THERMAL ENERGY STORAGE USING CARBONATE-SALT-BASED COMPOSITE PHASE CHANGE MATERIALS: LINKING MATERIALS PROPERTIES TO DEVICE PERFORMANCE

By

Chuan Li

A thesis submitted to the
University of Birmingham for the

Degree of Doctor of Philosophy

School of Chemical Engineering

College of Engineering and physical Sciences

The University of Birmingham

August 2016

UNIVERSITYOF
BIRMINGHAM

University of Birmingham Research Archive

e-theses repository

Abstract

Thermal energy storage (TES) has a crucial role to play in conserving and efficiently utilising energy, dealing with mismatch between demand and supply, and enhancing the performance and reliability of our current energy systems. This thesis concerns TES materials and devices with an aim to establish a relationship between TES device level performance to materials properties. This is a multiscale problem. The work focuses on the use of carbonate salt based composite phase change materials (CPCMs) for medium and high temperature applications. A CPCM consists of a carbonate salt based phase change material (PCM), a thermal conductivity enhancement material (TCEM, graphite flake in this work) and a ceramic skeleton material (CSM, MgO in this work). Both mathematical modelling and experiments were carried out to address the multiscale problem. The following is brief summary of the work.

First, the wettability of carbonate salt and MgO substrate is studied. It is found that the MgO-carbonate salt system presents an excellent wettability. The sintering of MgO reduces surface tension, leading to an increased contact angle between the carbonate salt and the sintered MgO. Second, microstructure characteristics and formation mechanisms of two CPCMs are explored. The results show that the addition of graphite flakes leads to reduced wettability of the carbonate salt on MgO and the tendency aggravates with increasing graphite loading. Salt motion occurs within the composite structure during repeated heating and cooling cycles. Such motion could form a shear force and break graphite flakes. The particle migration during the melting-solidification processes leads to a more homogenous distribution of both the salt and CSM/TCEM particle and an increase in the density of the microstructure. The CSM (MgO) particles in the single carbonate salt based composites would sinter and form a porous structure due to the use of a high sintering temperature. This reduces significantly the

swelling effect due to the presence of low surface energy graphite and restricts particle motion during melting-solidification thermal cycles. Third, an investigation on the effective thermal conductivity of the CPCMs is carried out based on the developed microstructures. A parallel-plate based experimental set up is constructed to measure the effective thermal conductivity of the composites. A theoretical model is proposed to predict the effective thermal conductivity of the single carbonate salt based CPCMs, and the model agrees well with experimental data. It is found that the Zehner-Schlunder model and Raticffr model can be used for the estimation of effective thermal conductivity of eutectic carbonate salt based CPCMs. Fourth, heat transfer behaviour of CPCMs based TES at component and device levels is investigated. This includes the formulation of a numerical model for transient heat transfer in CPCM modules and TES components and validation of the model via experiments. The model considers the thermal contact resistance within the TES component, and the influence of materials properties, module size and surface roughness of CPCM module as well as flow conditions of heat transfer fluid (HTF) are investigated. The results show that a constant mass ratio of PCM in CPCM modules gives the best combination of heat transfer rate and heat storage density. A larger CPCM module and a higher HTF inlet velocity give a more remarkable enhancement of the heat transfer behavior at the component level. For a given set of conditions, the concentric tubular based components offer better heat transfer performance compared with the single tubular components, with a total heat storage time and release time approximately 10% and 15% shorter, respectively. Trapezoidal packing TES device offers the best heat transfer behaviour and is superior to parallel and interlaced packing devices. At the same set of other working conditions, the total heat storage time for a trapezoidal configuration is shorter than parallel and interlaced packing devices, respectively 55.6% and 34.8%.

Acknowledgements

Table of Contents

List of Tables

List of Figures

Abbreviations

TES: Thermal Energy Storage

SHS: Sensible Heat Storage

LHS: Latent Heat Storage

TCES: Thermochemical Energy Storage

CAES: Compressed Air Energy Storage

CPCM: Composite Phase Change Material

PCM: Phase Change Material

TCEM: Thermal Conductivity Enhance Material

CSM: Ceramic Skeleton Material

MSLS: Molten Salt Liquefied Structure

PE: Penterythritol

PEG: Polyethylene Glycol

EP: Expended Perlite

DSC: Differential Scanning Calorimetry

MWCNTs: Multi-walled Carbon Nanotubes

SEM-EDS: Scanning Electron Microscopy with Energy Dispersive X-ray Spectrometry

AFM: Atomic Force Microscopy

HTF   Heat Transfer Fluid

Nomenclature

C	Specific heat ($J \cdot kg^{-1} \cdot K^{-1}$)
D	TES component diameter (m)
d	composite materials module diameter (m)
h_c	composite materials module thickness (m)
H	enthalpy (J)
Q	thermal energy storage capacity (J)
T	temperature (K)
U	velocity of HTF ($m \cdot s^{-1}$)
u	dimensionless axial velocity component
Re	Reynolds number
v	dimensionless radial velocity component
Y	y coordinate
X	x coordinate
r	radial coordinate
p	Pressure (Pa)
t	time (s)

L	latent heat (J·kg^{-1})
k	thermal conductivity (W·m^{-1}·k^{-1})
h	sensible enthalpy (J·kg^{-1})
ΔH	latent enthalpy (J·kg^{-1})
n	number of CPCM modules
β	liquid fraction
ε	volume ratio of TCEM in a PCM-TCEM mixture
ρ	Density (kg·m^{-3})
μ	dynamic viscosity (kg·m^{-1}·s^{-1})
ξ	volume ratio of CSM in a CPCM module
R	particle radius (m)
B	particle shape factor
α	deformed factor
ϕ	Porosity
Ω	Atomic volume (m^3)
J	vacancy flux
A	Surface area (m^2)
E	vacancy concentration

γ	Surface energy ($J \cdot m^{-2}$)
δ_s	effective superficial thickness
K_B	Boltzmann's constant ($J \cdot K^{-1}$)
r_m	Sintering curvature radius (m)
h_i	Infiltration height (m)
θ	Contact angle (°)

Subscripts

0	initial
Ref	reference value
e	effective
in	heat transfer fluid inlet velocity
PCM, pcm	phase change material
T, TCEM	thermal conductivity enhancement material
C, CSM	ceramic skeleton material
f, HTF	heat transfer fluid
c	composites
l	liquid phase
s	solid phase

sf   Solid-fluid mixture

sv   Solid/vapour

sl   Solid/liquid

lv   Liquid/vapour

Chapter 1 Introduction

1.1 Background

Global energy systems face great challenges [1-5]. In the UK, it is expected that the amount of electricity demand met by renewable generation in 2020 will be increased by an order of magnitude from the present levels [1, 2]. In the context of the targets proposed by the UK Climate Change Committee it is expected that the electricity sector would be almost entirely decarbonised by 2030 with significantly increased levels of electricity production and demand driven by electrification of heat and transport. India has been responsible for almost 10% of the increase in global energy demand since 2000. Its energy consumption in this period has almost doubled, leading the country's share in global demand up to 5.7% in 2013 from 4.4% at the beginning of the century [4]. The renewable energy share in US energy mix was 7.5% in 2010. This included 2.5% renewable power, 1.6% liquid biofuels and the remaining, 3.4%. This share will only increase to 10% by 2030. The REmap analysis indicates that it is technically feasible and cost-effective to increase the renewable energy share in total final energy consumption to 27% by utilizing existing renewable energy technologies [5]. In China, the government has promised to cut greenhouse gas emission per unit of gross domestic product by 40-45% by 2020 based on the 2005 level. This represents a significant challenge given that over 70% of its electricity is currently generated by coal-fired power plants [3]. Energy storage has the potential to provide a solution towards these challenges.

Energy storage refers to a reversible process that excess energy is stored into a form that can be transferred back to the same form or a different form when needed [6]. Numerous energy storage technologies exist currently due to different forms of energy, including

electrochemical (batteries, flow batteries and sodium sulphate batteries etc), mechanical (compressed air and pumped hydro etc), thermal (heat and cold), and electrical (supercapacitors) [6-8]. Thermal energy storage (TES) relates to a collection of technologies that store excessive energy in the forms of heat, cold and their combination in a medium termed TES material, and utilizes the stored thermal energy either directly or indirectly through energy conversion process when needed. TES currently accounts for approximately 55% of global non-pumped hydro installations [7-8]. However, the majority of research efforts have been paid on electrochemical energy storage in the past few decades [8]. The significance of TES should obtain wide recognition due to the following reasons:

a. Over 90% of global energy budget focuses on heat conversion, transmission and storage [6-8]. Thermal energy provides a main linkage between the primary and secondary energy sources [7-8], as illustrated in Figure 1.1.

b. Thermal energy is an intermediate product or by-product of industrial processes due to the thermodynamic constrains. Therefore, the utilization of TES technology has the potential to enhance the process energy efficiency and economics - a unique role that cannot normally be played by other energy storage technologies [6].

c. TES is an enabling technology for other energy storage methods, including cryogenic energy storage, compressed air energy storage and pumped thermal electricity storage. Integration of TES technology with power plants could substantially increase their capabilities of peak shaving and largely reduce the carbon capture costs [8].

d. Approximately 50% end use energy demand in the world is in the form of thermal energy [6].
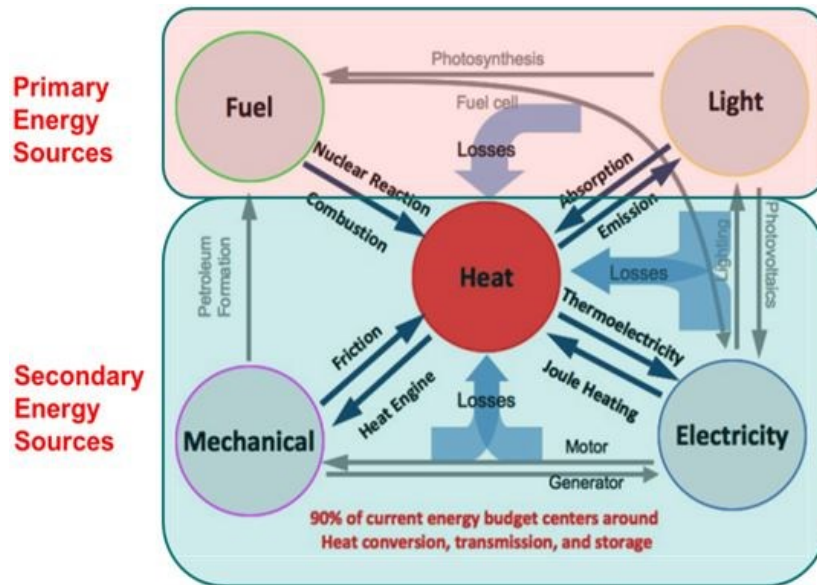
Figure 1.1 Thermal energy at the heart of energy chain [4].

Fundamentally, development of TES technologies requires the understanding of relationships between TES materials properties and performance of components, devices and systems as illustrated in Figure 1.2. This implies fundamental understanding of multiphase physics across multiscale. This forms the main motivation for this PhD thesis.
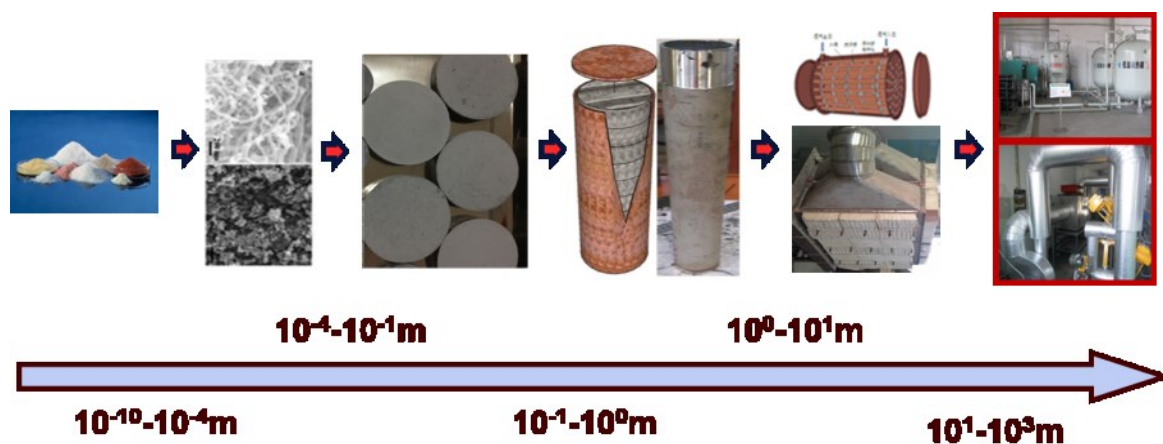
Figure 1.2 Multiscale multiphase physics of TES technologies: from materials

formulation to system integration [6].

1.2 Aims and Objectives

The aim of this study is to understand the relationship between TES materials properties and performance of components and devices. Composite phase change materials (CPCMs) are used as examples for the study, which consist of a phase change material (PCM), a thermal conductivity enhancement material (TCEM) and a ceramic skeleton material (CSM). The reasons for selecting this composite are associated with the combination of the energy and power densities, cost effectiveness, shape stability and long life span [9, 10]. The specific objectives of this study are:

(1). To study physical compatibility of different components of the CPCMs by investigating into the wettability of PCM on CSM.

(2). To characterise the microstructures of CPCMs and investigate into the microstructural evolution and underlying mechanisms.

(3). To develop a theoretical model for predicting the effective thermal conductivity of CPCMs and to validate the model experimentally.

(4). To study heat transfer and fluid flow behaviour of TES components and devices containing CPCMs.

1.3. Layout of the Thesis

This thesis consists of seven chapters. Chapter two provides a detailed summary of literature relevant to this work.

Chapter three looks at the wettability of PCM on CSM.

Chapter four studies the microstructural characteristics and evolving mechanism of CPCMs structures.

Chapter five explores the effective thermal conductivity of CPCMs.

Chapter six investigates into heat transfer and flow behaviour in CPCMs based TES components and devices.

Finally chapter seven summaries the main conclusions from this study and gives recommendations for future work.

Chapter 2 Literature Review

This chapter summarises relevant literature related to TES technologies covering materials, components and devices. Section 2.1 provides the current state of the art developments in TES technologies. Section 2.2 looks at TES materials particularly PCMs and CPCMs. Section 2.3 reviews the work on TES components and devices.

2.1 Thermal energy storage technologies

TES has a crucial role to play in conserving and efficient utilising energy, dealing with mismatch between demand and supply, and enhancing performance and reliability of energy systems [11-14]. TES technologies can be classified into three main categories of sensible heat storage (SHS), latent heat storage (LHS, also called PCM-based) and thermochemical energy storage (TCES); See Figure 2.1. SHS uses temperature difference and stores heat in solids and liquids; LHS is due to enthalpy change during solid-solid and liquid-solid phase change and TCES uses reversible adsorption/absorption/reaction enthalpy change due to interactions among liquid, solid and gas molecules [13]. An overview of literature on these different types of TES technologies is summarised below.

```
                    Thermal energy storage
                           (TES)
        ┌──────────────────┼──────────────────┐
     Sensible            Latent             Chemical
     ┌───┴───┐        ┌─────┼─────┐              │
                                           ┌── Thermochemical
                                           │
                                           ├── Reaction heat
                                           │
  Solid   Liquid    S-S   S-L   L-G        └── Heat pump
```
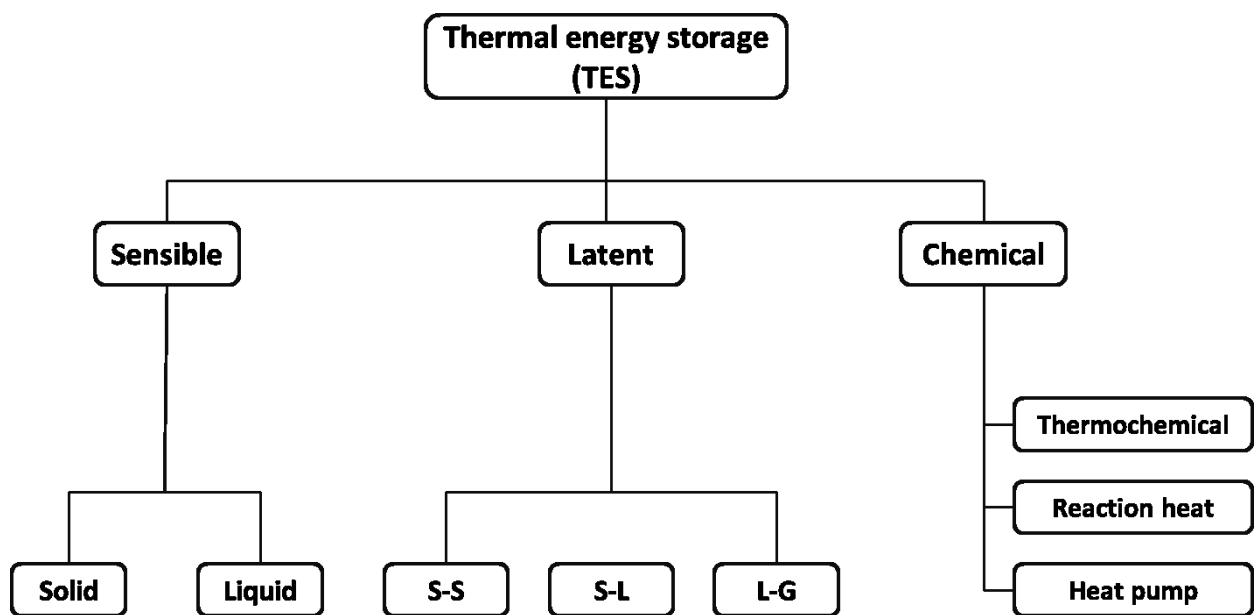
Figure 2.1 Classifications of TES technologies (S-S, solid-solid; S-L, solid-liquid; L-G, liquid-gas).

2.1.1 Sensible heat storage (SHS)

SHS is realised through temperature variation of storage materials. It can be further divided into solid SHS (metals, brick and ceramic materials) and liquid SHS (such as water and oil). The amount of heat stored in SHS is proportional to the temperature variation, the heat capacity and mass of storage materials [16], as described by the following equation:

$$Q = \int_{T_i}^{T_f} mC_p dT = mC_{ap}\left(T_f - T_i\right)$$
(2.1)

where T_f and T_i are respectively final and initial temperatures of the storage material, m is the mass of storage material, and C_{ap} is the average specific heat between T_i and T_f.

Some common used SHS materials and their properties are summarized in Table 2.1 [17, 18]. Water has the highest specific heat and is regarded as one of most cost effective SHS medium for applications below 100℃. Above the boiling point, the use of water requires an increase in the system pressure and hence cost. Therefore, materials with a high energy density similar to water have been sought for many years. Salts and petroleum based oils are commonly used for replacing water [17]. These materials have a lower vapour pressure and a wide temperature operation range than water. However, they suffer from one or more problems of corrosion, chemical stability, and short life etc. Solid materials such as brick, rock, concrete, wood, etc. are applicable for SHS at both low and high temperatures. However, these materials often suffer from low specific heat capacity and heat transfer can be an issue as well [18].

Table 2.1 Some common SHS materials [15-18].

Storage Medium	Temperature operation (°C)	Specific heat (J/kg·K)	Density (kg/m³)
Brick	20	840	1600
Rock	20	879	2560
Water	100	4190	1000
Concrete	20	880	1900-2300
Engine Oil	160	1880	888
Ethanol	78	2400	790
Butanol	118	2400	809
Isotunaol	100	3000	808
Octane	126	2400	704
Synthetic oil	30-100	2300	900
NaCl solid	50-150	850	2160
Cast iron	n.a.	560	7200
Magnesia fire bricks	50-200	1150	3000

2.1.2 Latent heat storage (LHS)

The storage mechanism of LHS (PCMs) is illustrated in Figure 2.2. When a PCM at solid state is heated and its temperature increases until it reaches the phase change point. Over this period, heat is stored in sensible form. Further heating of the material incurs solid to liquid phase transition and heat is stored in latent form and temperature is constant during this period. Once the phase change is completed, the PCM is in liquid phase, further heating of the material increases its temperature and heat is stored again in sensible form. Further heating to the material leads to boiling, which not normally used for TES. The reverse of the processes described above releases heat, which is also called discharge process.
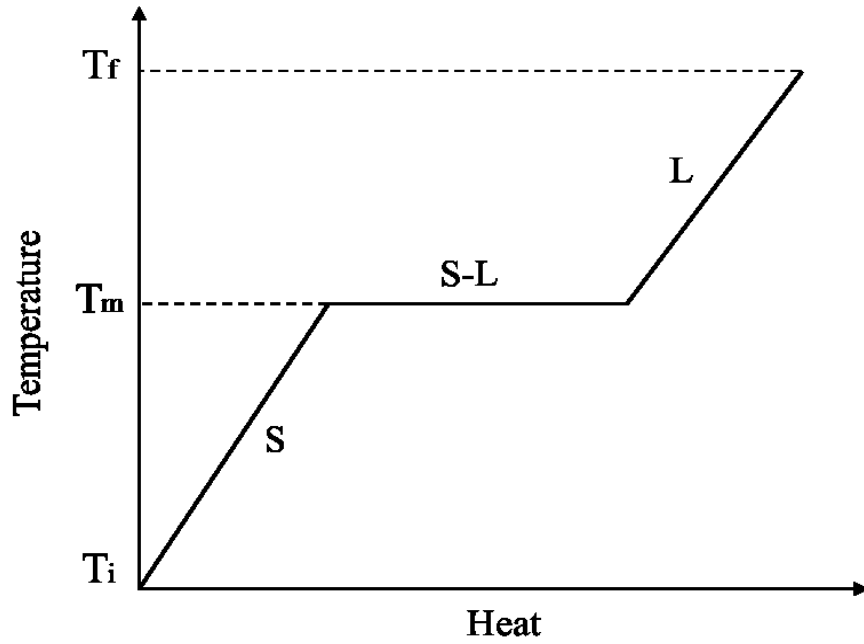
Figure 2.2 Phase change transition diagram for a LHS material.

As can be seen, a whole heat storage or release process involves three stages, two for sensible storage and one for latent storage, and hence the total heat storage capacity of a LHS material can be calculated by the following equation [19-21]:

$$Q = \int_{T_i}^{T_m} mC_p dT + mL_s + \int_{T_m}^{T_f} mC_p dT = m\left[C_{sp}(T_m - T_i) + L_S + C_{lp}(T_f - T_m)\right] \qquad (2.2)$$

where C_{sp} is the average specific heat between T_i and T_m, C_{lp} is the average specific heat between T_m and T_f, and L_s is the latent heat of solid-liquid transition.

It is seen that the heat capacity of a LHS material depends on its specific heat of both solid and liquid and the latent heat. Therefore, a high heat capacity and a large latent heat are key for LHS materials selection. As mentioned above, the transformation between solid and liquid states is specifically attractive due to small change in volume and has therefore been mostly investigated and utilized [22-25]. Solid-Solid phase change is less explored due to its low latent heat except of a few cases [23, 24].

2.1.3 Thermochemical energy storage (TCES)

TCES relies on reversible sorption of chemical reactions. Heat storage capacity is proportional to the mass of storage medium, the enthalpy change of the reversible processes and extent of the process towards equilibrium [26]. Mathematically, this takes the following form:

$$Q = m\Delta h_r \tag{2.3}$$

where, Δh_r is the endothermic heat of reaction.

TCES technology is still at the early stage of development. This study focuses on LHS using PCMs. As a result, TCES and SHS are not discussed further unless when necessary.

2.2 Thermal energy storage materials

2.2.1 Phase change materials (PCMs)

The thermophysical and chemical properties of PCMs are among the most important factors that determine the performance of a LHS system. Therefore, the selection of suitable PCMs for practical applications needs careful consideration. Table 2.2 lists some main characteristic requirements for PCMs selection.

Table 2.2 Main characteristic requirements for PCMs [13, 18].

Thermal properties	Physical properties	Kinetic properties	Chemical properties	Economic
Suitable phase change temperature	Favourable phase equilibrium	No supercooling	Chemical stability	Abundant
High latent heat	High density	Sufficient crystallization rate	Compatibility with materials of construction	Available
High thermal conductivity	Small volume change		Non toxic	Cost effective
High specific heat	Low vapor pressure		No fire hazard	

Numerous PCMs have proposed and studied in the literature. These materials can be divided into three groups of solid-solid PCMs, solid-liquid PCMs and liquid-gas PCMs. Solid-solid PCMs store heat through the crystallization forms transition and are companied by a relatively low latent heat. Liquid-gas PCMs are usually associated with a big volume change which leading to system complexity and some encapsulation issues. Solid-liquid phase change processes normally give a small changes of volume and relatively high latent heat, and are therefore the most promoting and widely used. Figure 2.3 shows classification of PCMs.
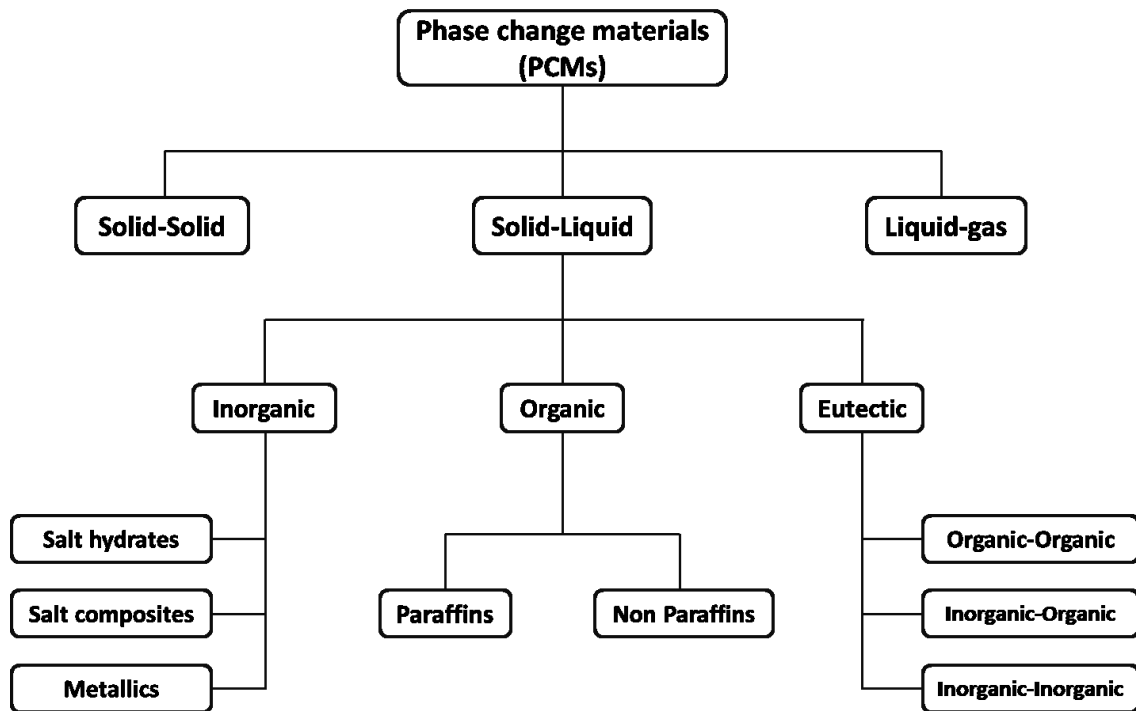
Figure 2.3 Classifications of PCMs.

Solid-liquid PCMs can be further classified into three main categories of inorganic, organic and eutectic PCMs. Inorganic PCMs include salt hydrates, salt composites and metallics. Organic PCMs consists of paraffins and non-paraffins such as fatty acids, esters and alcohols. Eutectic PCMs are made of two or more components, which can be organic-organic, inorganic-inorganic and inorganic-organic combinations. Some commonly used solid-liquid PCMs reported in the literature and their thermophysical properties are summarized in Table 2.3.

Table 2.3 Thermophysical properties of some common PCMs [18-28].

Materials	Melting temperature (^{o}C)	Heat of fusion (KJ/kg)	Density (kg/m^3)	Thermal conductivity (W/m K)
Capric acid	32	152.7	878(liquid) 1004(solid)	0.153(liquid)
Caprylic acid	16	148.5	901(liquid) 981(solid)	0.149(liquid)
$NaNO_3$	308	162.5	2260(solid) 1900(liquid)	0.5
$MgCl_2·6H_2O$	117	168.6	1450(liquid) 1569(solid)	0.57(liquid) 0.694(solid)
$CaCl_2·6H_2O$	29	190.8	1562(liquid) 1802(solid)	0.54(liquid) 0.108(solid)
Na_2CO_3/Li_2CO_3 (55.7/44.3)	498	393	2500	2.02
Alpha glucose	141	174	1544	n.a.
RT 65	64	154/173	910	0.2
RT 81	81	140	920	0.2
RT 90	90	163/194	930	0.2
$Mg(NO_3)_2·6H_2O$	89.3	149-175	1550	0.57 (120°C)
PK 80 A6	81	119	900	0.2
Benzanilide	161	162	n.a	0.4
O-Mannitol	166	294	1489	0.2
Hydroquinone	172.4	258	1358	0.2
Penterythritol (PE)	185	303	n.a.	0.2
Galactitol	188-189	351.8	1470	n.a.
Salicylic acid	159	199	1443	n.a.

These PCMs differ in not only the melting temperature and thermal properties, but also in melting-solidification process and are hence suitable for different applications. Table 2.4 compares the advantages/disadvantages of them.

Table 2.4 Summary of advantages and disadvantages of solid-liquid PCMs [25-29].

PCMs	Advantages	Disadvantages
Organic	•Good thermal stability •Small volume varies •Low vapour pressure •Wide operation temperature range •Freeze without much supercooling •No segregation •High fusion heat •Recyclable •Non-toxic	•Low thermal conductivity •Flammable
Inorganic	•Non-flammable •Relative high latent heat storage capacity	•Supercooling •Segregation •High volume varies •Corrosive
Eutectic	•Narrow melting points •Flexibility properties	•High cost •Corrosive •Limited available thermophysical properties data

2.2.2 Composite phase change materials (CPCMs)

As summarized above, organic PCMs and salt hydrates suffer from phase segregation and sub-cooling; inorganic PCMs have a low thermal conductivity and segregation; Eutectic

PCMs and molten salts are corrosive [13, 18]. Various approaches have been proposed to resolve these problems particularly for organic materials and inorganic hydrates [13]. These include encapsulation of PCMs to reduce sub-cooling and overcome leakage, and addition of highly thermally conductive materials such as metal foams and carbon materials to enhance their thermal conductivity [13]. However, these methods are not effective for molten salt based PCMs due to low thermal conductivity as well as chemical incompatibility [7]. Recent research has indicated that the use of CPCMs could provide an effective avenue to resolve these problems. Here, the CPCMs usually consist of a PCM, a TCEM and a CSM for shape stabilization. Such a combination has been shown to give an excellent combination of energy density, power density and mechanical properties [6, 9, 10].

Hong *et al.* [30] prepared paraffin and polyethylene based composites and investigated their thermal properties. Wang *et al.* [31] and *Tang et al.* [32] fabricated polyethylene glycol (PEG)/Silica dioxide (SiO_2) based composites by using a sol-gel method. Li *et al.* [33] also formulated a PEG/SiO_2 composite using the same method. Their results showed that the composites presented stable core-shell structures and can remain in the solid form even if external temperature exceeded the melting temperature of the PCM. Similarly, Wang *et al.* [34] prepared PEG/SiO_2 based composites using β-Aluminum nitride (β-ALN) as a thermal conductivity enhancer and studied their thermal properties. Their results indicated that the CPCMs gave a higher heat transfer rate and the thermal conductivity increased with an increase in β-ALN loading. Gokon *et al*. [35] prepared and investigated the thermophysical properties of alkali-carbonate and MgO ceramics composites. Xu *et al.* [36] prepared a methyl palmitate and methyl stearate composite and investigated the optimum formulation. Notter *et al.* [37] investigated the thermophysical properties of a ceramic-salt composite. Sari *et al.* [38] studied the preparation and thermophysical properties of paraffin and expanded graphite composites. Karaipekli and Sari [39, 40] formulated a mixture of capric acid and

myristic acid and expended perlite (EP) composite. The thermal properties, thermal reliability and thermal conductivity of the composites were determined. Their results showed a maximum salts concentration of 55wt% in the composites without PCM leakage from the composite. Thermal cycling measurements indicated good cycle life of the composite. Yang *et al.* [41] investigated PEG-tetraethyl orthosilicate composites containing various mass ratios of PEG made with the sol-gel method. The composites were characterized by X-ray diffraction (XRD) and differential scanning calorimetry (DSC), and the results showed that the silica structure held PEG strongly. Zhang and Feng [42] prepared a composite consisting of paraffin and olefin block copolymer as PCM and CSM, respectively. It was found that the composite had a good stability and excellent mechanical properties even with up to 40% of paraffin.

Karaman *et al.* [43] prepared PEG/diatomite composites with graphite as TCEM and studied their structure and thermal conductivity. Ye *et al.* [44] prepared and studied the thermal properties of CPCM consisting of $NaNO_3$, MgO and multi-walled carbon nanotubes (MWCNTs) as the PCM, CSM and TCEM, respectively. Introducing of MWCNTs into the composites greatly enhanced the thermal conductivity, and the extent of the enhancement increased with increasing mass ratio of the MWCNTs and testing temperature. Ge *et al.* [9, 10] prepared a CPCM with eutectic salt of lithium and sodium carbonates as the PCM, magnesium oxide as the CSM, and graphite as the TCEM. They found that the presence of CSM was essential for the dispersion of graphite materials within the PCMs. The wettability of the PCM on the CSM and TCEM significantly influenced the microstructure of the composites. Table 2.5 shows some CPCMs formulation methods reported in the literature.

Table 2.5 Fabrication methods of CPCMs [45-57].

Fabrication methods	PCM	Supporting materials	Thermal conductivity enhancer
Sol-gel method	polyethylene glycol;	Silica; silicon dioxide; tetraethyl orthosilicate	β-Aluminum nitride; Graphite
vacuum impregnation method	capric acid and myristic acid; palmitic acid	expanded perlite; vermiculite; carbon foam; cement; diatomite	
Physical blending method	Paraffin; polyethylene glycol; Molten salt; molten alkali-carbonate	Olefin block copolymer; Silica; porous carbon; active carbon; MgO	Graphite; carbon nanotubes

2.3 Thermal energy storage components and devices

2.3.1 Heat transfer analysis during phase change

Heat stored or released in solid-liquid PCMs is always accompanied by a phase transformation at liquid-solid interface [14]. During a storage process, solid phase melts, leading to an increase in the liquid phase, natural convection in the liquid phase often occurs. During heat release, the liquid phase freezes at the liquid-solid interface, forming an immobile layer of solid phase, which grows with time, giving up heat of fusion [21]. As natural convection is a more effective heat transfer mechanism than thermal conduction, the charging process is expected to be quicker than the discharging process. In addition, the solid phase often has a low thermal conductivity, giving rise to a slow heat transfer during

discharging. This in turn prolongs the energy release process. The governing equation for the phase change can be written as:

$$\lambda \rho \left(\frac{ds(t)}{dt} \right) = k_s \left(\frac{\partial T_s}{\partial t} \right) - k_l \left(\frac{\partial T_l}{\partial t} \right) \tag{2.4}$$

where λ is the latent heat of fusion, ρ is the density, $s(t)$ is the surface position, t is time, k is the thermal conductivity, subscripts s and l are the solid and liquid phases.

Heat transfer occurred at the liquid-solid interface is known as the Stefan problem [14, 20, 21]. Unlike single phase problems, heat transfer during phase change at the interface is much more complicated due to the following reasons:

(1). Non-linearity resulting from the movement of the phase change front [21].

(2). Lack of knowledge of heat transfer behaviour at the phase change front due to effect of buoyancy driven natural convection in the liquid phase field [22].

(3). Volume change occurs during phase change.

Several methods have been proposed to resolve the Stefan problem and they can be categorised into theoretical and experimental methods [20, 21]. The theoretical methods can be further divided into two groups of temperature-based and enthalpy-based methods [21-24]. In the temperature-based method, the phase change front is captured on a grid at each fixed time step, and non-uniform grid spacing and time step are utilized [29]. In the enthalpy-based method, the phase change interface fitting is totally eliminated by solving the energy equation with a fixed grid size and a fixed time step [21]. The enthalpy-based method is most suitable for solving the Stefan problem, especially when phase change takes place at a temperature range rather than at a constant temperature. In addition, there are more advantages: (1) the energy equation is similar to that for the single phase; (2) no specific conditions are needed to

be satisfied at the phase change front; (3) the enthalpy formulation involves the solution within a mushy zone, which includes both solid and liquid phases. The enthalpy-based method uses the following equation for the whole PCM area [24]:

$$\frac{\partial(\rho_p h_p)}{\partial t} = \frac{\partial}{\partial x}\left(k_p \frac{\partial T_p}{\partial x}\right) + \frac{\partial}{\partial y}\left(k_p \frac{\partial T_p}{\partial y}\right) \tag{2.5}$$

where h_p is the specific enthalpy of the sum of the sensible enthalpy (h_s) and the enthalpy change (βL) during phase change, k_p is the thermal conductivity of PCM, T_p is the temperature of PCM; L is the latent heat of PCM and β is the liquid fraction. In Equation (2.5), β is assumed to be zero in the solid phase, one in the liquid phase, and it is between zero to one at the solid-liquid interface; see Equation (2.6).

$$\beta = \begin{cases} 0 & if\ T_C \leq T_s \\ \dfrac{T_C - T_s}{T_l - T_s} & if\ T_s \leq T_C \leq T_l \\ 1 & if\ T_C \geq T_l \end{cases} \tag{2.6}$$

where T_s is the freezing point and T_l is the melting point, and their difference is due to supercooling or superheating of the PCM.

2.3.2 Thermal energy storage components and devices

A typical TES device usually consists of two main elements [21]: (1) an appropriate PCM suitable for the desired temperature range; and (2) an encapsulation for the PCM that can offer a desired heat transfer surface. A TES device is often made of components, and it can only function when it is integrated into a system. Successful utilization of a PCM depends on the device which provides encapsulation for PCM and container for HTF. A number of TES

devices have been developed. Figure 2.4 shows some examples of the TES devices reported in the literature.
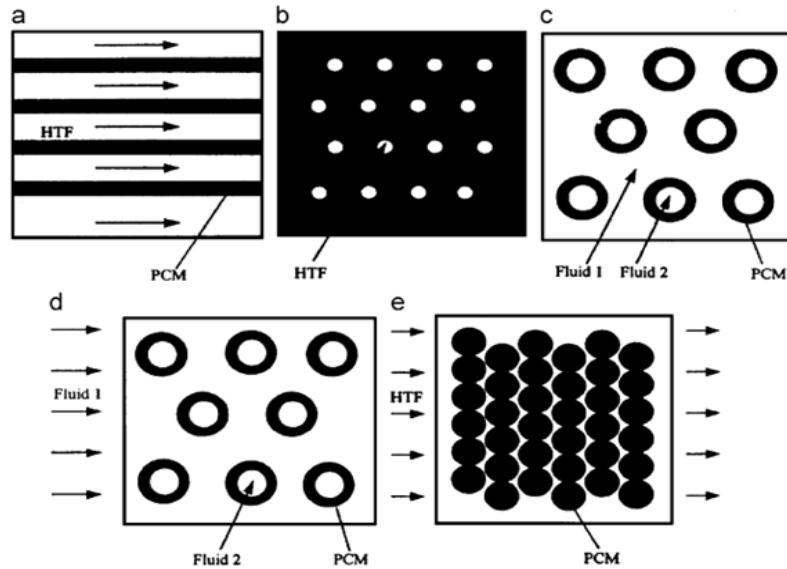
Figure 2.4 Different types of TES devices [21]: (a) Flat plate; (b) Shell and tube—internal flow; (c) Shell and tube—parallel flow; (d) Shell and tube—cross flow; (e) Packed bed.

Macro-encapsulation of PCM is a common type of TES components assembled to give a device for which both liquid and gas phases can be used as HTFs. This type of TES components can also prevent phase separation and is easier to operate and manufacture. The geometry and structure of macro-encapsulation vary from packed bed, to shell and tube, and to flat plate [21, 24].

2.3.2.1 Packed bed based TES components and devices

A schematic diagram of packed bed based TES device consisting of PCMs storage components is shown in Figure 2.5. Heat is transferred to or from a HTF with the HTF flowing through the voids between the components in the bed [21, 58]. During heat storage,

the high temperature HTF carrying heat flows through the bed and transfers the heat to PCM components in which PCMs absorb the heat and melt when temperature exceeds its melting point. Heat is released through TES components from PCM during heat release with the PCM freezing when temperature decreases to below the melting point.
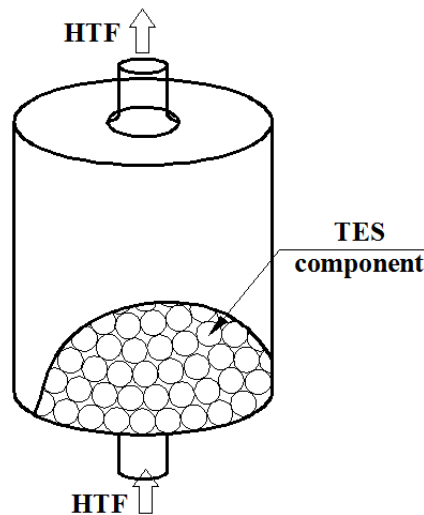
Figure 2.5 Schematic diagram of a packed bed based TES device.

Packed bed based TES devices provide a relatively large specific heat transfer surface within a small volume, which prolongs tortuous flow paths between TES components, enhances heat transfer during charging and discharging processes [21]. The heat transfer in a packed bed based TES device is determined by a number of factors such as packing ratio, component size and shape, operation conditions, and properties of PCM and HTF [58-60]. Those parameters need to be carefully considered when designing a packed bed based TES device.

Detailed HTF flow patterns and heat transfer processes inside a packed bed based TES device are complicated due to less regular packing of PCM components and disturbed flows in the bed. In order to investigate such behaviour, various mathematical and experimental studies have been carried out. The first mathematical study on packed bed based TES device was performed by Schuamnn [24] and most modelling studies reported so far has been based on

his model [58]. Mathematical models reported in the literature can be broadly divided into five categories; See Table 2.6 summarises the governing equations for the PCM and HTF. In the following, main assumptions for these models are discussed.

(1). Schmamnn's model: No heat transfer between TES components containing PCM was assumed and thermal conduction in the radial direction was not considered [60].

(2). Single phase model: In this model, solid and fluid phases in the device are treated as one phase. This model is only effective for the bed packed with very high thermal conductivity materials; there is not thermal resistance between liquid and solid.

(3). Continuous phase model: In this model, packed PCM components are assumed to be a continuous porous medium rather than a medium consisting of independent and individual TES components [61, 62].

(4). Thermal diffusion model: This model assumes a temperature gradient inside PCM components and there is no inter-TES component heat transfer. The temperature gradient at the TES component surface is only due to heat transfer between HTF and TES components [60].

(5). Effective packed bed model: Heat transfer between PCM components is assumed negligible in this model, and the heat is transported through point-to-point contacts between TES components and voids in-between is transformed from 3-D to 2-D ones [63].

Table 2.6 Governing equations of HTF and PCM containing TES components [58-63].

Single phase model:

$$[(1-\eta)\rho_s C_s + \eta\rho_f C_f]\frac{\partial\varphi}{\partial t} + GC_f\frac{\partial\varphi}{\partial Z} = k_{ef}\frac{\partial^2\varphi}{\partial Z^2} + k_{ef}\left[\frac{\partial^2\varphi}{\partial r^2} + \frac{1}{r}\frac{\partial\varphi}{\partial r}\right]$$

Continuous solid phase model:

HTF: $\eta\rho_f A_c L_d C_f\left(\dfrac{\partial T_f}{\partial t} + V\dfrac{\partial T_f}{\partial x}\right) = h_s a_p\left(T_p - T_f\right)$

PCM: $(1-\eta)\rho_f A_c L_d C_p\dfrac{\partial H_p}{\partial t} = h_s a_p\left(T_f - T_p\right)$

Continuous solid phase model including conduction effect along the axial direction:

HTF: $\eta\rho_f A_c L_d C_f\left(\dfrac{\partial T_f}{\partial t} + V\dfrac{\partial T_f}{\partial x}\right) = k_f\dfrac{\partial^2 T}{\partial x^2} + h_s a_p\left(T_p - T_f\right)$

PCM: $(1-\eta)\rho_f A_c L_d C_p\dfrac{\partial H_p}{\partial t} = k_f\dfrac{\partial^2 T_f}{\partial x^2} + h_s a_p\left(T_f - T_p\right)$

Enthalpy based model:

HTF: $\eta\rho_f A_c L_d C_f\left(\dfrac{\partial T_f}{\partial t} + V\dfrac{\partial T_f}{\partial x}\right) = h_s a_p\left(T_p - T_f\right)$

PCM: $\rho_p\dfrac{\partial H_p}{\partial t} = k_p\dfrac{\partial^2 T_p}{\partial r^2} + \dfrac{2}{r}k_p\dfrac{\partial T_p}{\partial r}$

Effective packed bed model:

HTF: $\dfrac{\partial(\rho_f c_f T_f)}{\partial t} + \dfrac{\partial(\rho_f c_f u_f T_f)}{\partial x} + \dfrac{\partial(\rho_f c_f v_f T_f)}{\partial y} = \dfrac{\partial}{\partial x}\left(k_f\dfrac{\partial T_f}{\partial x}\right) + \dfrac{\partial}{\partial y}\left(k_f\dfrac{\partial T_f}{\partial y}\right)$

PCM: $\dfrac{\partial(\rho_f h_p)}{\partial t} = \dfrac{\partial}{\partial x}\left(k_p\dfrac{\partial T_p}{\partial x}\right) + \dfrac{\partial}{\partial y}\left(k_p\dfrac{\partial T_p}{\partial y}\right)$

Concentric dispersion model:

$$\text{HTF: } \eta \rho_f C_f \left(\frac{\partial T_f}{\partial t} + V \frac{\partial T_f}{\partial x} \right) = k_f \frac{\partial^2 T}{\partial x^2} + h_s a_p \left(\vartheta - T \right) - U_w a_w (T - T_0)$$

$$\text{PCM: } \rho_s C_s \frac{\partial \vartheta}{\partial t} = k_s \left(\frac{\partial^2 \vartheta}{\partial r^2} + \frac{2}{r} \frac{\partial \vartheta}{\partial r} \right)$$

Notes: η-void fraction; A_c-cross sectional area of the device; L_d-height of the device; V-HTF velocity along the device void fraction; h_s-surface heat transfer coefficient between HTF and PCM; a_p-surface area of the PCM components.

Erek and Dincer [64] performed a numerical analysis of heat transfer behaviour of an ice based TES device using a concentric dispersion model with an empirical heat transfer coefficient correlation. Arkar and Medved [65] used the continuous solid phase model to investigate heat transfer behaviour of a packed bed based TES device with paraffin as PCM. The influence of thermal properties of PCM on the response time of the device was discussed. Benmansour et al. [66] also used the continuous solid phase model to analyse the transient behaviour of a cylindrical packed bed based TES device. Similarly, Hu et al. [67] studied a direct contact condenser consisting of a packed bed TES device in a solar driven humidification-dehumidification desalination plant by using the continuous solid phase model. Ismail and Henríquez [68] numerically investigated a packed bed based TES device packed with spherical capsules of water as PCM. The numerical modelling was performed with a marching technique which coupled the phase change inside the spherical capsules with the energy equation through the spherical boundary and the HTF. Regin et al. [69] studied a similar problem but with paraffin as PCM using the enthalpy method. They analysed the phase change phenomena of PCM inside the spherical capsules. This was for solar water heating applications. The effects of PCM phase change temperature range, the PCM capsule

size HTF inlet temperature and flow rate on the performance of the packed bed based TES device were investigated. Rady [70] numerically and experimentally studied heat transfer behaviour of a packed bed based TES device containing granular PCM as storage component. The governing equations for heat transfer in the device were obtained by considering a representative elementary volume containing granular PCM particles and air. MacPhee and Dincer [71] investigated the charging process of an ice packed bed based TES device. The energy, thermal exergy and flow exergy efficiencies, internal and external irreversibilities corresponding to flow exergy, as well as charging time were estimated. Wu *et al.* [72] studied heat transfer behaviour of a packed bed based cool storage device using n-tetracdecane as PCM, and numerically evaluated the kinetics using the implicit finite different method. Xia *et al.* [63] developed an effective packed-bed model to study the performance of a packed bed based TES device. They studied the effects of structural arrangement of TES components containing spherical capsules of PCM and PCM properties on the heat transfer behaviour of device. Eduard Ori *et al* [61] studied the performance of a packed bed based TES device using two different mathematical models and built an experiment set up to validate the modelling result. Karthikeyan and Velraj [60] performed a comparative study with three different mathematical models on the performance of a packed bed based TES device. Using paraffin as PCM encapsulated into spherical form, the effects of HTF properties, PCM capsule size and HTF operation conditions were investigated. Hitesh *et al.* [73] developed a heat transfer model for the packed bed based TES device and accounted for wall heat transfer coefficient and intra-particle diffusion effects. Based on the results, recovered and lost exergy were calculated. Table 2.7 summarises studies on packed bed based TES device reported in the literature.

Table 2.7 Summary of heat transfer behaviour studies on packed bed based TES device reported in the literature.

References	PCM/HTF	Investigation methods	Models	Parameters	Numerical method	Main conclusions
1. Benmansour *et al*, **2006** [66]	Paraffin wax/Air	Both charging and discharging/ Experimental investigation & mathematical modeling.	Continuous solid phase model.	Prandtl number; Reynolds numbers	Alternating Direction Implicit and Fully explicit scheme	*1.* Numerical model has accurate prediction of the temperature distributions within the bed.
2. Ismail and Henriquez, **2002** [68]	Water/30% volumetric concentration ethylene glycol solution	Charging/ Experimental investigation & mathematical modeling.	One dimensional model	Fluid flow rate; fluid entry temperature; Material of the spherical capsule	Finite difference approach and moving grid technique	*1.* Increasing working fluid volumetric flow rate reduces the fully charging and discharging processes. *2.* High thermal conductivity materials reduce the charging and discharging times.
3. Arkar and Medved, **2005** [65]	Paraffin(RT20) / Air	Both charging and discharging/ Experimental investigation &mathematical	Continuous solid phase model	Fluid flow rate; Apparent heat capacity	Explicit finite-difference approximation method	*1.* The apparent heat capacity should include an additional parameter-a heating or cooling rate. *2.* The experimental and

			modeling.			numerical results have the considerably better agreement when apparent heat capacity is integrated into the numerical model.
4. Eduard Oro *et al*, **2013** [67]	Organic material (C_{ps}=4000J/kg. K C_{pl}=3000J/kg. K h=175KJ/kg (-2-13C)/ water	Charging/ Experimental investigation & mathematical modeling.	Continuous model based on the Brinkman equation Energy equation model (Treat the PCM capsules as individual particles)	Gravitational force; Nu;	control volume based method-CFD, COMSOL 4.2 and Gauss seldel iterative method	*1.* Free convection is not as important as forced convection when higher Re number dominates the heat and mass transfer, the Brinkman equation will be the most useful model. *2.* Both mathematical models are validated with experimental data and the agreement is accurate.
5. L. Xia *et al*, **2010** [63]	1: Paraffin/ Water 2:Paraffin(RT20)/ Air	Both charging and discharging/ Mathematical modeling.	Effective packed bed model	PCM spheres arrangment; Encapsulation of PCM-materials and thickness	CFD 6.2 Control volume based technique for the energy equation and SIMPLE algorithms for pressure and	*1.* Heat retrieval rate with randomly packed PCM components is higher than that with specially packed ones; *2.*Both PCM properties and thickness of the encapsulation have the significant influences on the heat transfer performance

						velocity fields.	of the device; _3_. The effective packed bed model is versatile for various packed configurations;
6. A.Felix Regin *et al*, **2009** [21]	Paraffin wax/ water	Both charging and discharging/ Mathematical modeling.	Schumann model and enthalpy method		Inlet heat transfer fluid temperature(St efan number); fluid flow rate; phase change temperature range; capsules size;	Finite difference approximation	_1. S_olidification process is longer than melting process due to the low heat transfer rate during solidification. _2._ Higher Stefan number and mass flow rate reduce the fully charging process. _3._ Small radius capsules give a faster _4._ For a proper modeling, the phase change temperature range of the PCM must be accurately known and should be take into account.
7. S.Karthikeyan and R. Velraj,	Paraffin wax/ Air, water	Charging/ Experimental investigation &	_1._ continuous solid phase model-neglect		Mass flow rate, ball size.	Fully explicit finite difference method	_1._ HTF operating conditions have significant effect on the charging process.

2012 [60]		mathematical modeling.	the axial direction conduction 2. continuous solid model included the axial direction conduction 3. enthalpy based model			2. The effect of axial conduction can be negligible. 3. Continuous solid phase model is effective when air used as HTF and Enthalpy based model is recommended for the water as the HTF.
8. Shuangmao Wu *et al*, 2010 [72]	n-tetradecane/40 %aqueous ethylene glycol solution	Both charging and discharging/ Mathematical modeling	Continuous phase model	Inlet fluid temperature, mass flow rate, diameter of capsule, porosity;	Implicit finite difference approach and central difference approximation.	1. Increasing of HTF flow rate leads to a reduction of charging/discharging process. 2. HTF inlet temperature has strongly effect on both charging and discharging processes. 3. Lower packed porosity gives a higher cool storage capacity and a longer melting and solidification processes
9. Hitesh Bindra *et al*, 2013 [73]	Alumina/air	Both charging and discharging/ Experimental investigation & mathematical	A robust system-scale heat transfer model	Wall heat transfer, intra-particle diffusion effects,	Implicit finite difference approach	1. A high axial dispersion and ambient loss lead to lower exergy efficiency. 2. SHS device provides much higher exergy recovery

modeling.	recovery and lost exergy,	efficiency than LHS device. *3.* The pressure drop model could be further coupled with the thermal model.

2.3.2.2 Shell and tube type TES components and devices

Shell and tube type of TES devices are considered one of the most popular for commercial applications. In this type of configuration, PCM is contained in the space between the shell and tubes, with the HTF flows through the tube, as shown in Figure 2.6. Heat is transferred to or from PCMs through the tube walls.
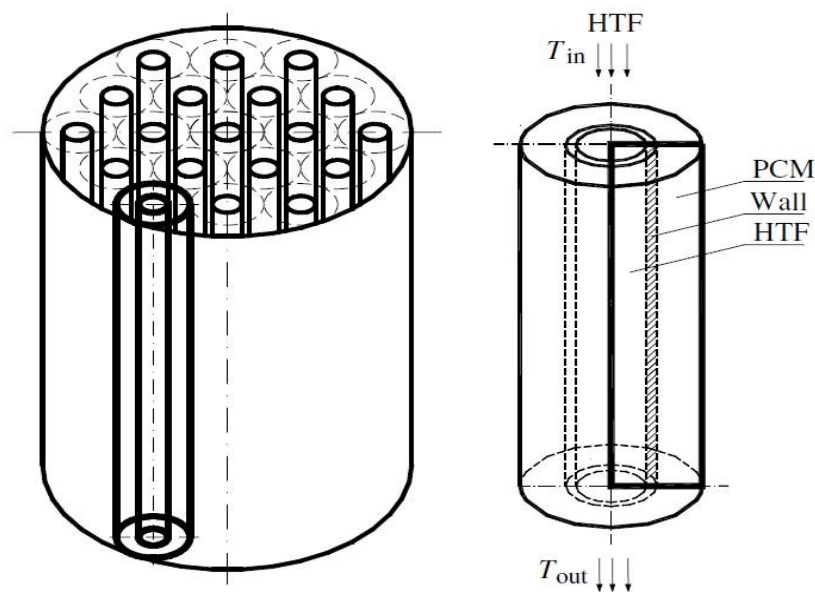
Figure 2.6 Schematic diagram of a shell and tube type TES device [74, 75].

The shell and tube type TES devices have been investigated by a number of researchers both experimentally, analytically and by modelling. Anica Trp [76] investigated heat transfer behaviour of a shell and tube TES device using paraffin as PCM and water as HTF. A FORTRAN computer code was written based on the enthalpy method to simulate the transient thermal behaviour of device during charging and discharging processes.

Liu *et al*. [77] numerically simulated a shell and tube TES device with Paraffin and water as PCM and HTF, respectively. The effects of properties of PCM and operation conditions of HTF on heat storage capacity and heat storage rate of device were studied. They showed that

the total heat storage capacity and rate of device increased when the initial temperature of PCM decreased or inlet temperature of HTF increased. Pandiyarajan *et al.* [78] experimentally studied thermal characteristics of a combined sensible and latent shell and tube TES device for diesel engine exhaust heat recovery and found that nearly 10-15% of total heat was recovered with the use of this combined device. Avci and Yazici [79] experimentally investigated heat transfer characteristics of a horizontal shell and tube TES device containing paraffin. The effect of inlet temperature of HTF on the melting and solidification processes was determined. Their results showed that increasing (for melting process) or decreasing (for solidification process) of HTF inlet temperature was found to enhance phase change process inside the device. In a similar experimental study, Akgun *et al.* [80] investigated the melting and solidification characteristics of paraffin in a shell and tube type TES device and the results indicated that increasing of HTF inlet temperature leaded to a decrease in the melting time. Agyenim *et al.* [81] compared two configurations of shell and tube TES devices using numerical modelling. Temperature gradients along the axial, radial and angular directions were compared and analysed. They found that the temperature gradient of PCM field during phase change was greatest in the radial direction for both devices and the recorded temperature gradients in the axial direction were respectively 2.5% and 3.5% that of the radial direction. Wang *et al.* [82] numerically investigated the charging and discharging characteristics of a shell and tube device containing an n-octadecane. The effect of HTF operation conditions on the thermal behaviour of device was studied. Their results showed that HTF inlet temperature had great effect on charging and discharging processes. Under the same working conditions, discharging process had a larger heat transfer rate than charging process. Tao *et al.* [83] developed a numerical code to investigate heat transfer performance of a shell and tube TES device for solar thermal collection. The effect of the non-uniform heat flux on the temperature distribution in PCM was examined. Their found

that the non-uniform heat flux boundary resulted in significantly non-uniform temperature distribution in PCM field. Ismail and Abugderah [84] employed a fixed grid numerical model to study the thermal behaviour of a vertical shell and tube TES device. The effects of Reynolds and Stefan numbers, and device geometry on the heat transfer behaviour of device were discussed. Their results indicated that the phase change temperature range had little effects on the device performance. The most significant parameters in influencing the device performance were the device length and tube outer radius. Wang *et al.* [85] experimentally analysed heat transfer performance of a novel dimpled shell and tube TES device. The thermal behaviour and pressure drop of the device were studied and the results were compared with spherical dimples and conventional smooth configurations. The ellipsoidal dimpled tube device was found to be better performance on heat transfer with a relatively low pressure drop than that spherical dimpled tube device. Most of studies on the shell and tube type TES device summarised above used either organic or inorganic PCMs with low thermal conductivity. This limits heat transfer rates during both charging and discharging processes. As a result, many investigated have been carried to enhance heat transfer at the PCMs side of the device. The most common approaches have been the use of fins of different configurations to the inner surface of the tube and high thermal conductivity enhancers, such as metal foam and graphite [86]. Heat transfer in a PCM-based TES device can also be from the HTF side, particularly when low thermal conductivity HTF such as air and water are used. In such cases, the main thermal resistance of shell and tube based TES device occurs in the HTF side. Measures have also been investigated to enhance heat transfer in the HTF side by using for example different tube structures to increase heat transfer surface area and internals fins to create the turbulence [87-93]. Table 2.8 gives a summary of the heat transfer enhancement methods reported in literatures for shell and tube based TES devices.

Table 2.8 Summary of heat transfer enhancement methods for shell and tube based TES device containing PCM [86-99].

References	Heat transfer enhancement methods		PCM/HTF	Research method	Parameters	Conclusions
1. Agyenim *et al*, **2009**	PCM side	Circular and longitudinal fins	Erythritol/air	Experimental and numerical	HTF operating conditions; Fins type; Device geometry	Longitudinal finned configuration gives the best charge behavior with insignificant sub-cooling during discharging process.
2. Mosaffa *et al*, **2012**	PCM side	Longitudinal fins	CaCl$_2$.6H$_2$O/air	Numerical	HTF operating conditions; System geometry	PCM solidifies more quickly in a cylindrical shell configuration than in a rectangular configuration. Heat transfer behavior of the device is enhanced by adding fins.
3. Fleming *et al*, **2015**	PCM side	Metal foam	Water/Dynalene+water (60:40)	Experimental and numerical	Thermal conductivity of metal foam; Porosity; HTF operating conditions	Natural convection plays a significant role in heat transfer behaviour. The use of metal foams significantly increases heat transfer rate during both melting and solidification.

No.						
4. Ermis *et al*, **2007**	PCM side	Finned tube	Water/Ethyl-alcohol (CH$_3$-CH$_2$OH)	Numerical	Finned tube size; HTF operating condition	Artificial neural network algorithm is found to be more accurate than numerical results.
5. Adine *et al*, **2009**	PCM side	Multi PCMs	(1)P116/water；(2) n-octadecane/water	Numerical	Mass ratio of PCMs; HTF operating conditions	A lower inlet temperature offers a higher heat transfer rate when HTF mass flow reaches a moderate rate.
6. Ismail *et al*, **2001**	PCM side	Axially fin	N/A	Numerical	Fin structure (Length, thickness, amount)	The number of fins, and the length and thickness of the fins are found to influence the solidification time. Natural convection in PCM is delayed with the use of fins.
7. Zhengyu Liu *et al*, **2013**	PCM side	Metal foam	Paraffin RT58/water	Numerical	Foam structure, porosity; HTF operating conditions.	Heat transfer rate can be enhanced by more than seven times compared with the use of pure PCM.
8. Rathod *et al*, **2015**	PCM side	longitudinal fins	Stearic acid/water	Experimental	HTF operating conditions	Heat transfer augmentation is more sensitive to the increase of HTF inlet temperature; Solidification time reduces up to 43.6%

						with the use of fins.
9. Mosaffa *et al*, **2014**	PCM side	Multi PCMs	(1) CaCl$_2$.6H$_2$O; (2) RT25；/Air	Experimental and numerical	HTF operating conditions	HTF inlet temperature is more significant than HTF flow rate in enhancing exergy efficiency.
10. Tao *et al*, **2012**	HTF side	Heat transfer area enhancement (Dimpled, cone-finned and helically tube)	LiF-CaF$_2$(80.5%-19.5%)/He-Xe	Numerical	Size of tube; HTF operating conditions	Heat transfer performance is significantly enhanced by changing tube surface features.
11. Mesalhy *et al*, **2005**	PCM side	Metal porous matric	N/A	Numerical	Metal foam thermal conductivity; HTF operating conditions	The presence of a porous matrix has a great influence on the heat transfer behavior and PCM melting rate.
12. Guo and Zhang, **2008**	PCM side	Aluminum foils	KNO$_3$-NaNO$_3$/Water/steam	Numerical	HTF operating conditions; system geometry size	The use of aluminum foils is an effective method to enhance the device thermal performance.
13. Li *et al*, **2013**	PCM side	Multi PCMs	(1) K$_2$CO$_3$-Na$_2$CO$_3$(51-49); (2) Li$_2$CO$_3$-	Numerical	Device structure; HTF operating conditions	Melting time decreases with an increase in HTF inlet temperature; Melting rate

			Na$_2$CO$_3$-K$_2$CO$_3$(20-60-20); (3) Li$_2$CO$_3$-K$_2$CO$_3$-Na$_2$CO$_3$(32-35-33);/Air			gradually decreases along both axial and radial directions.
14. Languri *et al*, **2013**	PCM side	Corrugated tube	Octadecane/Water	Experimental	Tube geometry structure; HTF operating conditions.	The use of corrugated tube gives nearly 9 times increase in heat transfer rates compared to a normal device.
15. Zhang and Faghri, **1995**	HTF side	Internal fins	N/A	Numerical	HTF operating conditions; Fins structure;	Addition of internal fins is an effective way to improve heat transfer rate when a low thermal conductivity is used.

2.3.2.3 Plate type TES components and devices

Plate type TES devices have gained widely attention due to compact design, high specific heat transfer areas, low pressure drop, and easy to clean and maintain. A schematic diagram of a typical plate type TES device is shown in Figure 2.7. PCM is filled in between neighbour plates with HTF flowing through flat channels between the PCM plates. Heat is transferred to or from PCM through the plate walls.
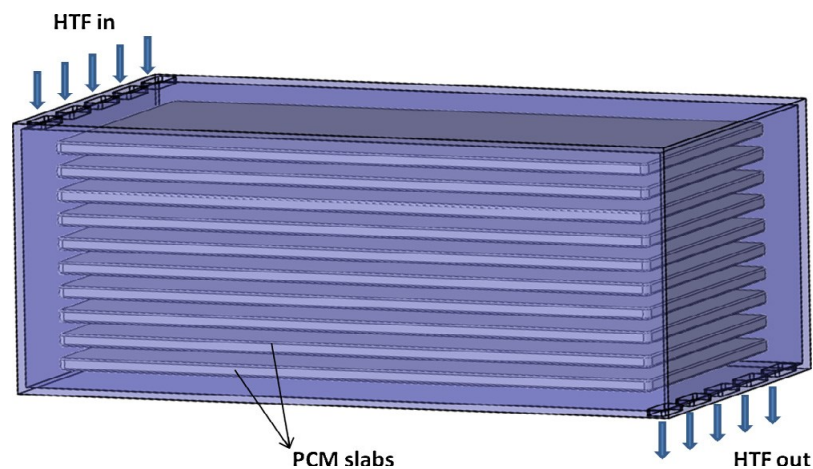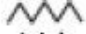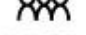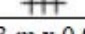
Figure 2.7 Schematic diagram of plate type TES device [100].

Campos-Celador *et al.* [101, 102] numerically investigated a TES device with finned plate filled with RT60 as PCM and water as HTF. The effect of HTF operating conditions on thermal behaviour of device was examined, and the results were compared with the packed bed based TES device with the same storage capacity. The plate type of device was found to be superior to the packed bed device.

Johnson *et al.* [103] experimentally studied heat transfer behaviour of a flat plate TES device. A eutectic mixture salt of KNO_3-$NaNO_3$ was used as a PCM and Mobiltherm 603 was employed as HTF. Various plate geometries were investigated, as illustrated in Table 2.9. Their results showed that the addition of heat transfer enhancement structure significantly

improved the heat transfer rate, and the cross-profile configuration offered the best heat transfer performance compared to other configurations.

Table 2.9 Heat transfer behaviour of plate type TES devices reported in [103].

Abbreviation	Descriptor	Drawing	Additional heat transfer surface area [m²]*	Structure volume [%]*	Phase change time during discharge [h]
None	None		0	0	5.51
WP	Waved profile		2.15	4.95	3.95
TP	Trapezoidal profile		2.15	4.96	3.69
RP	Rounded profile		2.27	5.21	4.63
ZZP	Zigzag profile		2.66	6.12	3.62
HP	Hollow profile		2.84	6.61	3.24
SCP	Semicircle profile		2.84	7.18	3.61
XP	X-profile		3.27	7.60	3.88
ZP	Z-profile		3.39	7.82	3.21
CP	Cross profile		3.75	8.66	2.64

* for comparison: using a 0.6 m x 0.93 m x 0.076 m chamber

Bechiri and Mansouri [104] numerically investigated the melting and solidification processes of paraffin in a plate type TES device and found that Reynolds number had a significant impact on the device overall storage performance. Increasing HTF inlet temperature leaded to a reduction of PCM melting time at a given HTF mass flow rate. Tian and Zhao [105] analysed the charging and discharging behaviour in a plate device containing paraffin. The PCM samples with metal foam embedded was investigated, and the results indicated that the addition of metal foams considerably enhanced device heat transfer performance. Liu *et al.* [100] numerically studied the heat transfer performance of a plate type TES device with a eutectic carbonate salt as PCM for concentrated solar power (CSP) applications. Six gaseous and liquid HTFs were considered and the effects of HTF thermal properties, operating conditions and heat storage capacity on the both charging and discharging processes were investigated. Their results showed that liquid sodium had the best heat storage capacity. At the same working conditions, the use of liquid sodium as HTF gave a 25% shorter fully

charging period than that of solar salt. Charvat *et al.* [106] investigated both numerically and experimentally thermal performance of a plate TES device with paraffin as PCM and air as HTF. The influences of HTF flow rate, inlet temperature and the thickness of plate component were analysed. They showed a significant impact of the HTF operating conditions and PCM plate thickness on the device performance. Halawa and Saman [107] formulated a theoretical model for a plate type TES device containing calcium chloride hexahydrate as PCM with a phase change temperature of 28 ℃. The effects of natural convection, plate component dimension and HTF operating conditions were studied. They found that thicker PCM slab reduced the heat transfer rate and therefore prolonged the whole charging and discharging processes. Ye *et al.* [108] numerically simulated thermal storage and release processes of a two-dimensional plate-fin device. Their results showed a significant role of the temperature difference between HTF and PCM in the device performance particularly when the temperature differences were below 20 ℃. Darzi *et al.* [109] numerically investigated heat transfer behaviour of a plate type device with Rubitherm as PCM. The effects of various parameters such as HTF operating conditions and plate component dimension on the melting front, outlet temperature, cooling power and thermal behaviour of device were examined. Their result indicated that the thickness of the PCM plate played an important role in the thermal performance of device and had a linear relation with the melting process.

There are also many other studies on the heat transfer behaviour of plate type heat exchangers [110-118]. These studies are not explicitly for TES applications but maybe of interest to the readers.

2.3.2.4 Other types of PCM based TES components and devices

Tay *et al.* [119-121] conducted a combined experimental and theoretical investigation of a U-type cylindrical TES device during the charging and discharging processes. They used hydrate salt as PCM and the PCM is filled in the interior of cylinders. Water was used as HTF circulating inside the U tube, as shown in Figure 2.8. A model based on the effectiveness-number of transfer units (ε-NTU) was developed. Numerical results of both the charging and discharging processes agree well with experimental data. After validated the numerical model, Tay *et al.* [122] compared heat transfer behaviour of device with pinned tubes, finned tubes and plain tubes; see Figure 2.9. Transient temperature distributions of the tube wall and PCM field were obtained under different HTF operating conditions. They found that finned tubes based device provided higher heat transfer rate than pinned tubes based device without impacting on the overall energy storage capacity.
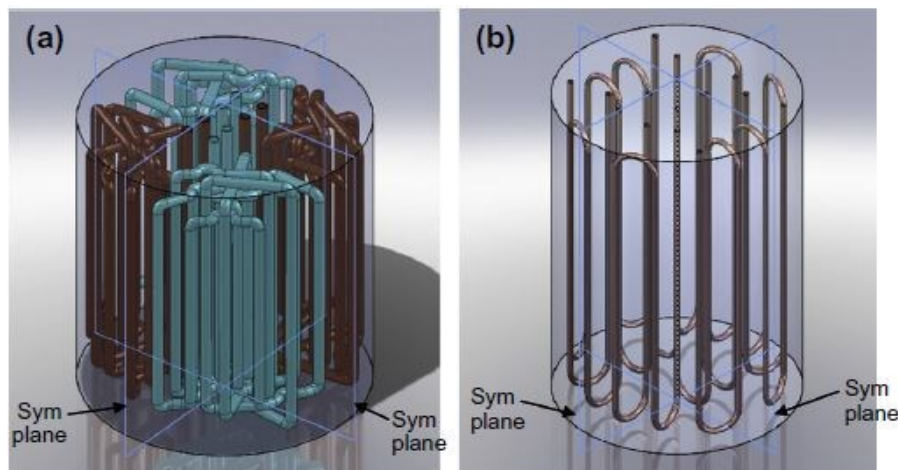
Figure 2.8 Schematic diagram of TES device with pinned tubes [119, 120].
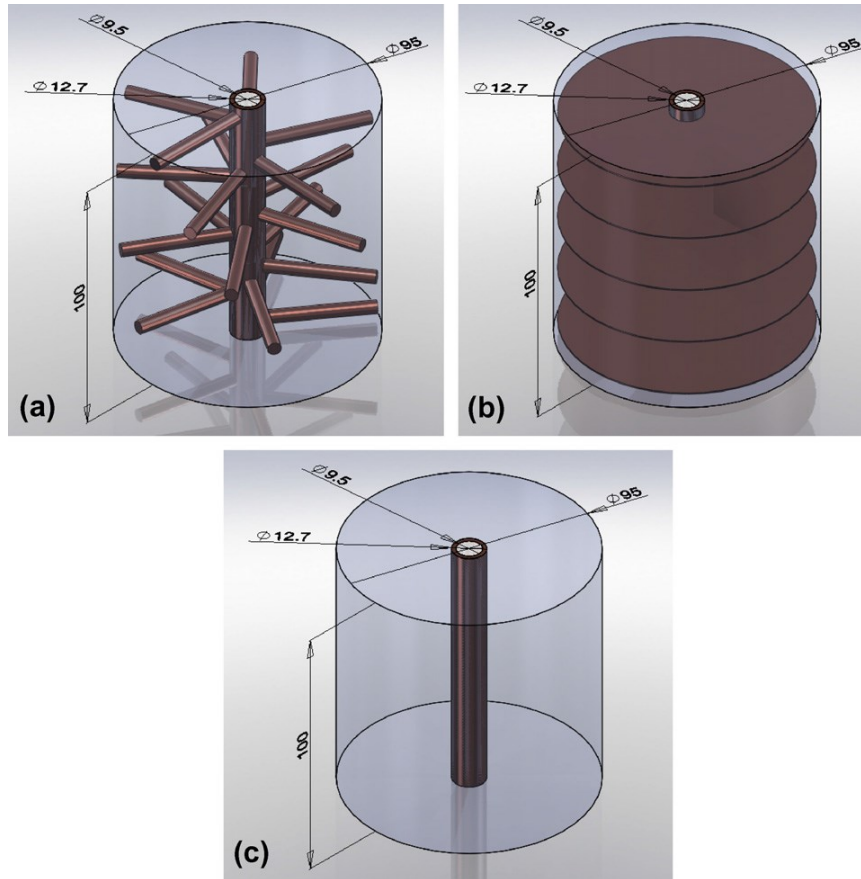
Figure 2.9 Schematic representations of a cylinder TES device with (a) pinned tubes, (b) finned tubes and (c) plain tubes [122].

Cakmak [123] experimentally investigated the thermal behaviour of a U-tube TES device containing cylindrical components (Figure 2.10). Calcium chloride hexahydrate with a phase change temperature of 29 ℃ was selected as PCM and water was used as HTF (Figure 2.10). They found that 588 kJ and 417 kJ heat were stored at two HTF inlet temperatures of 65 ℃ and 45 ℃, respectively.

Kurnia *et al.* [124] and AL-Khaffajy and Mossad [125] numerically studied heat transfer performance of a rectangular TES device containing U type component (Figure 2.11). Their results showed that the novel design provided highest heat transfer performance followed by U-tube with fins. U-tube with staggered fins performed better as compared to U-tube with in-line fins.

Zukowshi [126] presented a boat shaped TES device and experimentally studied its thermal behaviour with paraffin as PCM, as illustrated in Figure 2.12. He found that the proposed TES device containing paraffin wax (RII-56) can be successfully used in TES applications for processes and buildings. The heat transfer performance depended on HTF flow rate and PCM temperature change.

Shon *et al* [127] designed a finned rectangle TES device for receiving waste heat from coolant using xylitol as PCM (Figure 2.13) and analysed its heat transfer performance. Their results indicated that the absorption efficiency of the device was more significantly influenced by the coolant flow rate than by the temperature, and the influence of the coolant flow rate was related to the convective heat transfer inside the tubes.
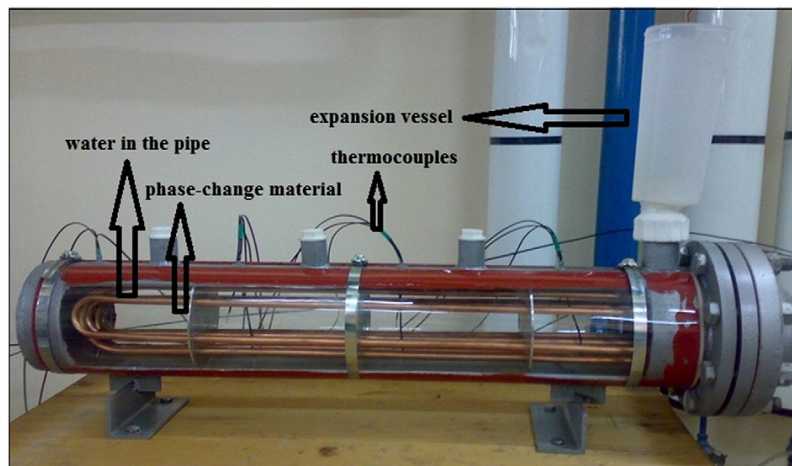
Figure 2.10 U-tube device containing cylinder component [123].
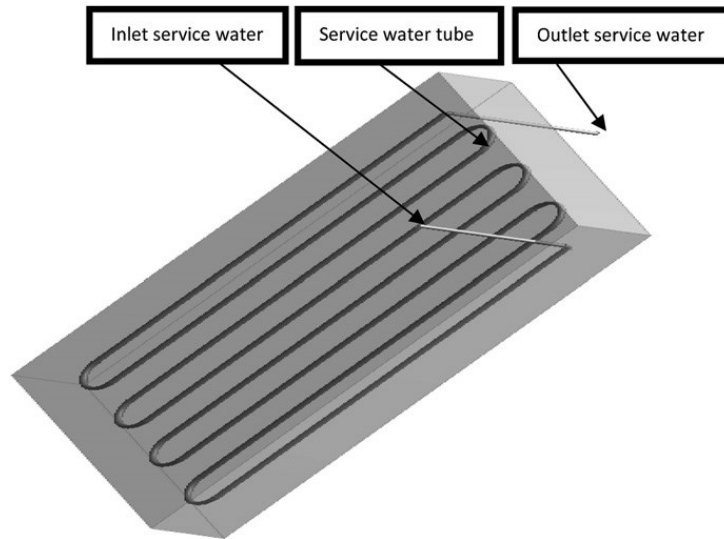
Figure 2.11 U-tube based rectangular device [125].
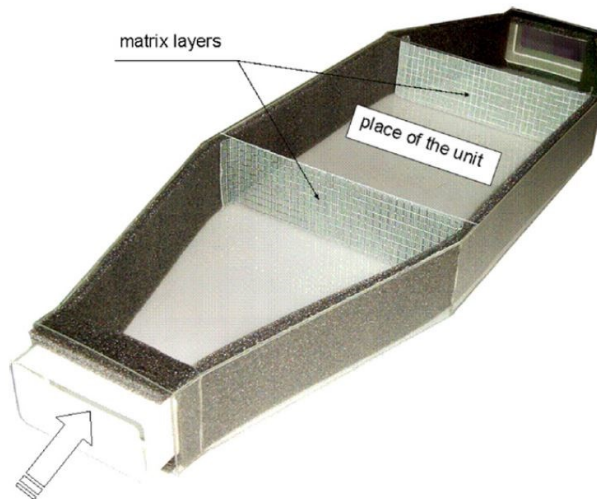
Figure 2.12 Boat shaped TES device [126].

Figure 2.13 Finned rectangle TES device [127].

Gil *et al.* [128] proposed a rectangular TES device containing U shape tubes for solar cooling and refrigeration applications, and experimentally analysed its thermal behaviour with hydroquinone as PCM and therminol VP1 as HTF; see Figure 2.14. They calculated the average effectiveness of the device and compared it with empirical modelling results in the literature, and found that the effectiveness described an important design specification of the device and increased with decrease of HTF flow rates.
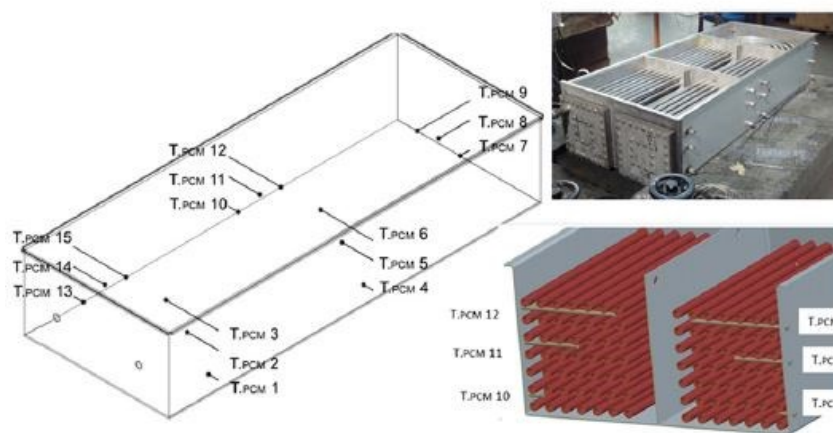
Figure 2.14 Rectangular TES device containing U shape tubes [128].

Rouault *et al.* [129] developed a one-dimensional numerical model to simulate the charging and discharging phenomena inside a rectangular TES device containing squared tubes, as illustrated in Figure 2.15. Paraffin wax was selected as the PCM and air was used as the HTF. An experimental set up was built to validate the modelling approach. Their results showed that modelling results had a good agreement with experimental data. Heat transfer coefficient between the PCM and the tubes depended on the downstream state of melting at a given point of the device.
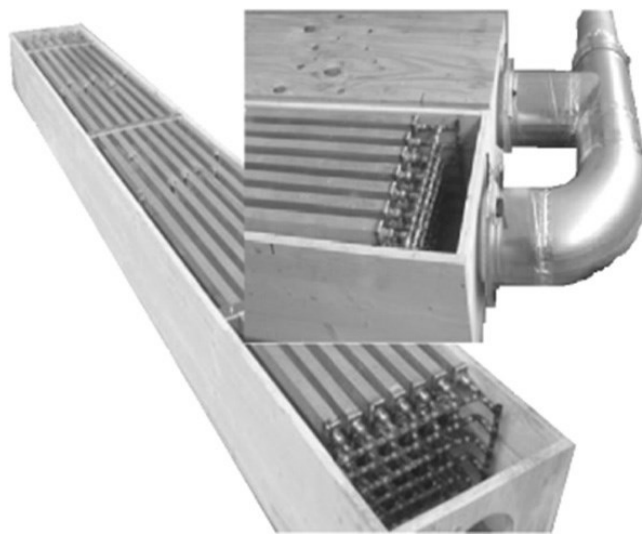
Figure 2.15 Rectangular TES device containing squared tubes [129].

2.4 Summary of the literature review

A wide variety of studies focusing on the TES technologies from materials to components and devices levels are presented in the literature. For the TES technologies to be more competitive and effective, a number of technological and scientific challenges need to be addressed at both materials and device/system scales. For TES materials, the challenges are associated with improving the properties including energy storage density, thermal conductivity, lifespan, operation temperature range and mechanical strength under large

temperature swings as well as cost reduction. Fabrication of TES devices and systems at scales that can deliver the properties at the materials scale are among other challenges. The use of microstructured CPCMs could provide an effective way to meet TES material level challenges. The CPCMs consist of a PCM, a TCEM and a CSM for shape stabilization. Such a combination gives an excellent combination of energy density, power density and mechanical properties. Understanding of the relationship between materials properties and microstructures is essential for the formulation design and manufacture process of CPCMs, however, it is insufficient as the TES devices and systems may not be able to deliver the properties at the materials scale and little work has been done in this respect. This forms the motivation of a systematic study on TES system level performance to TES materials properties and implies fundamental understanding of multiscale multiphase physics across a large length scale. The work presented in this thesis forms part of the efforts. It concerns the relationship between TES device level performance to TES materials properties using CPCMs.

Chapter 3 Wettability of carbonate salt on MgO

This chapter aims to understand the wettability behaviour of carbonate salt on MgO substrates through the measurements of contact angle. The effects of two important factors on the contact angle were studied: (a) penetration of carbonate salt into MgO substrate, and (b) surface tension of the salt changes on the MgO substrate. Scanning electron microscopy with energy dispersive X-ray spectrometry (SEM-EDS) and Atomic force microscopy (AFM) were used in the study. The results are useful for guiding the fabrication of MgO based CPCMs and the understanding of microstructural characteristics of the fabricated composite materials.

3.1 Introduction

Industrial needs for TES materials with high energy and power density, good mechanical strength, and long life span has led to significant interest from both scientific and industrial communities [41-43]. As explained before, CPCM can meet the needs, which consist of a PCM, a CSM and a TCEM. Such materials can be fabricated by using two methods of physical mixing and vacuum infiltration [9, 10, 44]. For either of the methods to be successful, the wettability of liquid PCMs on CSMs plays a crucial role. This calls for an in-depth understanding of the wetting behaviour liquid PCMs on CSMs. Such understanding is important not only for the formulation of the CPCMs, but also for the predication of microstructural characteristics of the materials.

Numerous PCMs can be utilized for the fabrication of the CPCMs. Examples include fatty acids and paraffin waxes with low melting temperature, and molten salt (carbonates, nitrates and sulphates) with medium to high melting temperature [30-46]. There are also a number of materials that may be used as CSMs, including diatomite, magnesium oxide, expanded graphite and silicates [47-57, 130]. This work focus on the use of MgO as the CSM and carbonate salt as PCM, which are mainly for medium and high temperature TES applications. The wettability of a molten salt on a CSM depends on the interfacial energies between three phases involved solid/vapour, solid/liquid and liquid/vapour. According to the Young's equation [9], the contact angle for a molten salt on a smooth MgO substrate can be described as: $\cos\theta = (\sigma_{sv} - \sigma_{sl})/\sigma_{lv}$, where θ is the contact angle of solid and liquid phase, σ is the interfacial energy, and subscripts sv, sl and lv denote respectively solid/vapour, solid/liquid and liquid/vapour interfaces.

Very limited work has been carried out so far on the wettability of molten salts on ceramic material substrates [10]. This forms the motivation for the work of this chapter. This research focuses on the influences of two factors on the contact angle: (a) penetration of carbonate salt into MgO substrate, which may change the contact angle dynamically, and (b) surface tension changes due to different fabrication temperatures. Scanning electron microscopy with energy dispersive X-ray spectrometry (SEM-EDS) and Atomic force microscopy (AFM) were used in the study.

3.2 Experimental

3.2.1 Preparation of carbonate salt samples and MgO substrates

The salt samples used in this study were made with eutectic carbonate salt ($NaLiCO_3$), which were in cylinder (rod) shape and had a mass of approximately 50 mg. The eutectic salt contained 50 wt% Li_2CO_3 and 50 wt% Na_2CO_3. The samples were made by thoroughly mixing the two salts followed by shaping in a cylindrical mould with diameter of 4 mm. MgO substrates used were either a sintered or a non-sintered cylindrical plate with dimension of 13 mm diameter and 4 mm thickness. The sintered MgO plates were sintered at 1000 ℃. One flat surface of the plates was polished to give a mirror finish using various grades of SiC abrasive papers and three grades of diamond pastes (with particle diameters of 6, 3 and 1 μm) to an average surface roughness of 300-400 nm as measured by a surface profilometer (KLA Tencor MicroXAM 2) over a length of 150 μm at a speed of 20 μm/s. The substrates were carefully cleaned in acetone using an ultrasonic machine before placed wettability experiments.

3.2.2 Experimental apparatus and measurement methods

A high temperature drop shape analyser (Kruss, DSAHT17-2) was used to investigate the wetting behaviour of carbonate salt on MgO substrates. The device is based on the sessile drop method. Figure 3.1 shows a schematic illustration and an image of the experimental apparatus.
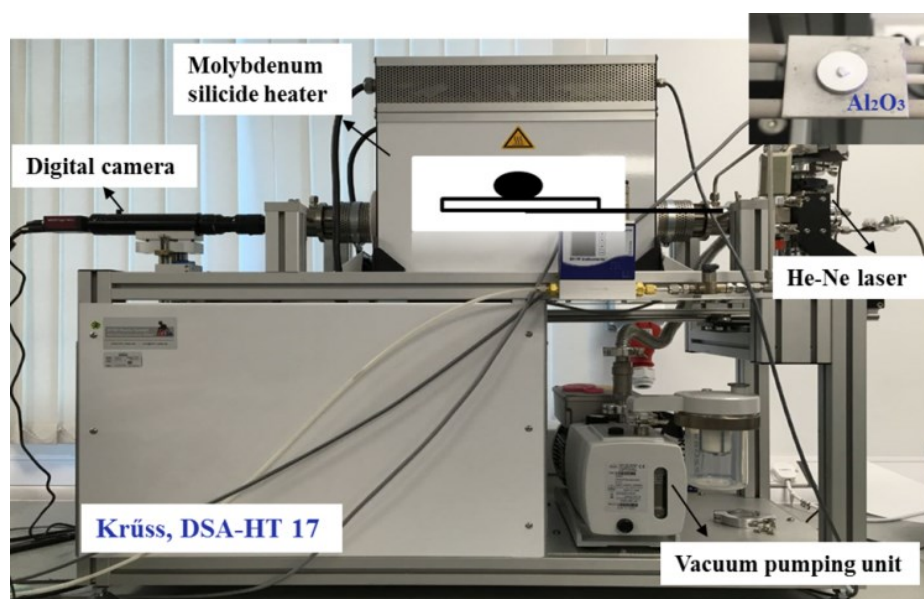
Figure 3.1 A schematic illustration and a photograph of the sessile drop test apparatus.

The analyser consists of a molybdenum reflector installed in a sealed chamber, a molybdenum silicide heater, an aluminium oxide supporting tube and a sample holding platform, a type B thermocouple, a vacuum pumping unit with a rotary pump and a turbo molecular pump, a programmable temperature controller, a He-Ne laser and a high-resolution digital camera. Prior to a test, a salt cylinder was placed on the top of MgO substrate, and followed by placing the salt-MgO sample on the sample holding platform. The platform was then adjusted to a horizontal position, and inserted into the centre of the chamber. A high purity nitrogen stream was then switched on to flow into the chamber followed by heating up sample to a preset temperature at a heating rate of 10 K/min. After the sample temperature

reached the measurement temperature, the N_2 gas supply was cut off. As soon as the sample began to melt, the digital camera was started to capture the image of the salt sample, which was used as the initial drop profile. Subsequently images were taken every 5 seconds and the images were analysed using the drop-analysis software to obtain the contact angle, drop height and contact diameter. Each experiment was repeated at least twice to study the repeatability. In order to investigate the effect of infiltration of the carbonate salt into MgO substrates on the wettability, a 10mm×10mm single crystal MgO (100) plate (Sigma-Aldrich Co. LLC, UK) was used, which had a purity of 99.9% and a relative density over 96%. A SEM with EDS was used to investigate the microstructures at and near the triple point as well as the interface between the carbonate salt and the MgO substrate after the salt solidified. The surface morphology was measured by an atomic force microscope (AFM, NanoWizard III NanoScience).

3.3 Results and discussion

3.3.1 Contact angle and drop dimension

Figure 3.2 shows the time evolution of the contact angle (θ) and the droplet diameter (D) and height (H) for the carbonate salt on the non-sintered MgO substrate at a measurement temperature of 778 K. It can be seen that the contact angle and drop dimension change with time, and the change can be divided into three stages of (a) initial stage, (b) spreading stage, and (c) steady state stage. The initial stage could be regarded as the equilibrium stage since the contact angle and the droplet dimension are almost constant, and the spreading velocity is very low as the salt sample just starts to melt. In stage (b), both the contact angle and droplet height decrease whilst the droplet diameter increases, indicating the spreading of droplet on the triple line as carbonate-MgO is a non-reacting system [9, 10]. In stage (c), the contact

angle and droplet dimension are almost constant, indicating the constraint of energetic equilibrium on the substrate surface.
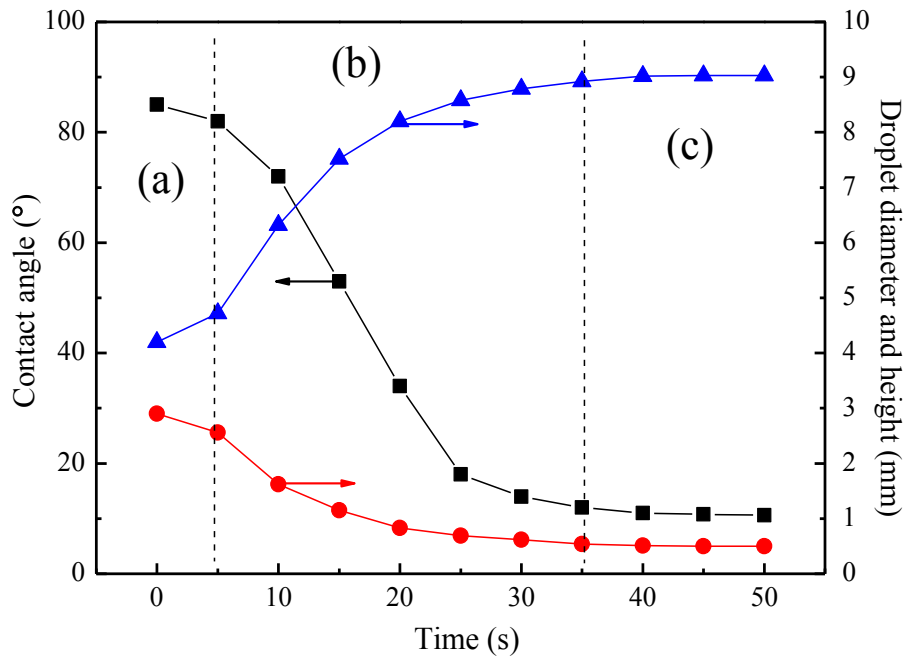
Figure 3.2 Time evolution of contact angle and droplet dimension of carbonate salt on a non-sintered MgO substrate.
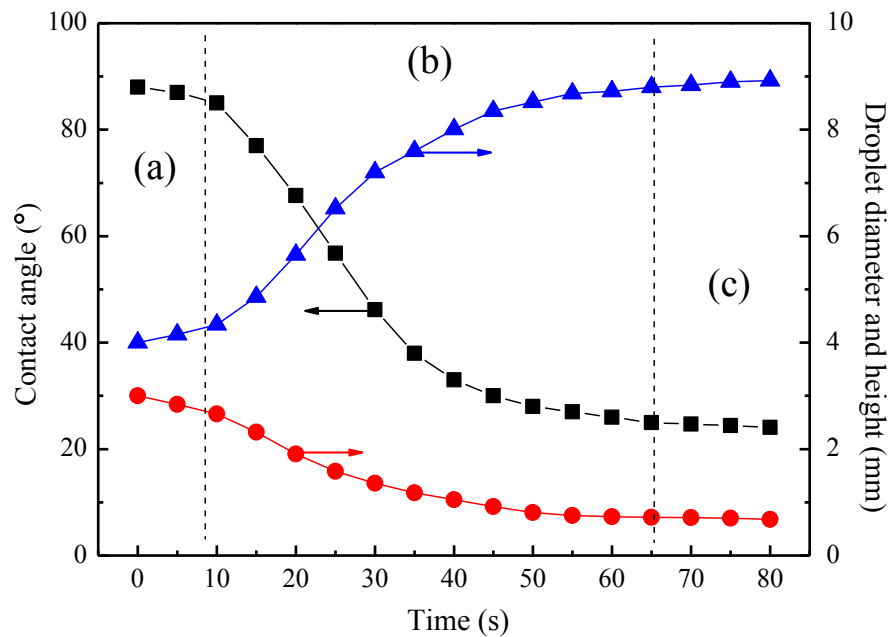
Figure 3.3 Time evolution of contact angle and droplet dimension of carbonate salt on a sintered MgO substrate.

Figure 3.3 demonstrates the contact angle and droplet dimension of the carbonate salt droplet on a sintered MgO substrate. One can see three clear stages of the spreading process, similar to the observation of the carbonate salt drop on the non-sintered MgO substrate. However, the durations of the first two stages are far longer compared with that of the non-sintered MgO substrate: stage (a) lasts ~8 s (~5 s for the non-sintered case) and stage (b) is ~57 s (~30 s for the non-sintered case). The equilibrium contact angle approaches ~25° (~12° for the non-sintered case). These observations indicate that the wettability of carbonate salt on the sintered substrate is lower than that on the non-sintered substrate. The enhanced wettability is likely due to the salt infiltration into the MgO substrate, which will be discussed in Section 3.3.2.

3.3.2 Salt infiltration

The salt infiltration was studied by using SEM-EDS. Figure 3.4 shows typical top-view SEM images of both non-sintering MgO and sintered MgO substrates. Coarse particles are seen on the non-sintered MgO substrate, which are non-uniformly distributed. Although uniaxial compression and polishing processes were applied during SEM sample preparation, some cavities and crevices of ~3-5 μm are apparent. Fine particles are seen to distribute uniformly and densely packed on the sintered MgO substrate although there are still some micro crevices with ~ 0.5 μm diameter (Figure 3.4 (b)). As a result, liquid carbonate salt is more likely to penetrate into the non-sintered MgO substrate.
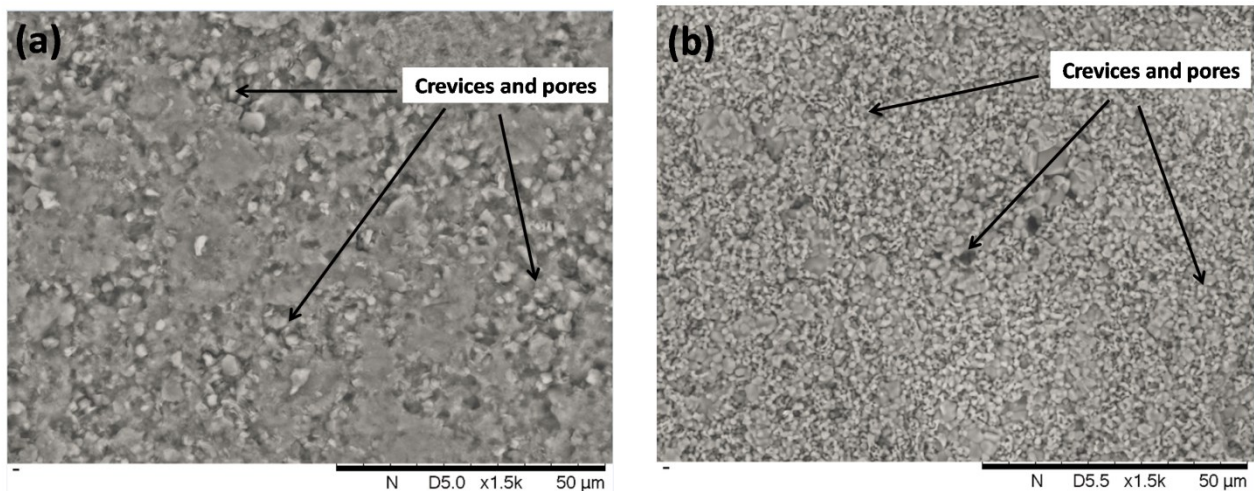
Figure 3.4 SEM images of non-sintered (a) and sintered (b) MgO substrates.

This agrees with the following Washburn's equation [131]:

$$h_i^2 = \frac{r\sigma_{lv}\cos\theta}{2\mu}t \qquad (3.1)$$

where r is the radius of capillary or pores, σ_{lv} is the surface tension, θ is the contact angle, μ is the viscosity and t is the time taken to reach an infiltration height of h. Equation (3.1) applies to cases with high wettability and acute contact angle. This is indeed the case for the carbonate salt on both sintered and non-sintered MgO substrates. Equation (3.1) also indicates that the infiltration of carbonate salt on non-sintered Mgo substrate should be more significant than that of sinter MgO substrate due to larger pore sizes.

Figures 3.5 and 3.6 show SEM-EDS images and analyses of the interface between MgO substrate and the carbonate salt. Considerable salt infiltration into the MgO substrate is evident, particularly for the non-sintered MgO substrate (Figure 3.5) where an infiltration depth of ~ 1.5 mm can be observed, significantly larger than that for the sintered MgO substrate (~ 0.5 mm , Figure 3.6). Such difference could be explained from two aspects: One is that the size and number of crevices and pores of non-sintered MgO substrate are larger than that of sintered MgO substrate, as shown in Figure 3.4. The other is that the specific structure of the sintered MgO substrate, which may hinder the salt penetration. As illustrated in Figure 3.4 (b), the sintered MgO substrate is in the early stage of sintering process with individual particles still visibly distinguishable [132, 133] and sintering necks starting to growth [133]. The sintering of MgO particles forms a rigid microstructure that could confine and hence prevent the motion of liquid carbonate salt into the substrate.
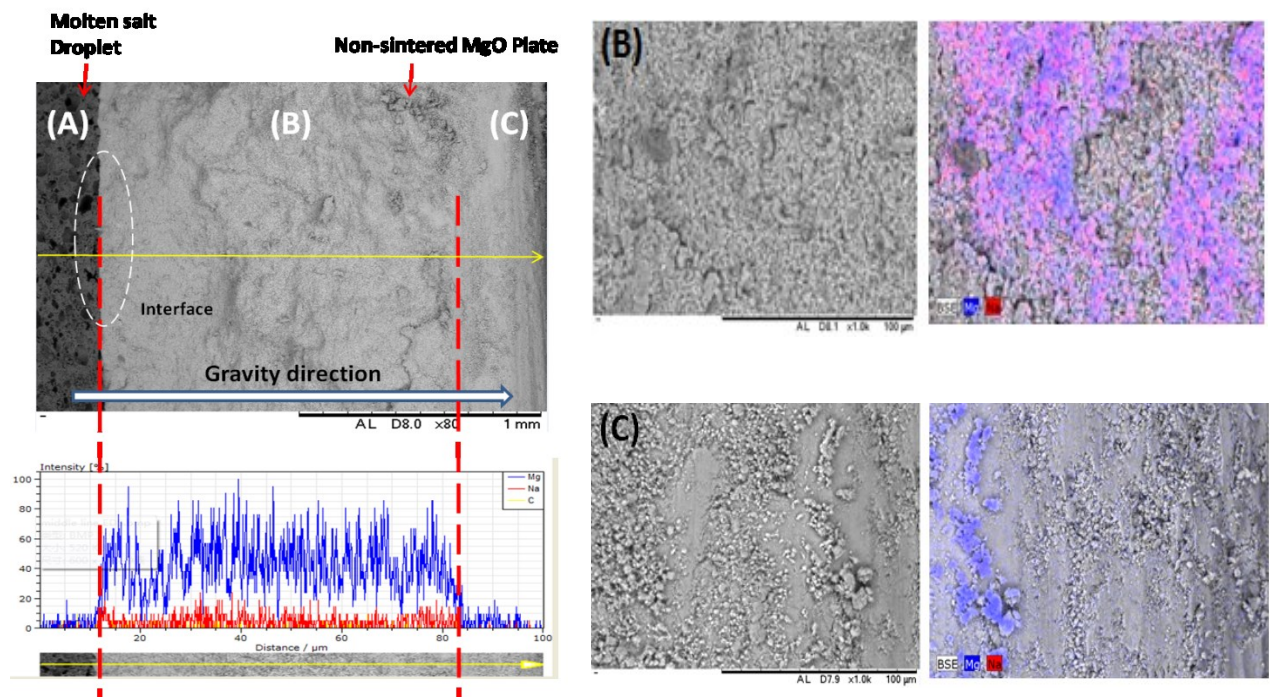
Figure 3.5 SEM-EDS analysis of the interface between carbonate salt and non-sintered MgO substrate: (A)-carbonate salt droplet; (B) and (C)-non-sintered MgO substrate.
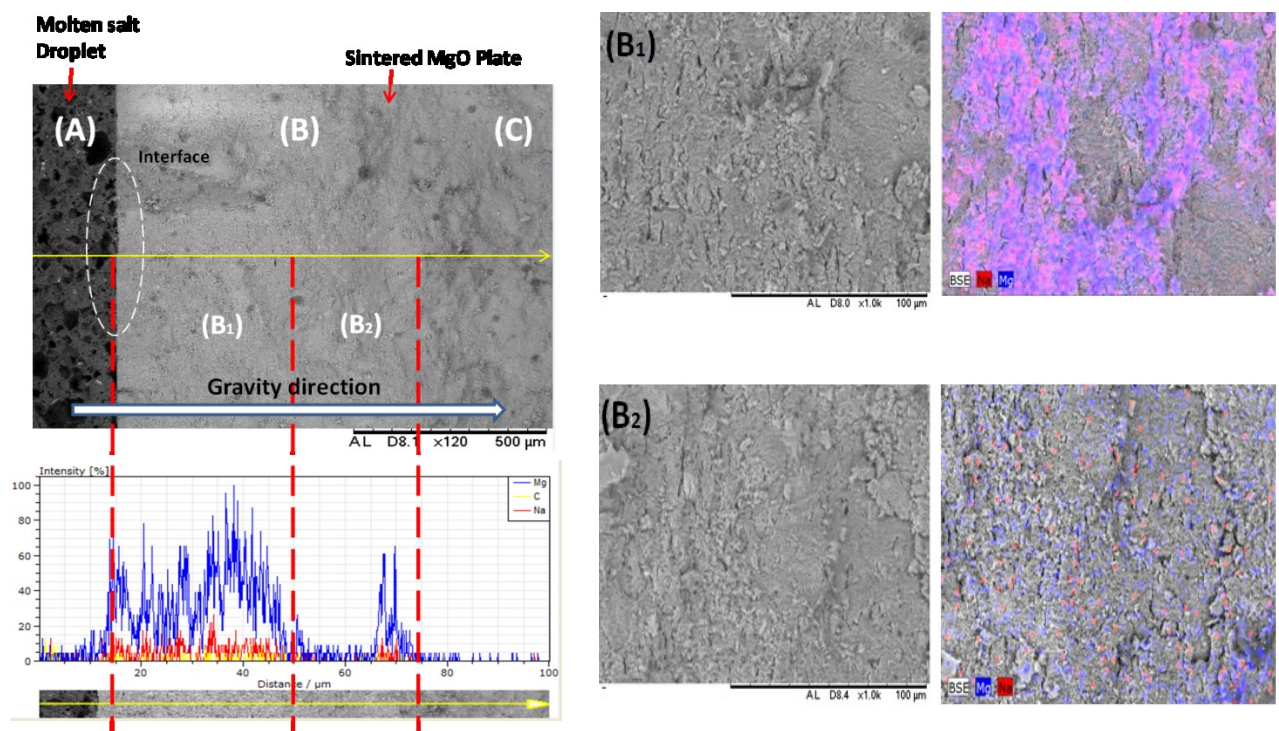
Figure 3.6 SEM-EDS analysis of the interface between carbonate salt and sintered MgO substrate: (A)-carbonate salt droplet; (B) and (C)-sintered MgO substrate.

3.3.3 Effect of substrate on the contact angle

As illustrated in the previous sections, the extent of salt infiltration increases with increasing wettability, which leads to a decrease in the droplet volume on the substrate, and hence influence on the measured contact angle. In other words, the actual contact angle is different from the measured value. Therefore, the effect of infiltration should be taken into consideration when studying this sort of liquid-substrate combination.
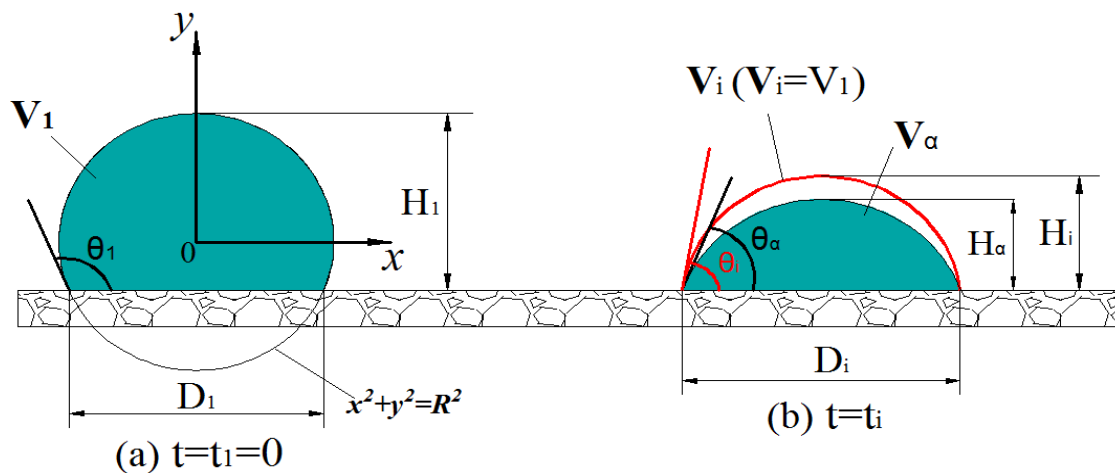
Figure 3.7 Schematic illustration of changes of a carbonate salt droplet on a MgO substrate due to infiltration (Red line in (b) denotes the contour of salt droplet without infiltration).

Quantification of the effect of salt infiltration on the contact angle could be evaluated by using the evaporation method proposed by Kondoh *et al.* [134]. For doing so, the salt droplet is assumed to be part of a sphere with radius R and the infiltration has no effect on the wetting test. Under those assumptions, the volume of salt droplet on the substrate should be constant and does not change with the time during the test; (see the red line which denotes the droplet contour without the effect of infiltration, $V_i=V_1$). This is illustrated in Figure 3.7.

The volume of the carbonate salt drop at any moment on the substrate ($V_i=V_1$) and the contact angle at t=0 can be expressed by:

$$\sin\theta_1 = \frac{D_1}{2R} \tag{3.2}$$

$$V_1 = \int_{-(H_1-R)}^{R} \pi(R^2 - y^2)dy = \pi\left(\frac{D_1 H_1^2}{2\sin\theta_1} - \frac{H_1^3}{3}\right) \tag{3.3}$$

where V_1, D_1, H_1 and θ_1 are respectively the salt droplet volume, droplet diameter, droplet height and contact angle at t=0; (see Figure 3.7a). The change in the droplet height and radius, and the contact angle at any moment can be then calculated by:

$$H_i^3 + \frac{3D_i^2 H_i}{4} - \frac{6V_1}{\pi} = 0 \tag{3.4}$$

$$R_i = \frac{V_1}{\pi H_i^2} + \frac{H_i}{3} \tag{3.5}$$

$$\theta_i = \sin^{-1}\frac{D_i}{2R_i} \tag{3.6}$$

Where H_i, R_i and θ_i are respectively modified droplet height, drop radius and contact angle at any moment. D_i denotes the experimentally measured droplet diameter, which, upon inserted into Equations (3.4)-(3.6), gives the modified droplet height, radius and contact angle. Figure 3.8 shows the modified contact angle under different conditions (non-sintered MgO, sintered MgO and single crystal MgO) taking into account of the salt penetration. Here, the use of single crystal MgO substrate is to show the result with no infiltration for comparative purpose. One can see significant effect of the substrate on the contact angle. For the non-penetration single crystal MgO substrate, the wetting and spreading process is far quicker than that with other two substrates, giving the final equilibrium contact angle of 38°. The contact angle of the carbonate salt on the non-sintered MgO and sintered MgO substrates are respectively 25° and 32°, considerably lower than that for the single crystal MgO plate.
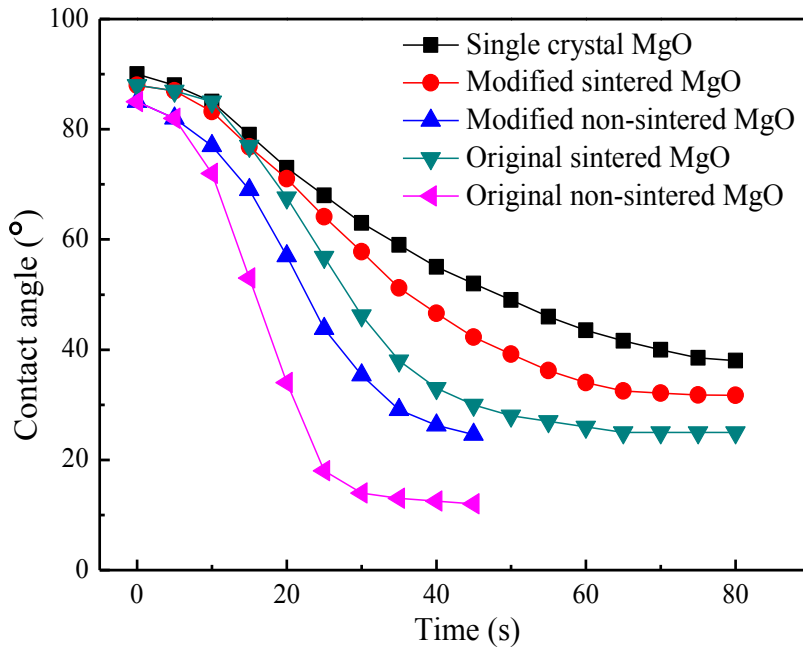
Figure 3.8 Effect of substrate type on the contact angle.

3.3.4 Surface energy measurements

The results presented in section 3.3.3 suggest that the substrate structure plays a key role in the wetting and contact angle of salt. The structure of the substrate very much depends on the sintering temperature should the substrate be made from powders-the cases in this study for both the sintered and non-sintered substrate. Single crystal MgO could also be made by sintering at very high temperature (~3000°C). Different substrate structures produced at different sintering temperature could mean different surface energies. As a result, an attempt is made in the following to explain the experimental observations of wetting and contact angle from the view point of surface energy.

At equilibrium, the contact angle depends on interactions between different phases, and can be described by the Young's equation [135]:

$$\cos\theta = \frac{\sigma_{sv} - \sigma_{sl}}{\sigma_{lv}} \tag{3.7}$$

For a given liquid phase, that is the carbonate salt of $NaLiCO_3$ in this study, σ_{lv} is constant, the difference between σ_{sv} and σ_{sl} is the only factor that determines the value of contact angle. Let σ be defined as the difference:

$$\sigma = \sigma_{sv} - \sigma_{sl} \tag{3.8}$$

Over the two interfacial tensions, σ_{sv} depends on the intrinsic property of the substrate, whereas σ_{sl} is due to the interaction between the carbonate salt and the substrate. Interfacial tension could be linked to intermolecular forces and polarity of the phases. For example, σ_{sl} could be given by [136]:

$$\sigma_{sl} = \sigma_{sv} + \sigma_{lv} - 2\left(\sigma_{sv}^d \cdot \sigma_{lv}^d\right)^{1/2} - 2(\sigma_{sv}^p \cdot \sigma_{lv}^p)^{1/2} \tag{3.9}$$

where the subscribes d and p denotes respectively the dispersion and polar contributions to the surface tension. In cases where only dispersion forces operate, the polar term goes and Equation (3.9) becomes the Fowkes equation [136]:

$$\sigma_{sl} = \sigma_{sv} + \sigma_{lv} - 2\left(\sigma_{sv}^d \cdot \sigma_{lv}^d\right)^{1/2} \tag{3.10}$$

Inserting Equation (3.10) to Equation (3.8) yields:

$$\sigma = 2\left(\sigma_{sv}^d \cdot \sigma_{lv}^d\right)^{1/2} - \sigma_{lv} \tag{3.11}$$

Equation (3.11) suggests that the interfacial tension difference be determined by σ_{sv} (the interfacial tension of solid and vapour phases), given the liquid-vapour interfacial tension (σ_{lv}). This implies that the contact angle depends on the interfacial energy between the

vapour phase and the measured solid surface. The salt on the non-sintered MgO substrate has the smallest contact angle as demonstrated before, indicating the greatest the substrate surface tension, which is exactly what was observed experimentally. This is also explains that the single crystal MgO substrate give the lowest surface tension. The above results also indicate that the sintering temperature plays an important role due to its effect on the structure of the substrate. To further investigate this, atomic force microscopic (AFM) analyses on the MgO substrates were carried out by using a Nanoscope III AFM with functionalised silica tips from Mikromasch. The measurements were done mainly on the adhesion force and principle of the measurements has been described elsewhere in the literatures [137-139]. Briefly, an AFM measures the cantilever deflection of the tip displacement due to its interaction with the substrate. The adhesion force can be calculated from the Hooke's law [140]:

$$F = k\Delta\varepsilon \tag{3.12}$$

where k is the spring constant of the cantilever calculated to be 0.179 N/m and $\Delta\varepsilon$ is the maximum cantilever deflection. Figure 3.9 shows the measured force-displacement curves for three MgO substrates. The insert in Figure 3.9 gives the adhesion forces for three substrates.
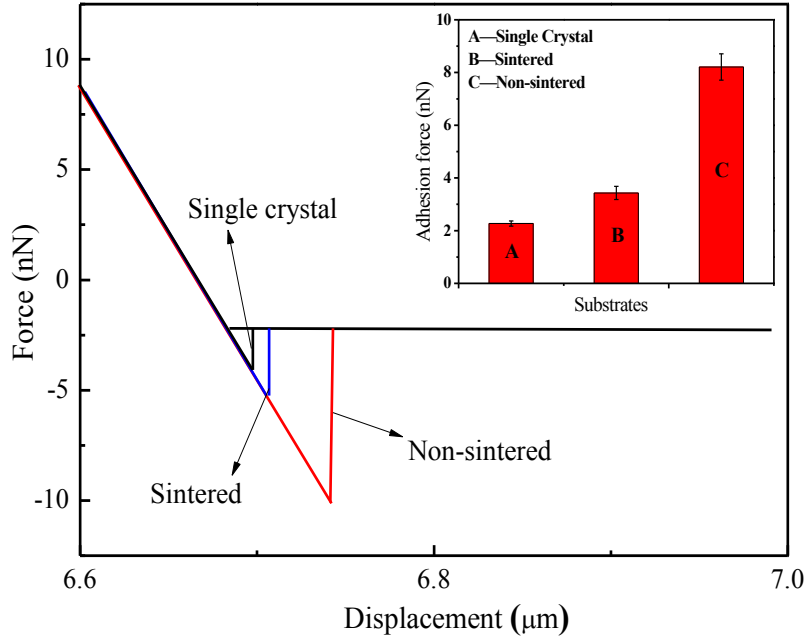
Figure 3.9 Typical force-displacement curves for the three MgO substrates. The inset summarises the average adhesion force for three MgO substrates.

One can see that the single crystal MgO substrate gives an adhesion force of 2.1 nN. Significantly larger adhesion forces are observed for both the sintered and non-sintered MgO substrates, with that for the non-sintered MgO substrate (~8.4 nN) nearly 2.5 times that for the sintered MgO substrate (~3.5 nN). The significant difference in the adhesion forces for the three substrates indicates the effect of different surface microstructural and possibly chemical characteristics.

The adhesion force between the tip and the substrate is the sum of several forces and can be expressed by [137]:

$$F = F_{el} + F_{vdw} + F_{cap} + F_{chem} \tag{3.13}$$

where F_{el}, F_{vdw}, F_{cap} and F_{chem} represent respectively the electrostatic force, Van der Waals force, meniscus or capillary force and chemical bond or acid-base interacting force. Under

the ambient conditions, the dominant adhesion force is the capillary force due to the formation of a liquid meniscus between the tip and the substrate [140]. Assuming that the AFM tip is a hemisphere with radius R in contact with the substrate, and liquid volume is negligible, the capillary force can be given by [140]:

$$F_{cap} = 2\pi\gamma_{lv}R(\cos\theta_1 + \cos\theta_2) \qquad (3.14)$$

where γ_{lv} is the surface tension at the liquid vapour interface, and θ_1 and θ_2 are the contact angles between the liquid and the tip, and the liquid and the substrate, respectively. Inserting of the above equation into equations (3.12) and (3.13) gives the contact angle of liquid and the substrate as:

$$\cos\theta_2 = \frac{kx}{2\pi\gamma_{lv}R} - \cos\theta_1 \qquad (3.15)$$

Equation (3.15) shows that the contact angle of the liquid and the substrate depends on the adhesion force; the larger the adhesion force, the smaller the contact angle will be. Equations (3.13) - (3.15) also indicate that the non-sintered MgO substrate has the highest surface tension in agreement with experimental observation presented in Section 3.3. As mentioned early, sintering temperature determines the microstructure of the MgO substrate given other conditions, and hence the surface energy and contact angle upon contacting the salt. More experiments were carried out on the MgO substrates sintered at different temperatures. Table 3.1 summarises the results. For comparison, the result for the single crystal MgO (3000 °C) is also listed. One can see that when the sintering temperature increases from 500 °C to 3000 °C, the contact angle increases from 25° to 40°.

Table 3.1 Contact angle of the carbonate salt on MgO substrates sintered at different temperatures*.

Sintering temperature (℃)	500	700	900	1100	1300	3000
Contact angle	25° (±1.7°)	25°(±1.8°)	32°(±1.6°)	32°(±1.8°)	34°(±1.7°)	40°(±1.8°)

* The effect of salt infiltration has been taken into consideration for all measurements. The data includes the best estimate and the standard error.

3.4 Conclusions of chapter 3

The wetting behaviour of carbonate salt on MgO substrate has been investigated through contact angle measurements at elevated temperatures. Both non-sintered and sintered MgO substrates were prepared for the study. For the sintered substrates, different sintering temperatures were applied, which ranges from 500 ℃ to 3000 ℃. For comparison purposes, a single crystal MgO substrate was also used in the study. To eliminate the effect of salt penetration on the contact angle, a calculation model is used to obtain true values of the contact angle. The results show good wettability of the carbonate salt on the MgO substrates and the wettability is a fairly strong function of microstructure and hence surface energy of the MgO substrates fabricated at different sintering temperature. The non-sintered MgO substrate has a loose surface particle packing with large pores and crevices, leading to significant salt infiltration. The corresponding contact angle is measured to be 25 °. The structure and morphology of sintered MgO substrates depends the sintering temperature given other conditions, the higher the sintering temperature, the finer the particles on the surface, the more homogenous particle distribution, and the smaller the size of the porous and

crevices on the substrate surface. At very high sintering temperature, e.g. 3000 ℃ (for MgO single crystal), the surface structure is very dense and smooth. The contact angle of the salt on the sintered MgO increases with increasing sintering temperature of the MgO substrate fabrication and approaches ~40° for the single MgO crystal. The effect of the sintering temperature for making the MgO substrate could be linked to the surface energy due to the surface microstructures. This is validated by the AFM measurements of the adhesion forces of the MgO substrates.

Chapter 4 Microstructure Characteristics and Development of CPCMs

This chapter studies the microstructure characteristics and formation mechanisms of CPCMs. Two CPCMs, eutectic carbonate salt based CPCMs and single carbonated salt based CPCMs were prepared and investigated. SEM and EDS were used in the study to measure salt distribution and redistribution within the composite structure during melting-solidification thermal cycles. The effect of TCEMs on the microstructural changes and the development of CPCMs were also investigated.

4.1 Introduction

Understanding the microstructural characteristics is essential for the establishment of structure-property relationship for CPCMs and hence the capability of design and fabrication of the material. This is also important for the predication of the thermophysical properties and performance of CPCM modules [6].

In this work MgO based carbonate salt CPCMs were used which are mainly for the medium and high temperature TES applications. The goal is to study the microstructure characteristics and structural changes during thermal cycles. Both a eutectic carbonate salt and a single carbonate salt based CPCMs were prepared and investigated. SEM and EDS were the main tools for the study, which measure time evolution of the salt distribution and migration within the composite structure during melting-solidification thermal cycles. The effect of the presence of TCEMs on the microstructure development of CPCMs was also investigated.

4.2 Experimental

4.2.1 Raw materials

The PCM used for the composite formulation was the eutectic carbonate salt (NaLiCO$_3$), made with 50 wt% sodium carbonate (Na$_2$CO$_3$, purity >99%) and 50wt% lithium carbonate (Li$_2$CO$_3$, purity >99%), both from Sigma-Aldrich Co. LLC, UK. The melting temperature of the eutectic salt is 500.35℃. Sodium carbonate (Na$_2$CO$_3$, purity >99%, Sigma-Aldrich Co. LLC, UK) was used for preparing the single sodium carbonate based composite. MgO (purity >95%, light magnesia, Sigma-Aldrich Co. LLC, UK) and natural graphite flake (Sigma-Aldrich Co. LLC, UK) were used as the CSM and TCEM, respectively, for the composite formulation.

4.2.2 Fabrication of eutectic carbonate salt based CPCM modules

The fabrication of the eutectic salt composite involved the following steps. Step 1 was thoroughly mixing sodium carbonate and lithium carbonate (50:50 ratio by mass) in a stainless steel crucible and followed by heating the sample in a furnace to 530 ℃ for 1 h. The carbonate mixture was then cooled down to the ambient temperature and milled to fine powder form. Step 2 was thoroughly mixing the milled eutectic carbonate salt with an appropriate amount of MgO and graphite flake, followed by shaping the powder mixture into disk-like pellets of 30 mm in diameter and 10 mm in thickness by uniaxial cold compression at 30 MPa for 1 min. In step 3, the green pellets were sintered under a N_2 atmosphere in an electrical furnace using the following profile: heating at 5 ℃/min between 25 and 100℃; holding at 100℃ for 60 min; heating further at 5 ℃/min between 100 and 550℃; and holding at 550 ℃ for 90 min; and finally cooling of the sample to ambient temperature with the reversed profile to the heating process.

4.2.3 Fabrication of single carbonate salt based CPCM modules

The fabrication process for the single carbonate salt based CPCM modules was the same as that for the eutectic carbonate salt based CPCM modules except for the sintering process. After the green pellets were made in step 2, the pellets were sintered under the N_2 atmosphere with the following profile: from heating at a rate of 5 ℃/min between 25 and 100 ℃; holding at 100 ℃ for 60 min; further heating at a rate of 10 ℃/min between 100 and 950 ℃; holding at 950 ℃ for 90 min; and cooling with a profile reverse to the heating process.

4.2.4 Characterization of the CPCM modules

The morphological and microstructural characteristics of the CPCMs modules were studied by using SEM-EDS (TM3030, HITACHI). The wettability studies were performed with the high temperature drop shape analyser (Kruss, DSAHT17-2) introduced in chapter 3. The thermal cycling tests were done by a self-constructed and automated device comprising of a high temperature region (1000℃) and a low-temperature region (20℃) with a perpendicular arrangement.

4.3 Results and discussion

4.3.1 CPCMs with no graphite addition

4.3.1.1 Morphological and microstructural observations

Figure 4.1 (a) and (b) show SEM images of green pellets made of powder mixtures of NaLiCO$_3$ and MgO, and Na$_2$CO$_3$ and MgO with uniaxial cold compression, respectively. A reasonably homogeneous distribution of salt and MgO can be observed for both sets of samples after the mixing process. The embedded image in Figure 4.1 (a) is a pellet made of pure MgO, which shows that MgO particles are approximately spherical in shape with a mean diameter of 3-5 μm, and there are plenty of voids formed between packed MgO particles. Figure 4.1 (a) shows that the salt occupies the voids of packed MgO particles forming the composite. Sintering of the composites changes the microstructure significantly, as shown in Figure 4.1 (c) for the NaLiCO$_3$-MgO composite. The salt experiences melting and recrystallization during heating and cooling processes, leading to the formation of a molten salt liquefied structure (MSLS) [10]. Such a structure plays an important role in retaining the salt and forming a dense structure. It is also noticed that apart from forming the

MSLS, MgO particles appear to have densified in the Na_2CO_3-MgO composite, with MgO particles coated by salt as shown in Figure 4.1 (d). Such structure difference between the two composites as shown in Figure 4.1 (c) and Figure 4.1 (d) could be attributed to both the interfacial energy between the different components of the composites, and the sintering temperature differences for the composites.
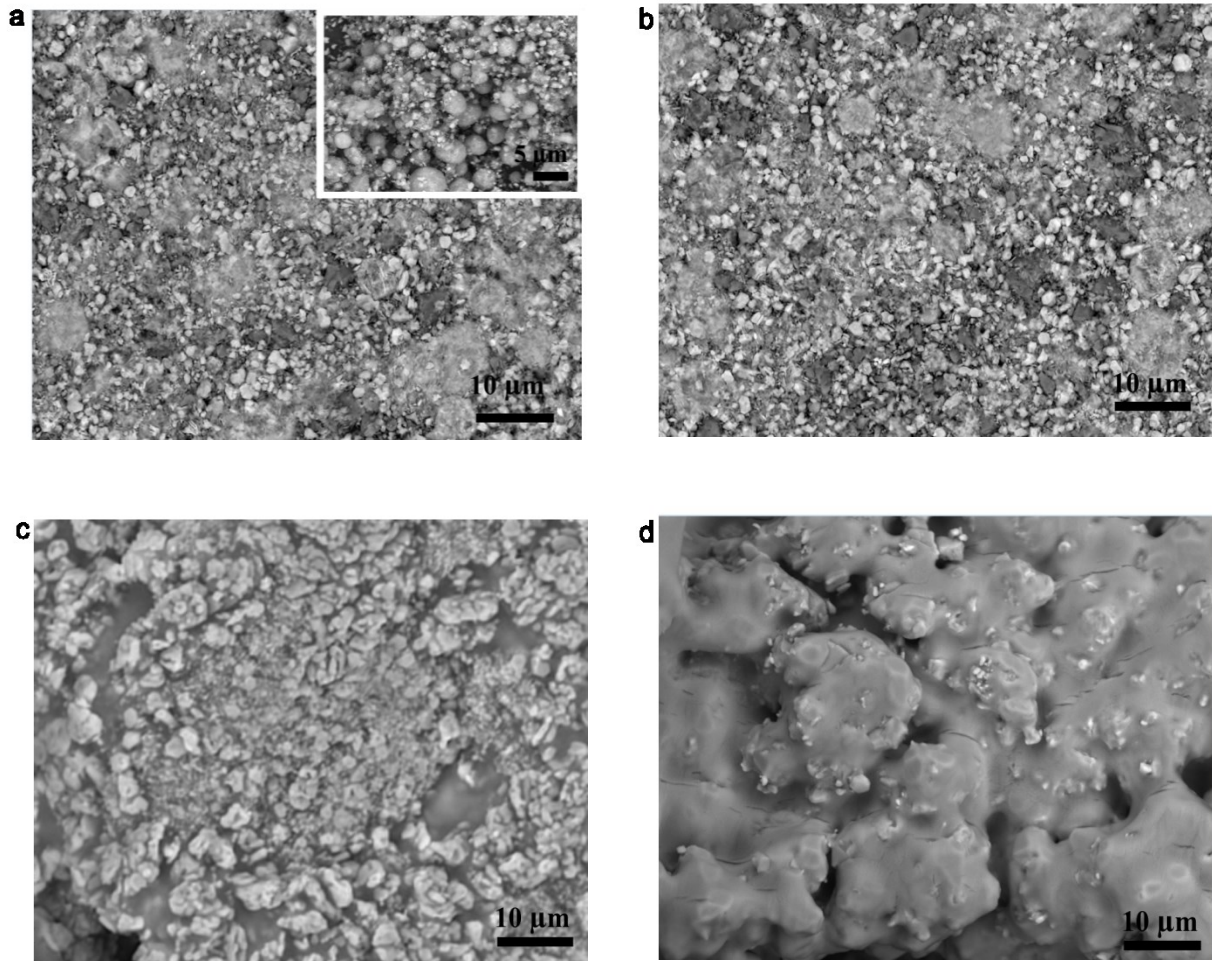
Figure 4.1 (a) SEM image of green pellet (non-sintered) of NaLiCO₃-MgO composite with a mass ratio of 1:1; inset is a SEM image of green pellet (non-sintered) made of pure MgO; (b) SEM image of green pellet of Na₂CO₃-MgO composite with a mass ratio of 1:1; (C) SEM image of sintered pellet of NaLiCO₃-MgO composite with a mass ratio of 1:1; (d) SEM image of sintered pellet of Na₂CO₃-MgO composite with a mass ratio of 1:1.

4.3.1.2 Particle distribution and migration during melting-solidification thermal cycles

Particle distribution and migration within the composite during thermal cycles were observed by SEM-EDS analyses. The two carbonate salt based CPCMs were used in the work. After the green pellets were made in the fabrication process, they were equally cut into two pieces. A rectangular area from the cross section of either half a piece was selected for the observation with a horizontal line being marked for quantitative analyse. Figure 4.2 illustrates the position and orientation of the observed area and line in the samples.
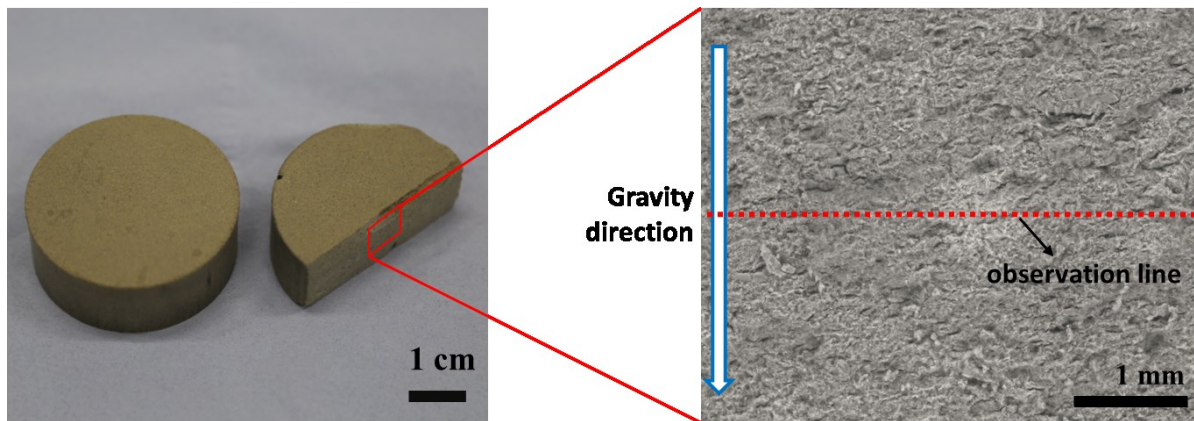
Figure 4.2 Illustrations of position and orientation of observation line (area) in the samples (Carbonate salts based MgO composites with mass ratio of 1:1).

Figure 4.3 shows element distributions in the observation area of the $NaLiCO_3$-MgO composite after 0 (green sample), 1, 10 and 50 heating and cooling cycles. These distributions were obtained from EDS mapping, which only gives Mg and Na maps. The EDS was unable to map Li distribution due to low atomic mass. Na and Mg maps give an indication of PCM and CSM distributions in the observation area within the composite. One can see that both the PCM and CSM are dispersed reasonably well within the green sample through physical mixing (Figure 4.3a). Sintering of composites leads to significant changes to

the structure and particle distribution (Figures 4.3b-4.3d). A number of pros/cavities appear during the first thermal cycle due to volume change as a result of phase change of the salt (Figure 4.3b). As melting-solidification thermal cycles go on, further change are seen in the particle distribution within the composites, as shown in Figures 4.3(c) and 4.3(d). The salt shows a tendency of moving downward in the observation area and the CSM seems to have moved with the salt.
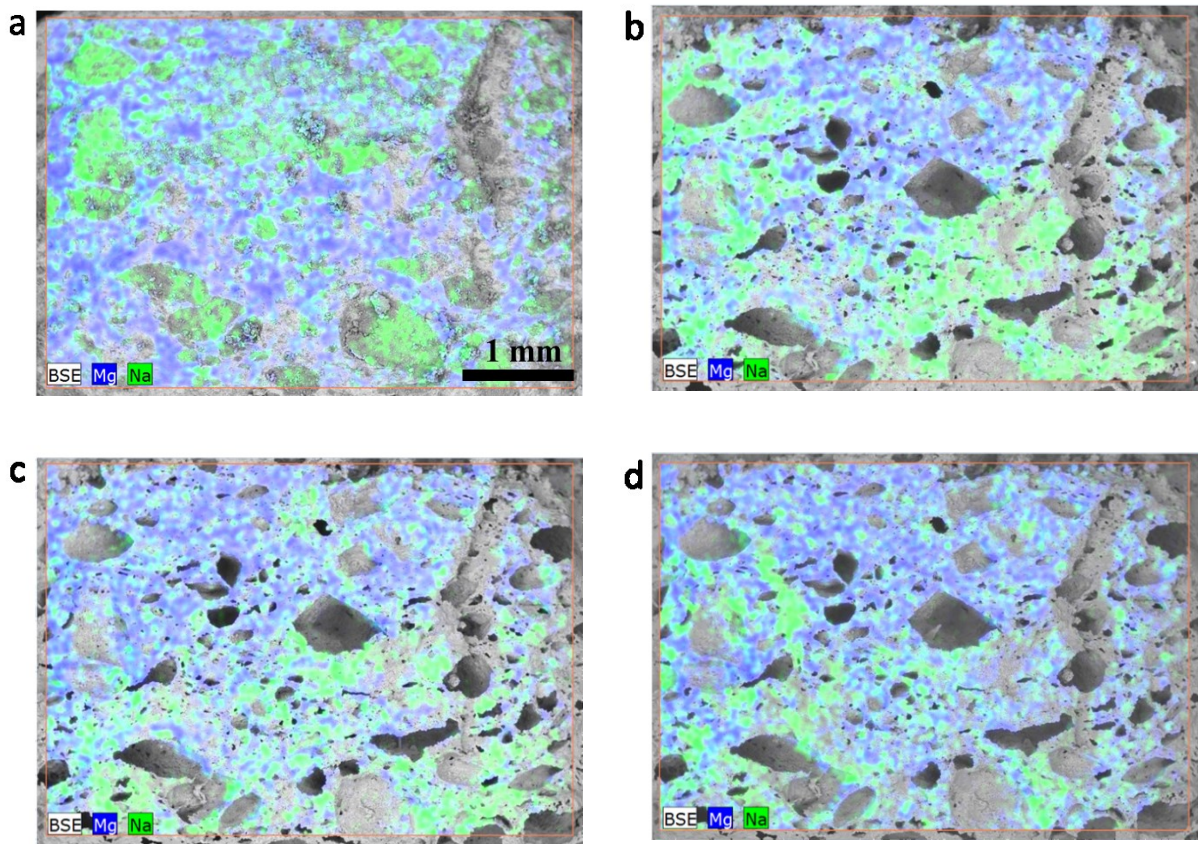
Figure 4.3 EDS element mapping micrographs of the observation area within the NaLiCO₃-MgO composite: (a) green sample (non-sintered), (b) after one heating and cooling cycle, (c) after 10 heating and cooling cycles and (d) after 50 heating and cooling cycles; blue and green colours represent Mg and Na, respectively.

Figure 4.4 shows particle concentrations in the observation area after different heating and cooling cycles. One can see that the particle concentration along the observation line changes with the melting-solidification thermal cycles. This is consistent with the qualitative analyses of the EDS mapping presented above. An attempt is made to explain the experimental observation in the following. When the temperature approaches the melting point during a melting-solidification thermal cycle, the solid salt turns into viscous liquid leading to flow of liquid salt in the pores. The flow is due to several factors including volume change due to phase change of the PCM, capillary force due to interfacial tension and gravitational force. Meanwhile, the liquid salt is wetted by the high interfacial energy CSM and provides a force to drag the CSM to move within the interparticle voids of the composite microstructure.
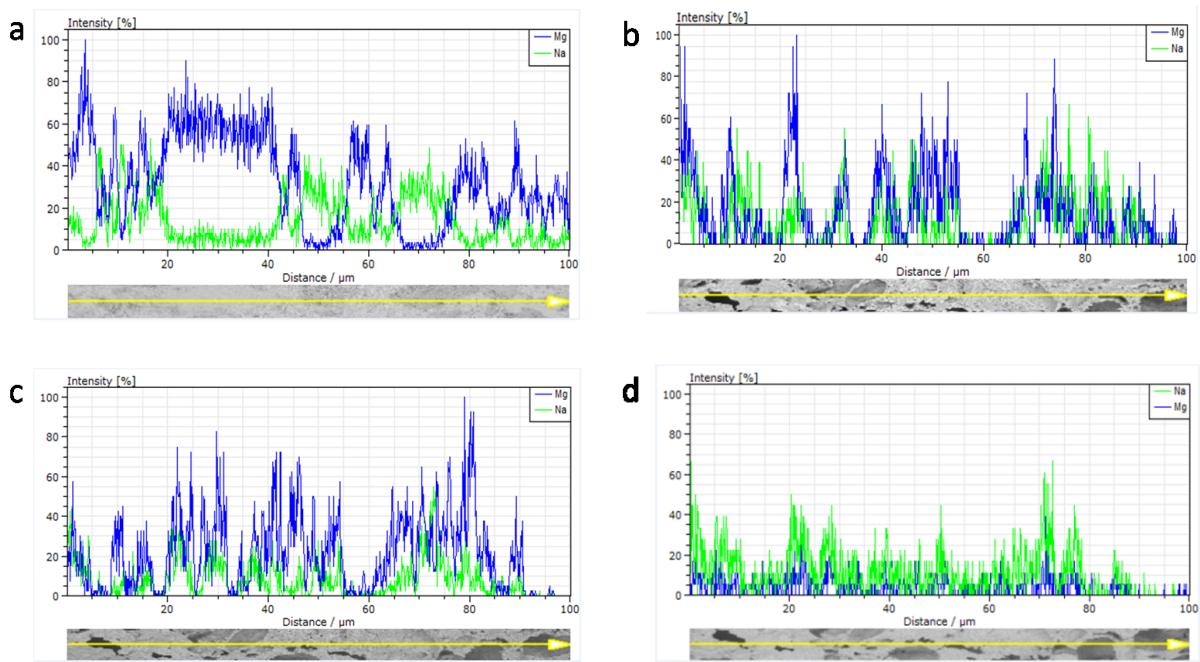
Figure 4.4 Element concentrations along the observation line within the NaLiCO₃-MgO composite: (a) green sample (non-sintered), (b) after one heating and cooling cycle, (c) after 10 heating and cooling cycles and (d) after 50 heating and cooling cycles; blue and green colours represent Mg and Na, respectively.

Figure 4.5 shows the EDS micrographs of element distributions in the observation area of the Na$_2$CO$_3$-MgO composite after 0, 1, 10 and 50 melting-solidification thermal cycles. The structure of green sample (Figure 4.5a) is similar to that for the green NaLiCO$_3$-MgO composite as shown in Figure 4.3a. However, significant changes are observed after first thermal cycle, the observed are seems to be covered mostly by the salt, represented by Na, and only a small amount of element Mg is detected. More thermal cycles give insignificant changes.
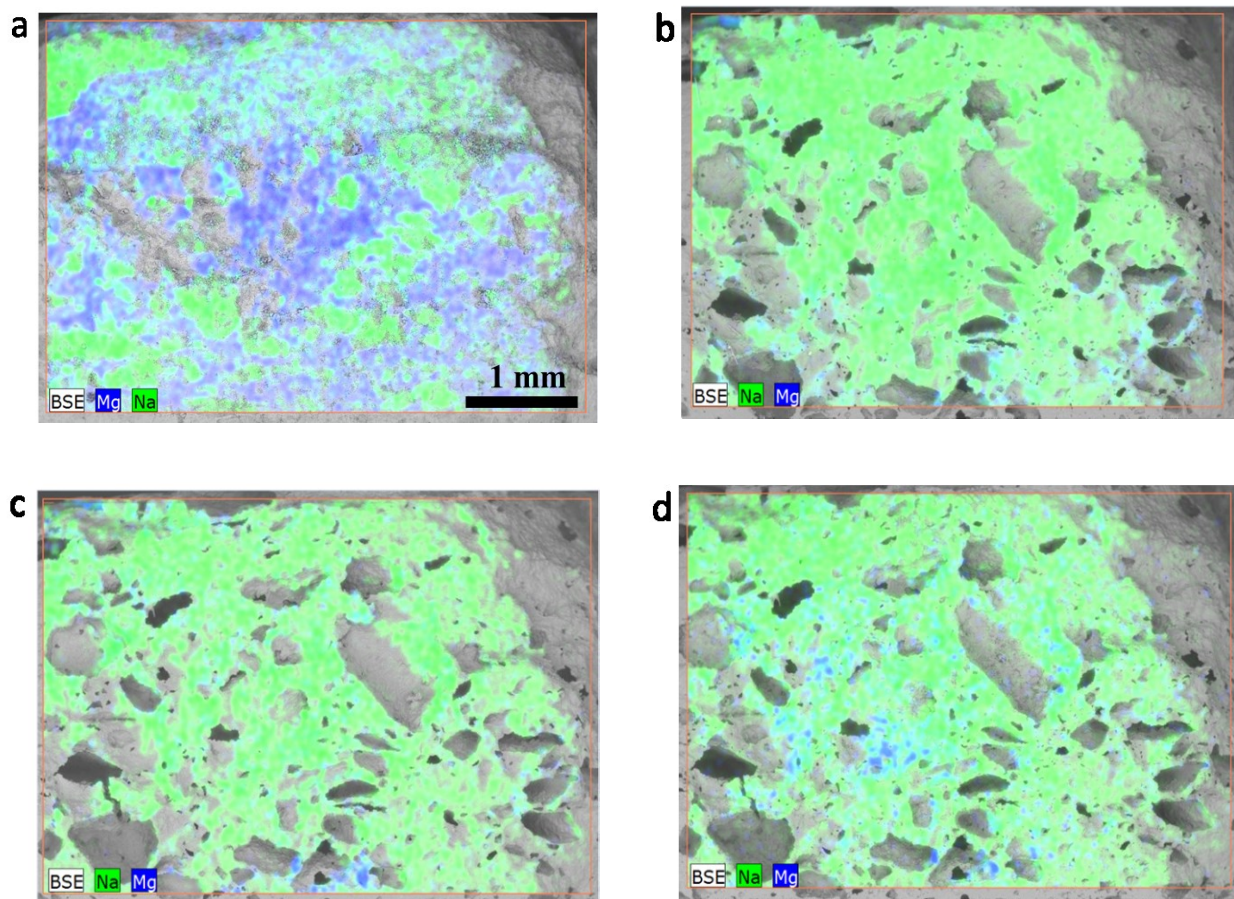
Figure 4.5 EDS element mapping micrographs of the observation area within the Na$_2$CO$_3$-MgO composite: (a) green sample (non-sintered), (b) after one heating and cooling cycle, (c) after 10 heating and cooling cycles and (d) after 50 heating and cooling cycles; blue and green colours represent Mg and Na, respectively.
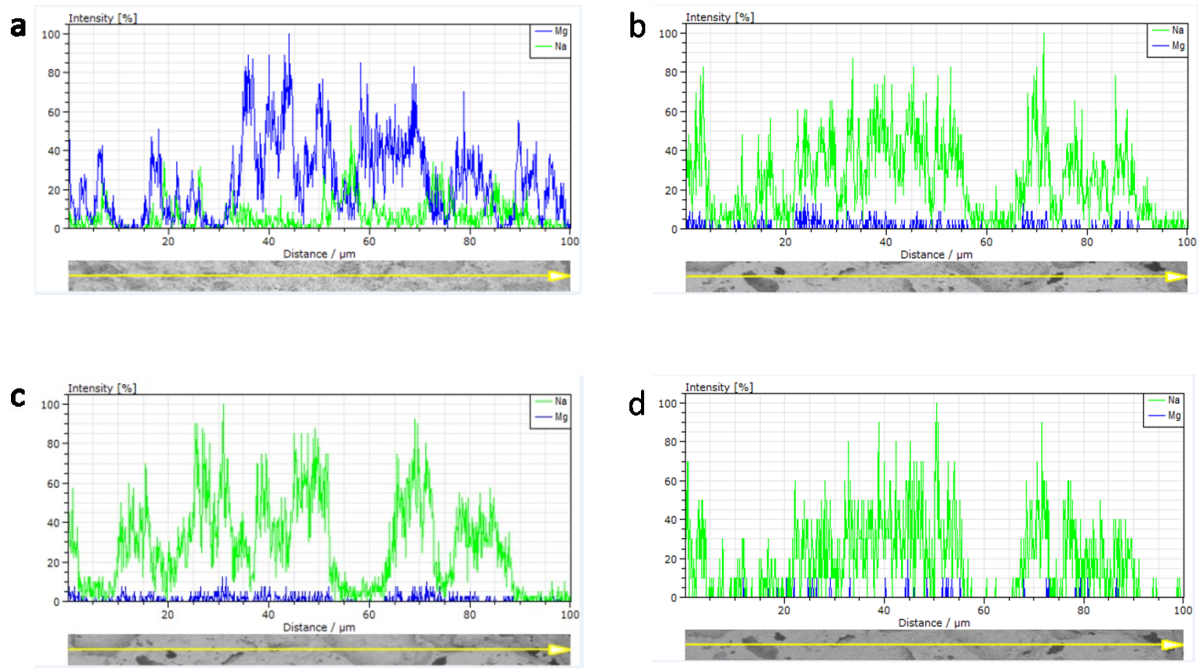
Figure 4.6 Element concentrations along the observation line of the Na₂CO₃-MgO composite: (a) green sample (non-sintered), (b) after one heating and cooling cycle, (c) after 10 heating and cooling cycles and (d) after 50 heating and cooling cycles; blue and green colours represent Mg and Na, respectively.

Figure 4.6 shows particle concentrations along the observation line of the Na_2CO_3-MgO composite after different melting-solidification thermal cycles. High MgO concentration (represented by high Mg intensity) observed in the green pellet almost disappears after first cycle, which is consistent with the qualitative observation of the EDS maps shown in Figure 4.5. This is very different from the $NaLiCO_3$-MgO composites, where no significant changes in Mg and Na intensity are seen (ref. Figure 4.4). The exact reason for this difference remains to be identified. Higher viscosity of Na_2CO_3 may be a reason, which leads to a thicker coating of the MgO particles during solidification. Higher sintering temperature could be another reason. The MgO particle could sinter and form a sintering neck structure during sintering process. Such a rigid structure could hold the molten salt and prevent the salt migration within the composite structure during repeated heating and cooling cycles.

4.3.2 CPCMs containing graphite

4.3.2.1 Morphological and microstructural observations
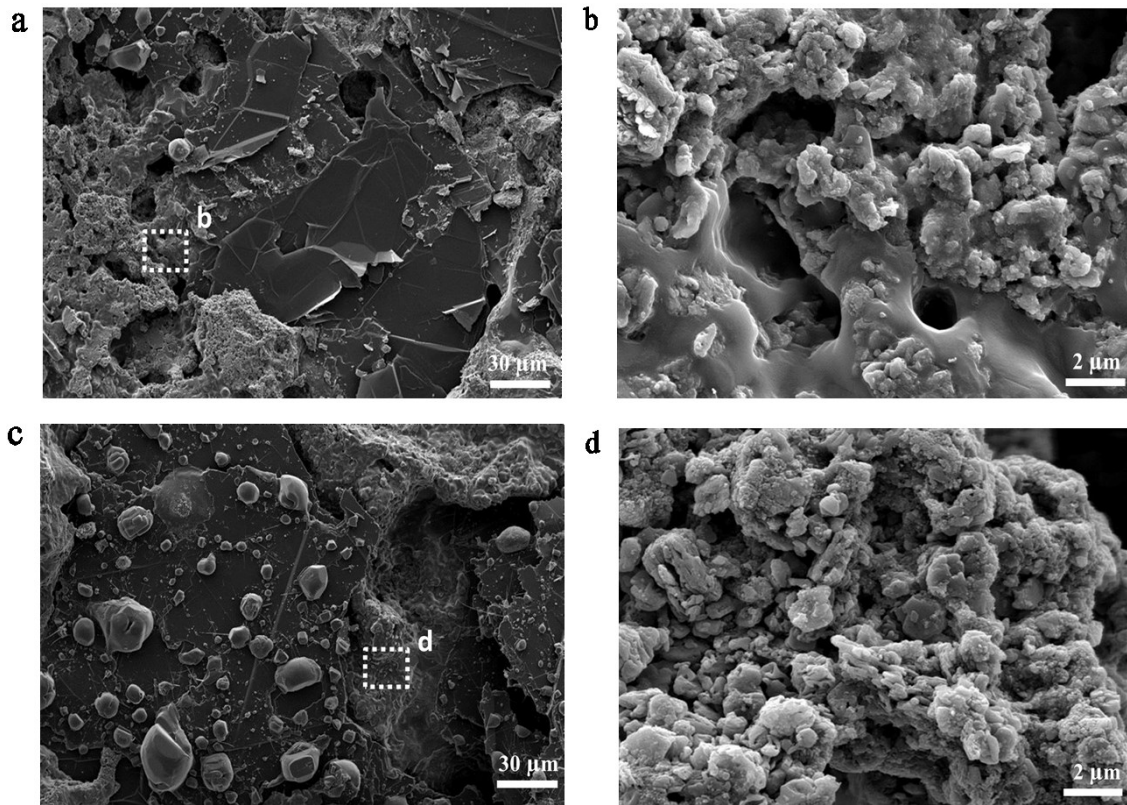
Figure 4.7 SEM images of sintered NaLiCO$_3$-MgO-Graphite composites (a, b) with a mass ratio of 1:1:0.1 and Na$_2$CO$_3$-MgO-Graphite composites (c, d) with a mass ratio of 1:1:0.1. The micrographs on the right hand side are captured from the rectangular areas indicated on the left figures.

Figure 4.7 shows SEM images of two sintered carbonate composites containing graphite. A layered structure is observed in composite and which is due to the addition of graphite flakes and the flat surface of the graphite particles orientate perpendicularly to the compression force. Figure 4.7 also shows a graphite rich area and there micro-gaps between graphite flakes and other ingredients in the composites. This could be attributed to the poor wettability of salt on graphite [9, 10]. An inspection of Figures 4.7 (a) and 4.7 (b) suggests the formation of MSLS, leading to a dense structure, as expected. However, a very different structure is

seen for the Na$_2$CO$_3$-MgO-graphite, as shown in Figure 4.7 (d), where less pores are apparent, giving a more dense structure.

4.3.2.2 Particle distribution and migration during melting-solidification thermal cycles

Figure 4.8 shows the element concentrations along the observation line of the NaLiCO$_3$-MgO-Graphite composite after 0, 1, 10 and 50 heating and cooling cycles. Significant changes can be observed in the concentrations distributions of C (yellow), MgO (blue, represented by Mg) and salt (green, represented by Na). This suggests particle migration and redistribution within the composite structure during repeated heating and cooling processes. Figure 4.9 shows EDS mapping of element C within the NaLiCO$_3$-MgO-Graphite composite after different thermal cycles. The flake shaped graphic particles have an orientation perpendicular to the direction of compression in the green pellet (Figure 4.9a). Thermal cycles appear have led to fragmentation of the particles to give smaller and more homogenously distribution particles (Figure 4.9 b,c,d).

The work by Ge et al indicates a competing mechanism within a composite structure due to different wettabilities of the salt on the CSM and, that on the carbon material [9, 10]. Ceramic materials particularly MgO has a high interfacial energy and hence easily wetted by molten salt, while graphite has a low interfacial energy and hence is less wetted by the salt. This competing mechanism leads the formation of microcavities within the composite structure after thermal cycling. This agrees with the observation of this work; see Figure 4.7. Such microcavities provide a route to absorb volume change during phase change. During heating, salt turns into a viscous liquid, providing a capillary force hold the ceramic particle together while avoiding leakage. In the same time, liquid salt moves within microcavities and

interparticle pores, generating particle migration and creating a shear force that could break graphite particles. The solidification process could also generate significant stress on the graphite, leading to size reduction.
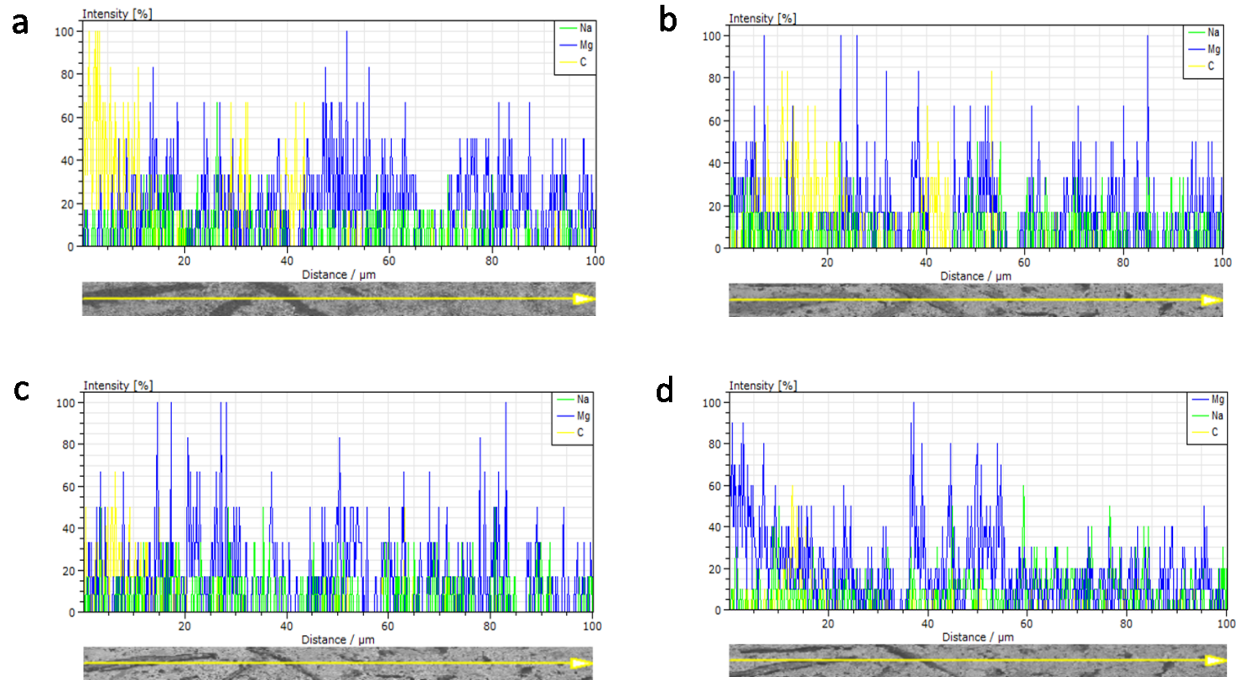
Figure 4.8 EDS mapping of Mg, Na and C along the observation line in the NaLiCO₃-MgO-graphite composite with a mass ratio of 1:1:0.1 experienced different thermal cycles, (a) green sample (non-sintered), (b) after one heating and cooling cycle, (c) after 10 heating and cooling cycles and (d) after 50 heating and cooling cycles; blue, green and yellow colours represent Mg, Na and C, respectively.
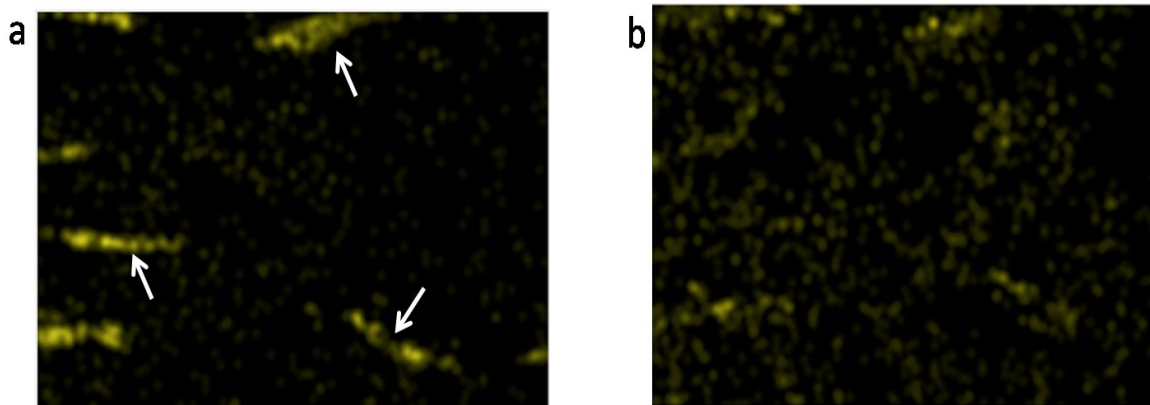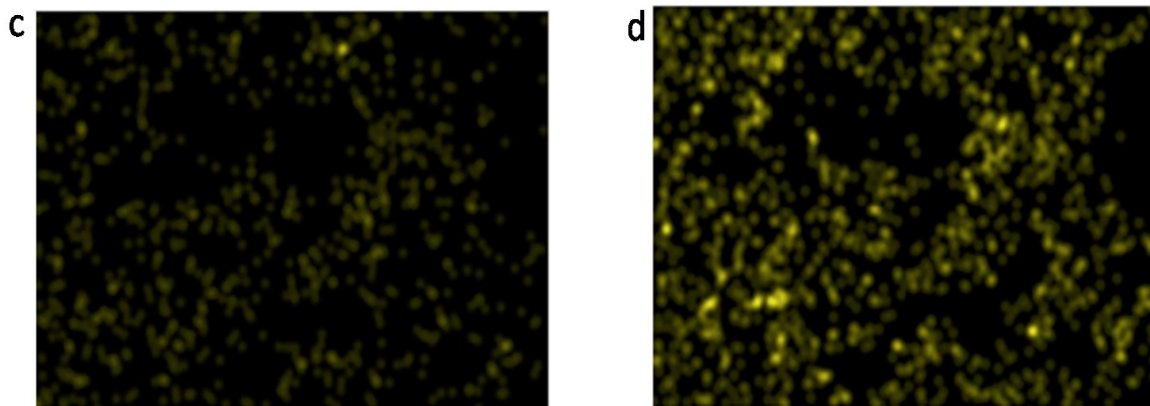
Figure 4.9 EDS mapping images of element C within the NaLiCO$_3$-MgO-graphite composite with a mass ratio of 1:1:0.1 after different thermal cycles, (a) green sample (non-sintered), (b) after one heating and cooling cycle, (c) after 10 heating and cooling cycles and (d) after 50 heating and cooling cycles.

The effect of graphite loading in the composite was also investigated. Figure 4.10 shows EDS maps along the observation line in a NaLiCO$_3$-MgO-Graphite composite with a mass ratio of 1:1:0.6 after 0, 1, 10 and 50 melting-solidification thermal cycles. Difference in the element distribution before and after thermal cycles is apparent though less significant than the composite containing less graphite loading. However, the element distributions after different numbers of thermal cycles are very small, indicating the higher graphite loading may have hindered particle migration. This hindrance may also be associated with wettability of salt on graphite and the flake shape.
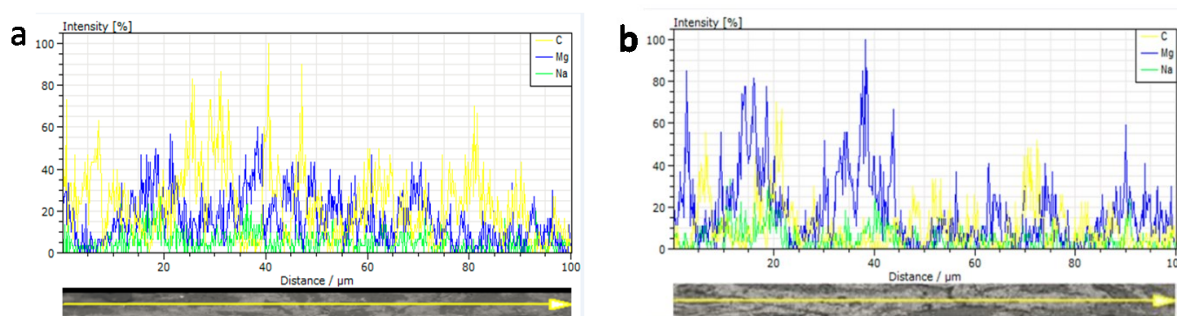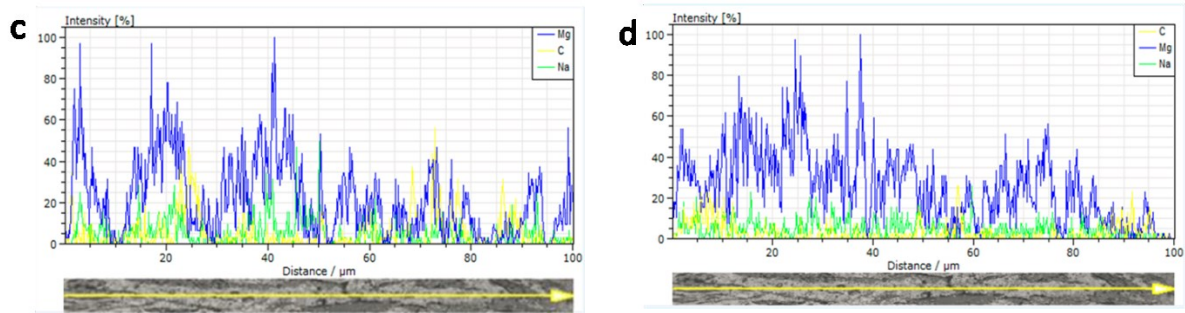
Figure 4.10 Element distributions along the observation line in the NaLiCO$_3$-MgO-graphite composite with a mass ratio of 1:1:0.6 after different thermal cycles, (a) green sample (non-sintered), (b) after one heating and cooling cycle, (c) after 10 heating and cooling cycles and (d) after 50 heating and cooling cycles; blue, green and yellow colours represent Mg, Na and C, respectively.

Figures 4.11 and 4.12 show the C maps in the observation zone of the NaLiCO$_3$-MgO-Graphite composites with mass ratios of 1:1:0.2 and 1:1:0.6 after different heating and cooling cycles, respectively. One can make the following observations: (1) Breakage of graphite particles occurs during thermal cycling and the extent of particle breakage decreases with increasing graphite loading; (2) There are still graphite flakes even after 50 thermal cycles; (3) Particle migration appears to be more difficult with more graphite loading.
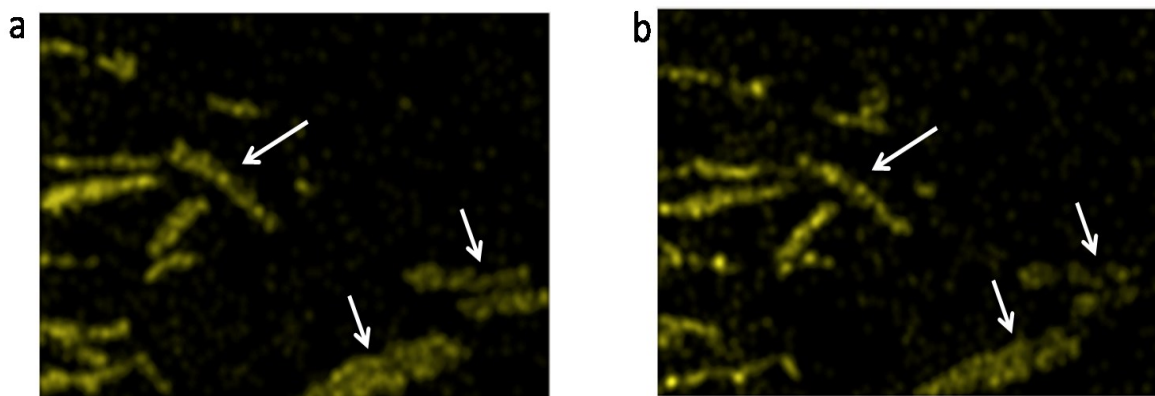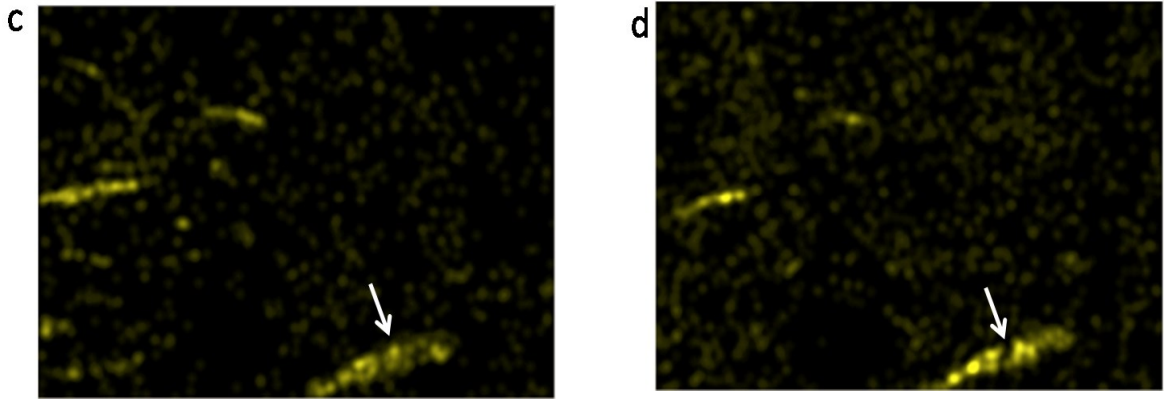
Figure 4.11 EDS element maps of C of NaLiCO$_3$-MgO-graphite composite with a mass ratio of 1:1:0.2 after different thermal cycles, (a) green sample (non-sintered), (b) after one heating and cooling cycle, (c) after 10 heating and cooling cycles and (d) after 50 heating and cooling cycles.
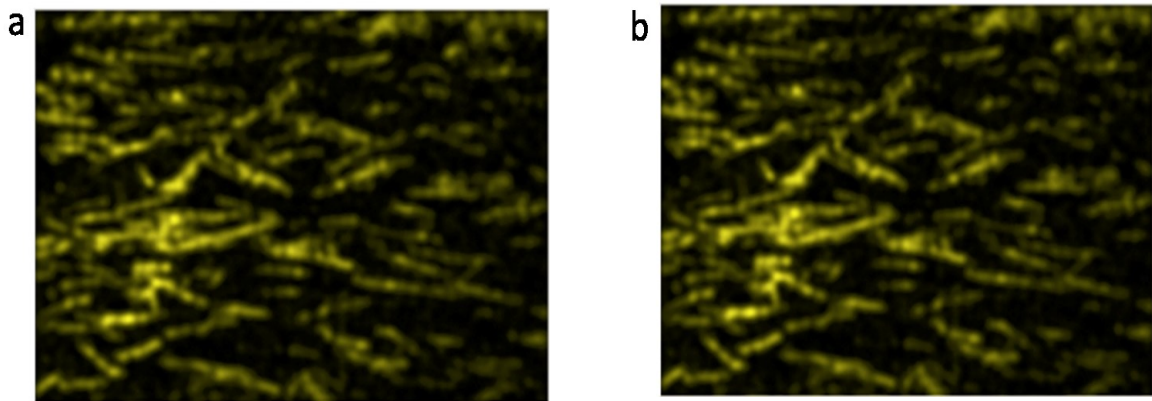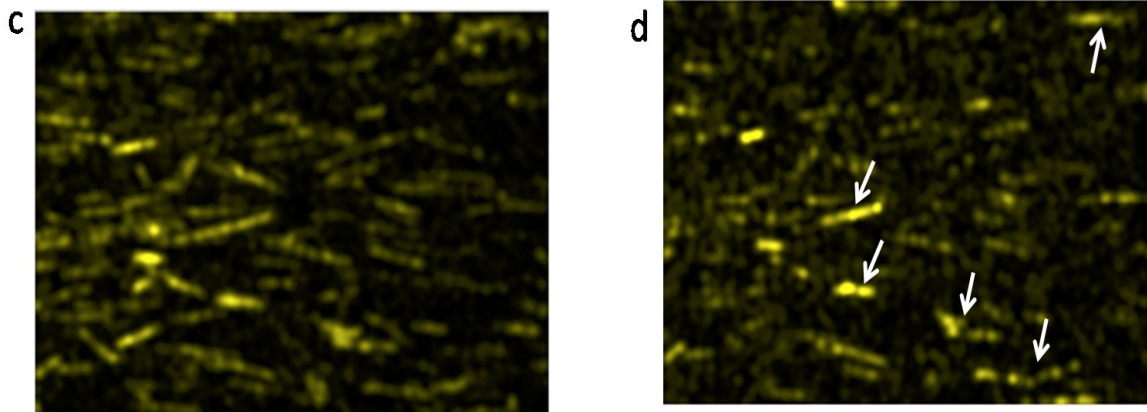
Figure 4.12 EDS element maps of C of NaLiCO₃-MgO-graphite composite with a mass ratio of 1:1:0.6 after different thermal cycles, (a) green sample (non-sintered), (b) after one heating and cooling cycle, (c) after 10 heating and cooling cycles and (d) after 50 heating and cooling cycles.

Shown in Figure 4.13 are concentration distributions of MgO (represented by Mg), salt (represented by Na) and C along the observation line in the Na_2CO_3-MgO-Graphite composite with a mass ratio of 1:1:0.1 under 0, 1, 10 and 50 melting-solidification thermal cycles. Little change could be observed in the concentration distributions after different thermal cycles. This indicates little particle migration and hence redistribution of particles in Na_2CO_3-MgO-Graphite composite during thermal cycles and the use of graphite further hinders the migration.
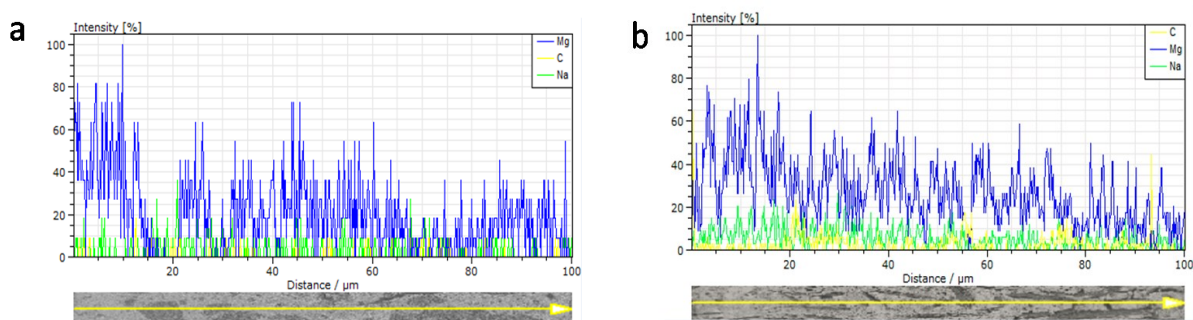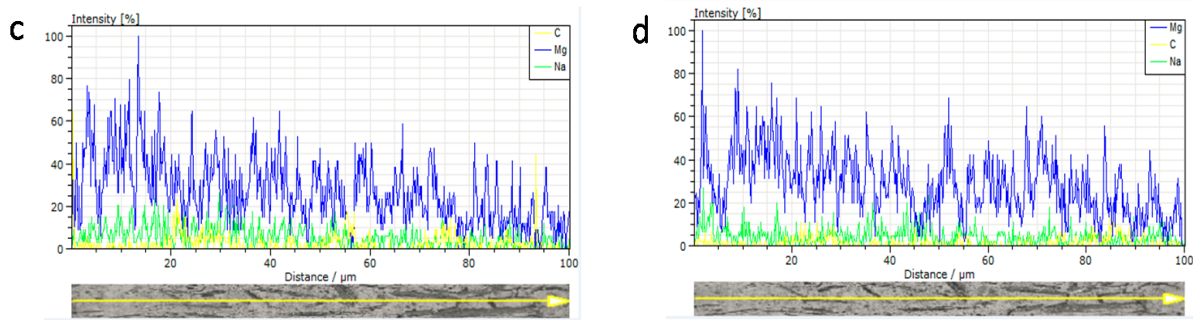
Figure 4.13 Element concentration distributions along the observation line in the Na$_2$CO$_3$-MgO-graphite composite with a mass ratio of 1:1:0.1 after different thermal cycles, (a) green sample (non-sintered), (b) after one heating and cooling cycle, (c) after 10 heating and cooling cycles and (d) after 50 heating and cooling cycles; blue, green and yellow colours represent Mg, Na and C, respectively.

4.3.3 Microstructure development of CPCMs

Based on the experimental observations and analyses presented above, a tentative microstructure development mechanism is proposed for carbonate salt based CPCMs. Figure 4.14 illustrates the mechanism with Figure 4.14 (a) for the eutectic salt based CPCMs and Figure 4.14 (b) for the single carbonate salt based CPCMs.
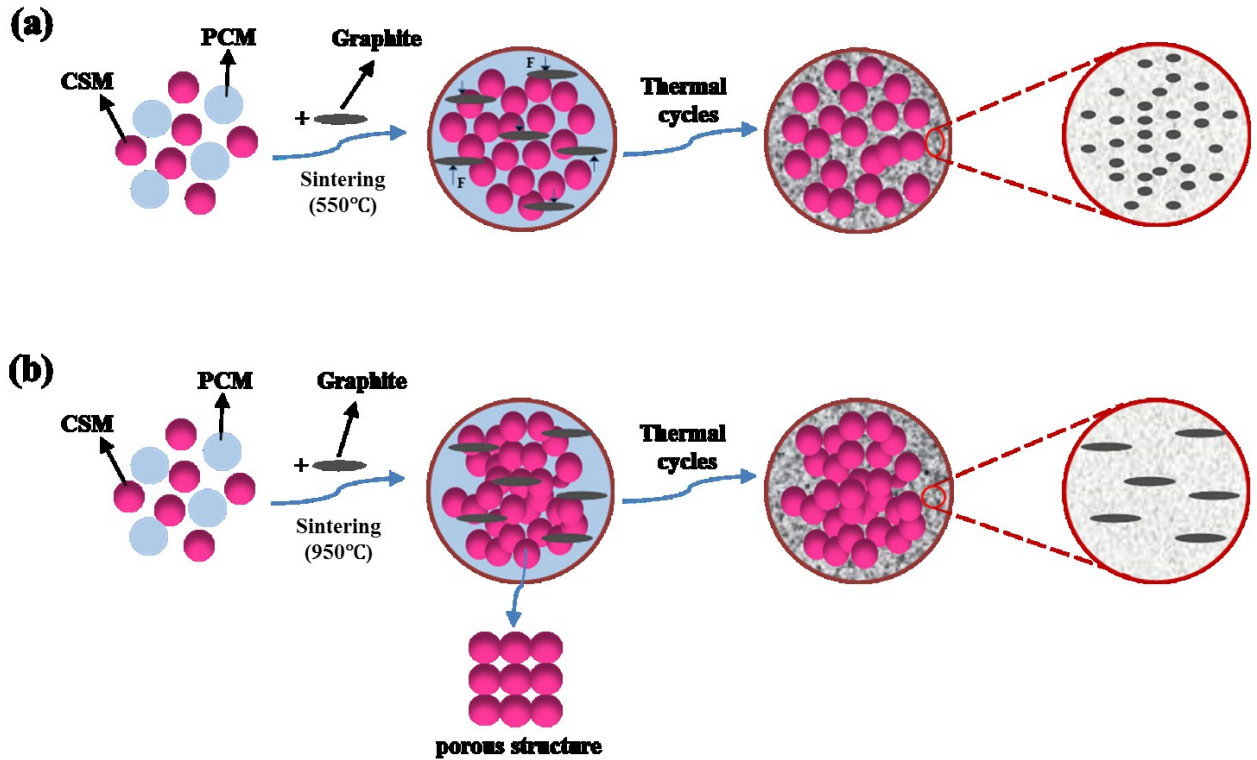
Figure 4.14 Schematic illustrates of microstructure development of CPCMs for (a) eutectic carbonate salt based and (b) single carbonate salt based composites.

First consider the eutectic carbonate salt based CPCMs with a low graphite loading. During the green pellet fabrication process, physical mixing enables good distribution of particles within the composites at the composite module scale whereas the cold compression reduces interparticle voidage. Upon sintering, the solid salt particles form eutectic phase and turns into a viscous liquid when the temperature is above the melting point. The liquid flows into micro-pores under a pressure difference created by volume change and interfacial energy between CSM and the salt. The interfacial energy also pulls the CSM particles together forming liquid bridges among the particles. During such a process, rearrangement and migration of CSM particles occur with the liquid phase salt. This could overcome the swelling caused by graphite particles due to their low surface energy towards the salt, allowing the formation of a dense composite. During repeated heating and cooling cycles, the

salt changes between liquid and solid states. The surface tension (originated from the intermolecular forces) between salt and solid surfaces leads to capillary actions, which could create a significant shearing force (ΔF). Such a shearing action could lead to breakage of graphite flakes. The reciprocating motion of salt causes particle redistribution within the composite, leading to a more homogenous distribution of ingredients. When the graphite loading is high, particles migration inside the composite are restricted due to increased viscosity of liquid salt and low interfacial energy. This gives a reduced extent of graphite breakage and little changes to the concentration distribution over different thermal cycles.

Next consider the single carbonate salt based CPCMs, as shown in Figure 4.14 (b). The fabrication process is similar to that for the eutectic carbonate salt based composites. Upon heating, the solid carbonate salt turns into liquid phase when the prevailing temperature exceeds the melting point. The flow of liquid salt in the interparticle voids leads to rearrangement of CSM. Due to high sintering temperature used in the fabrication process, the CSM could sinter and form a rigid structure upon cooling. Such a rigid microstructure is formed in the first few cycles, which can effectively prevent the salt leakage and, maintain the particle distribution within the composite structure during melting-solidification thermal cycles. It is because of this structure, little rearrangement of CSM particles occurs during subsequent thermal cycles, and little breakage of graphite particles.

Finally, the influence of graphite loading on the microstructure development of CPCMs is analysed further in the following. As discussed before, the low wettability of salt on graphite hinders particle redistribution and swells the structure, the use of a CSM with a high wettability towards salt is needed to maintain the composite structure.
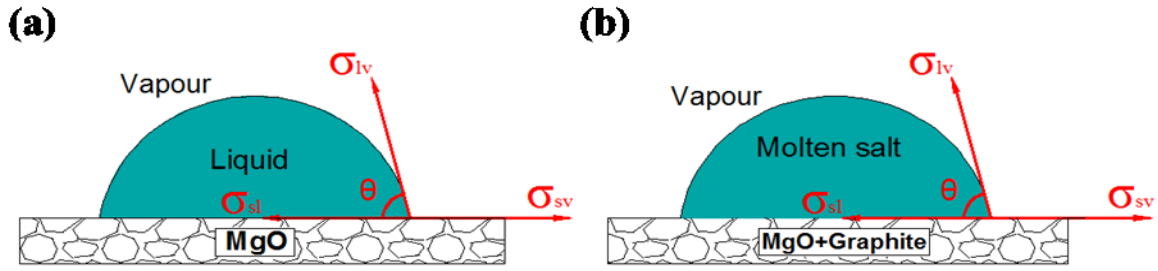
Figure 4.15 A molten salt drop on two different substrates.

According to Young's equation [10, 134], the wettability of the liquid phase on a solid phase is linked to the contact angle and depends on the relationship between the interfacial energies of three phases, solid/vapour, solid/liquid and liquid/vapour. For CPCMs without graphite, the contact angle is determined by the interfacial energy of CSM; see Figure 4.15 (a). The CSM is usually selected to have a relatively high interfacial energy such MgO used in this work, and hence a small contact angle. For CPCMs with graphite, the wettability of salt on the substrate is determined by both the properties of CSM and graphite (Figure 4.15 (b)), and the contact angle can be written as:

$$\cos\theta = \frac{\gamma_{sv(MgO+Graphite)} - \gamma_{sl(MgO+Graphite)/Salt}}{\gamma_{lv(salt)}} \tag{4.1}$$

Figure 4.16 shows measured contact angle data of the two carbonate salts on MgO substrate containing different graphite loadings. As expected, the wettability of carbonate salts on the CSMs decreases with increasing graphite loading. At zero graphite loading, the contact angles for the $NaLiCO_3$ and Na_2CO_3 are approximately 23° and 32°, respectively. They increase to 128° and 133° respectively for the two salts with a graphite loading of 100%. The results also show that the contact angle starts to exceed 90° when the graphite loading is above ~ 60%.

The above observations and analyses confirm that the hindrance of particle migration within the composite structures during melting-solidification thermal cycles is mainly due to the addition of graphite, as illustrated schematically in Figures 4.11 and 4.12. It also explains that the salt leakage could occur within a composite if the graphite is overloaded, as the CSM could not be able to excelled the poor wettability of graphite and retain all the salt [10].
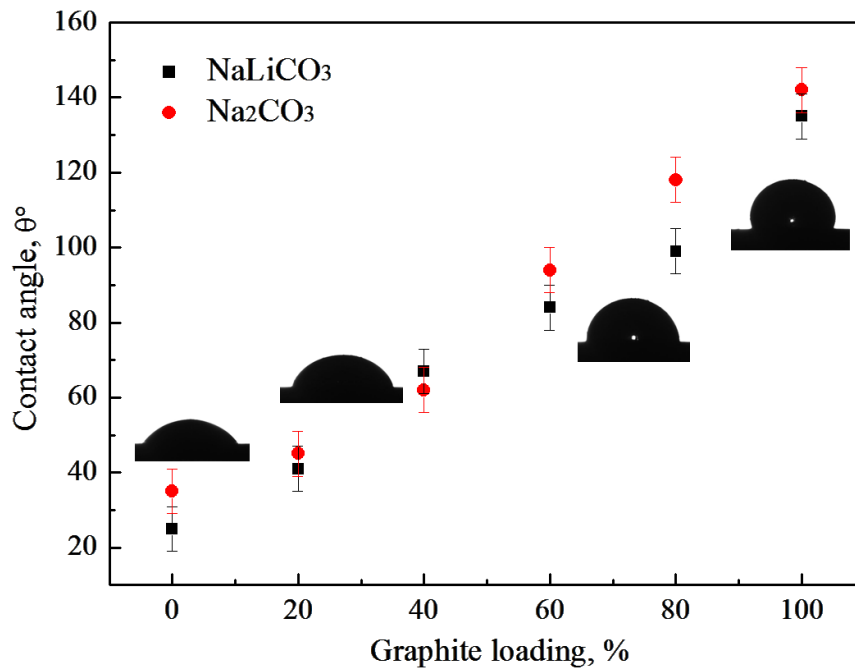
Figure 4.16 Contact angles of the two carbonate salts on MgO and MgO/graphite substrates as a function of graphite loading.

4.4 Conclusions of chapter 4

The microstructure formation mechanisms of CPCMs are studied and presented in this chapter. Two CPCMs, a eutectic carbonate salt and a single carbonate salt based CPCMs, were used as examples in the study using SEM and EDS. Salt motion and particle migration and distribution/redistribution within the composites during melting-solidification thermal

cycles are discussed based on the experimental observations. The effect of TCEM on the microstructure formation was investigated. The following conclusions could be obtained:

(1). Salt motion occurs within the composite structure during repeated heating and cooling cycles. Such motion is likely to be associated with volume change induced by phase change and surface tension due to intermolecular forces. The motion could provide a force to drag the CSM (MgO) to move within interparticle void of the composit microstructure. The motion could form a shear force. Such a force could break graphite flakes. The migration during the melting-solidification processes leads to a more homogenous distribution of both the salt and CSM/TCEM particles and an increase in the density of the microstructure.

(2). The CSM (MgO) particles in the single carbonate salt based composites could sinter and form a porous structure due to the use of a high sintering temperature. This reduces significantly the swelling effect due to the presence of low surface energy graphite and restricts particle motion during melting-solidification thermal cycles.

(3). The addition of graphite flakes in the formulation leads to reduced wettability of the carbonate salt on MgO substrates and limits particle migration within the composites. The extent of the reduction increases with increasing graphite flake loading.

(4). A tentative mechanism is proposed for the microstructure formation of the composite based on the experimental observations and analysis of interfacial energies between PCM, CSM and TCEM.

Chapter 5 Effective Thermal Conductivity of CPCMs

The effective thermal conductivities of carbonate salt based CPCMs have been investigated and reported in this chapter. A theoretical model based on composite microstructures was proposed to predict the effective thermal conductivity of the single carbonate salt based CPCMs. The model uses a unit cell modelled as two MgO spheres in contact with the PCM/TCEM mixture filled in the interparticle void of them. Two models reported in the literature were employed to determine the thermal resistance between the particles and to estimate the sintered neck parameters. A parallel-plate based experimental set up was constructed to measure the effective thermal conductivity of the composites. The modelling results were compared with experimental data and reasonably agreement has been obtained. Various literature models for the effective thermal conductivity were compared with each other and experimental data.

5.1 Introduction

A CPCM consists of a PCM, a TCEM and a CSM. Such a formulation and associated fabricated method have been shown to give an excellent physical and chemical stability and a high thermal conductivity [9-11]. This chapter addresses thermal conductivity of CPCMs, which is essential for the design and optimization of CPCMs based TES components, devices, and systems. As discussed in chapter 4, CPCMs has a microstructure that depends on the formulation and fabrication process, they can be treated as a porous media with the CSM as skeleton for retaining the PCM and TCEM while maintaining structural stability. Prediction of thermal conductivity of such materials is therefore complicated due to many factors involved including microstructures, spatial distribution of different ingredients, and their thermal properties. Numerous theoretical and empirical corrections have been proposed in the literature. These corrections are mostly based on six basic structural models of series, parallel, geometric mean, Maxwell and Zeher-Schlunder [148-155], which cannot be used directly to predict the thermal conductivity of CPCMs. As shown in chapter 4, different fabricated processes also bring complication. This complication can be addressed by considering sintered and non-sintered structure separately [156]. Atabaki and Baliga [157] carried out both experimental and theoretical studies on thermal conductivity of sintered powder-metal plates filled with distilled water and verified the effective thermal conductivity of the sintered materials is higher than that of non-sintered materials. Florez *et al.* [156] studied the effective thermal conductivity of sintered porous media both numerically and experimentally. In their work, thermal circuit analogy was employed to derive an expression for the determination of hemisphere thermal resistance between sintered necks. Alexander [158] investigated the effective thermal conductivity of sintered metal fibres and powders, and proposed a theoretical model based on the experimental data. Sheng *et al.* [159] proposed a junction factor model to predict the effective thermal conductivity of sintered microfibrous materials

made of conductive metal. Hadley [160] considered the effective thermal conductivity of porous media made of unconsolidated and consolidated packed metal particles. A theoretical model for the effective thermal conductivity of sintered porous media made of zinc oxide has also been proposed by Birnboim *et al.* [161], who also studied relationship between the material microstructure and thermal conductivity, with the former including neck growth rate.

The main objective of the work to be presented in this chapter is to investigate the effective thermal conductivity of carbonate salt based CPCMs. A theoretical model is proposed for predicting the thermal conductivity. The model is based unit cells of a matrix media consisting of two MgO spheres (CSM) in close contact with PCM and TCEM mixture fully filled the void between the CSM particles. The point contact model proposed by Zehner-Schunler [153, 154] and the neck growth model proposed by Birnboim *et al* [161], which will be reviewed in Section 5.1.1 and 5.1.2, are employed to account for the sintered and non-sintered structures for the determination of the thermal resistance between the CSM particles. A parallel-plate based experimental set up was designed and constructed to measure the effective thermal conductivity and verify model.

5.1.1 Zehner-Schlunder's model

Zehner-Schlunder's model is the theoretical model that uses a unit cell to predict the effective thermal conductivity of porous media. The unit cell for Zehner-Schlunder's model is shown in Figure 5.1. Zehner and Schlunder [153] assumed that heat conduction in the unit cell follows two parallel paths: one is through the fluid in the outer concentric cylinder and the other is via the inner cylinder which consists of both solid and fluid phases.
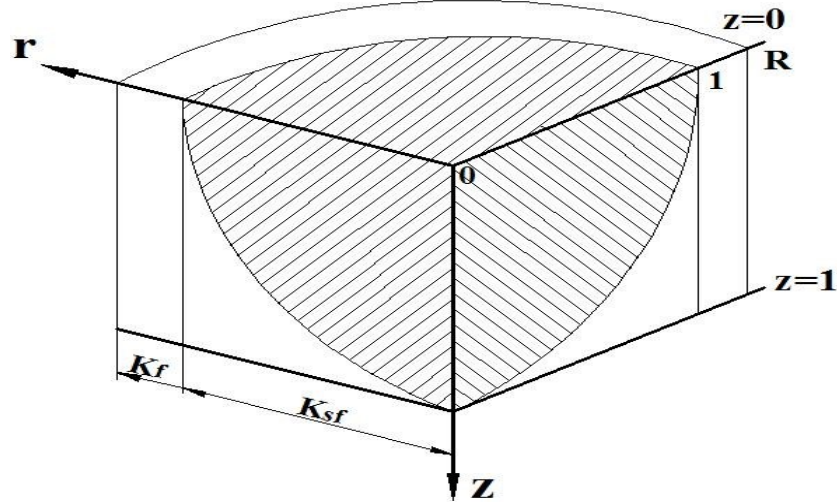
Figure 5.1 Schematic diagram of unit cell of Zehner-Schlunder' model.

Thus, the effective thermal conductivity of unit cell, k_e, can be written as:

$$k_e = \left(1 - \frac{1}{R^2}\right)k_f + \frac{1}{R^2}k_{sf} \qquad (5.1)$$

where k_{sf} is the equivalent thermal conductivity of the inner cylinder consisting of both fluid and solid phases, k_f is the thermal conductivity of fluid phase, R is the particle radius. To determine the relationship between the R and the porosity, the authors obtain from mass transfer experiments that the diffusivity ratio of a fluid-saturated bed to that of a pure fluid is related to the porosity by [153]:

$$\psi_e / \psi_f = 1 - \sqrt{(1 - \phi)} \qquad (5.2)$$

where ψ_e is the diffusivity of a fluid-saturated packed bed, and ψ_f is the diffusivity of the fluid phase. Since heat conduction through a packed bed of non-conducting particles surrounded by a conducting gas is analogous to mass diffusion in a bed, the following equation is therefore given:

$$\lim_{k_s/k_f \to 0} k_e/k_f = \psi_e/\psi_f = 1 - \sqrt{(1-\phi)} \qquad (5.3)$$

The thermal resistances of the solid and fluid in the composite layer are assumed in series, and it follows that $k_{sf} = k_s$ as $k_s/k_f \to 0$ and at this limit, Combining Equation (5.1) and (5.3) gives:

$$\frac{1}{R^2} = \sqrt{(1-\phi)} \qquad (5.4)$$

Thus, the effective thermal conductivity of unit cell can be written as,

$$k_e = \left(1 - \sqrt{(1-\phi)}\right)k_f + \sqrt{(1-\phi)}k_{sf} \qquad (5.5)$$

The value of k_{sf} depends on the shape of the solid and fluid interface (see Figure 5.1) which is given by,

$$r^2 + \frac{z^2}{[B-(B-1)z]^2} = 1 \qquad (5.6)$$

where B is the shape factor, note that for $B=0$ the boundary becomes the z-axis with no solid volume, at $B=1$ the solid becomes a sphere, and at $B \to \infty$ the solid occupies the entire inner cylinder. Assuming the thermal resistances of the solid and fluid phases in the inner cylinder are in series with respect to the temperature gradient and thus,

$$\frac{k_{sf}}{k_f} = \frac{2}{1-\lambda B}\left(\frac{(1-\lambda)B}{(1-\lambda B)^2}\ln\frac{1}{\lambda B} - \frac{B+1}{2} - \frac{B-1}{1-\lambda B}\right) \qquad (5.7)$$

where $\lambda = k_f/k_s$. Substituting equation (5.7) into equation (5.5),

$$\frac{k_e}{k_f} = 1 - \sqrt{(1-\phi)} + \frac{2\sqrt{(1-\phi)}}{1-\lambda B}\left(\frac{(1-\lambda)B}{(1-\lambda B)^2}\ln\frac{1}{\lambda B} - \frac{B+1}{2} - \frac{B-1}{1-\lambda B}\right) \qquad (5.8)$$

The shape factor B is determined from a geometric condition which gives,

$$B = C\left(\frac{1-\phi}{\phi}\right)^{m}$$
(5.9)

In the Zehner and Schlunder's model, C is a constant of 1.25 and m of 10/9 [153, 154].

5.1.2 Birnboim et al.'s model

A two-sphere model for the neck growth as a function of temperature during the initial sintering stage has been proposed by Birnboim et al [161]. Figure 5.2 shows the schematic diagram of two-sphere sintered model, the geometrical parameters in the model are the particle radius, R, the neck radius, x, and the radius of curvature of the sintered neck, r.
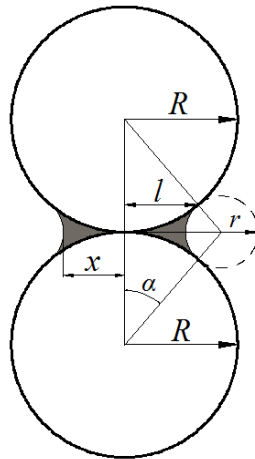
Figure 5.2 Geometric schematic of two-spheres sintered model.

The radius of curvature is given by:

$$r = \frac{x^2}{2R}$$
(5.10)

The volume of material added to the neck per sphere is given by:

$$v = \frac{\pi x^4}{4R}$$
(5.11)

The volume is changing at a rate and can be expressed by:

$$\frac{dv}{dt} = \left(\frac{\pi x^3}{R}\right)\frac{dx}{dt}$$

(5.12)

The volume of matter transported into the neck per unit time is given by:

$$\frac{dv}{dt} = JA\Omega$$

(5.13)

where Ω is the atomic volume, A is the cross sectional area over which surface diffusion occurs, and J is the vacancy flux and given by:

$$J = \frac{D_A \nabla E}{\Omega}$$

(5.14)

where D_A is the vacancy diffusion coefficient and E is the vacancy concentration. The concentration gradient can be approximated by:

$$\nabla E = \frac{\Delta E}{\left(\frac{2\pi r}{4}\right)}$$

(5.15)

where ΔE is the different in vacancy concentration caused by:

$$\Delta E = E - E_0 = \frac{E_0 \gamma_s \Omega}{K_B T r}$$

(5.16)

E_0 is the vacancy concentration near a flat surface, γ_s is the surface energy. T is the temperature and K_B is the Boltzmann constant. Combining above equations can get:

$$\frac{dv}{dt} = \frac{16 D_s \delta_s \gamma_s \Omega}{K_B T(R^2/x^3)}$$

(5.17)

where

$$D_s = D_0 \exp\left(\frac{-Q}{K_B T}\right) \tag{5.18}$$

In Equations 5.17 and 5.18, D_s is the surface diffusion coefficient, D_o is the coefficient of the superficial diffusion, Q is the energy of activation for the superficial diffusion, δ_s is the effective superficial thickness, and T is the sintering temperature in kelvin. Combining Equation (5.12) and (5.17) gives:

$$\int x^6 dx = I \int \frac{\exp\left(\frac{-Q}{K_B T(t)}\right)}{T(t)} dt \tag{5.19}$$

where $I = \dfrac{16 D_s \delta_s \gamma_s \Omega R^3}{\pi K_B}$ \hfill (5.20)

5.2 Experimental setup and thermal conductivity measurements

5.2.1 CPCMs preparation

The two carbonate-salt-based CPCMs, namely, the eutectic carbonate salt and the single carbonate salt based CPCMs, were used in this part of study. Two types of raw MgO materials, heavy and light MgO (Sigma Aldrich Co. LLC, UK), were employed for the CPCMs fabrication. The heavy MgO has a coarse particle size with average diameter of 18 μm and the light MgO has a fine average particle size with average diameter of 4 μm; see Figure 5.3. The eutectic carbonate salt (NaLiCO$_3$) was made from 50 wt% sodium carbonate (Na$_2$CO$_3$, purity >99%, Sigma-Aldrich Co. LLC, UK) and 50 wt% lithium carbonate (Li$_2$CO$_3$, purity >99%, Sigma-Aldrich Co. LLC, UK). The single carbonate molten salt (Na$_2$CO$_3$) was from Sigma-Aldrich Company Ltd, UK, which has a purity >99%. Graphite flakes (Sigma-

Aldrich Company Ltd, UK) were used as the TCEMs. These materials were used as received without further purification.

The detailed fabrication process for the CPCMs has been detailed in chapter 4. Briefly, the process involved three steps. First, preset amounts of PCM, MgO and graphite flakes were mixed in a milling jar of a Planetary Mill Pulverisette (Fritsch, UK) at a speed of 150 rpm for 30 min. The mixture was then put into a mold (diameter of 50 mm) and shaped into a cylindrical pellet by uniaxial compression at a pressure of 30 MPa with a holding time of 3 min. The pellet was sintered in an electrical furnace under N_2 atmosphere at either 550℃ (for the eutectic carbonate salt based CPCMs) or 950℃ (for the single carbonate salt based CPCMs).
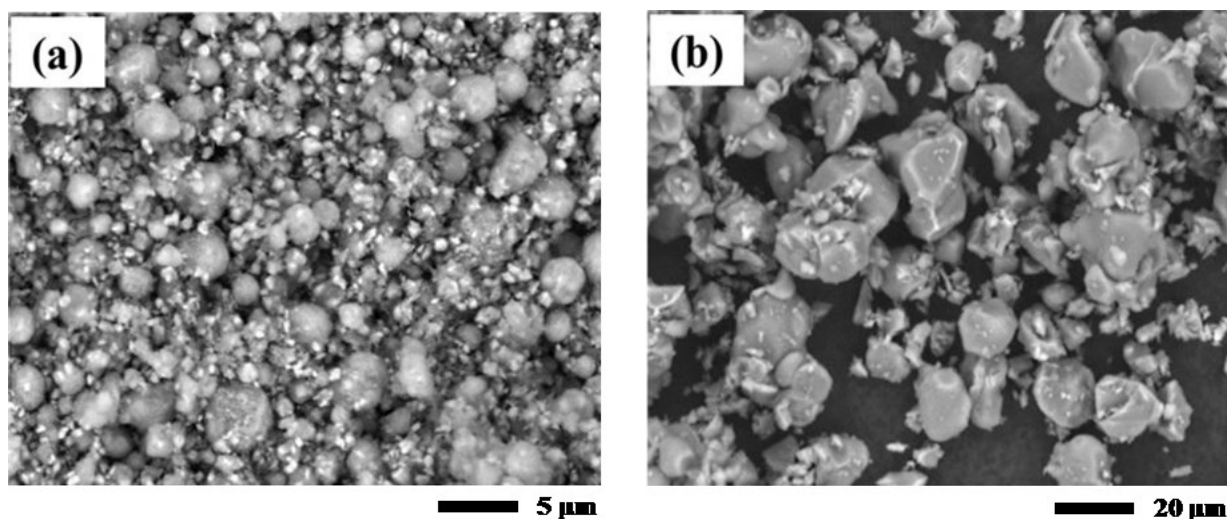
Figure 5.3 SEM images of MgO (a) light MgO and (b) heavy MgO.

5.2.2 Experimental setup

Figure 5.4 shows a schematic diagram of the experimental setup for thermal conductivity measures. The setup consists of an electrical heating element connected to a power supply unit, a test sample, a thermally insulated box, a thermostatic water bath and a data acquisition

system. The electrical heating element has a rated power of 120 W and was purchase from Fisher Scientific Ltd, UK. The power supply unit was obtained from ISE Company, USA, which has an output voltage range of 0-280V. The thermal insulation box was made from ceramic fibre and has size of 300mm×300mm×300mm. The thermostatic water bath was used to provide a constant temperature of 15℃ during the measurements and controlled by a refrigerated circulator (F32-MA, Julabo GmBH, Germany). The data acquisition system consisted of a compact DAQ chassis (cDAQ-9172) and a temperature module (NI-9217) that got from National Instruments Co. Ltd, UK.

In a typical experiment, a test sample was placed between the heating and cooling plates (panels). The heating and cooling panels were in tight contact with the test sample to minimize the thermal contact resistance and to ensure uniform heat conduction. A thermal paste (MX-4 thermal compound, Arctic, UK) was applied on both the contact surfaces in order to reduce the thermal conduct resistance at the interfaces and thermocouples. The power supplier unit and the thermostatic water bath were then switched on followed by the starting of the data logging unit. The power supplier unit provided a preset level of power to the heating element, whereas the water bath carried away an equivalent amount of heat from the heating element. After around 10 mins, an equilibrium state was established when the temperatures at T1-T6 were stabilised as monitored by the data logging unit. These temperature readings together with geometry of the sample and the heating power were used for the estimation of the thermal conductivity; see section 5.2.3 for details. In order to study the accuracy of the measurements, a standard stainless steel (NPL 2109, Thermtest, USA) was used. Each experimental test was repeated at least 3 times to ensure repeatability.
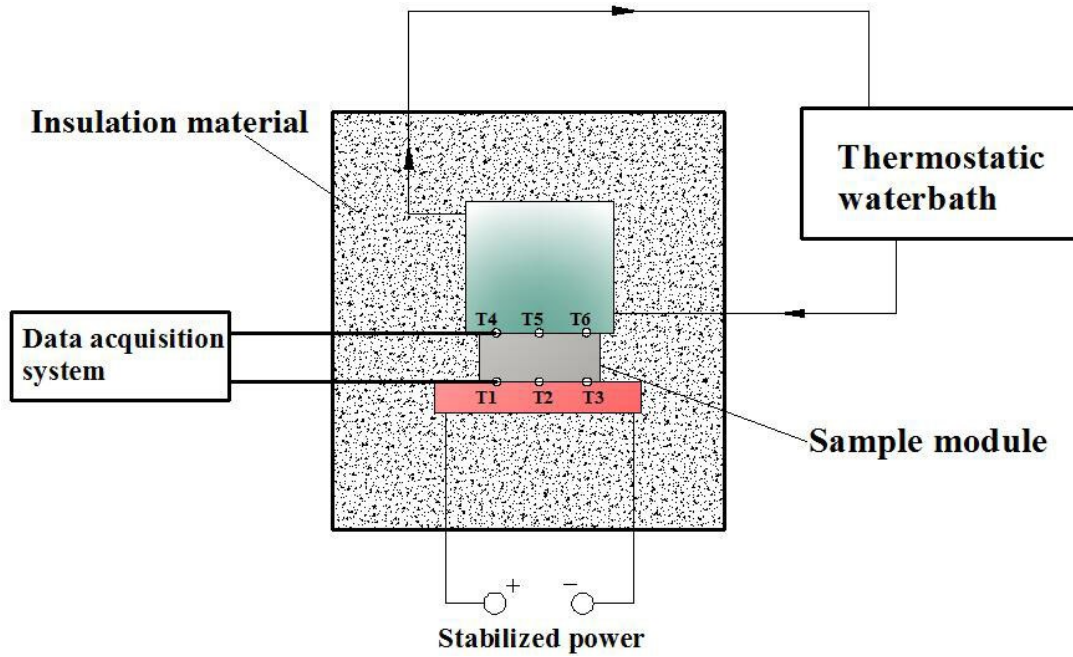
Figure 5.4 Schematic diagram of the test platform for thermal conductivity measurement.

5.2.3 Experimental measurements

As the test samples have a diameter far larger than their thickness (aspect ratio ~5), heat transfer between the hot and cold surfaces can be considered as a one-dimensional heat conduction problem, and the following Fourier's law applies:

$$Q = -\lambda(T) A_c \frac{\Delta T}{\Delta x}$$
(5.21)

where Q is the heat input, $\lambda(T)$ is the thermal conductivity, A_c is the surface area of the sample, and $\Delta T / \Delta x$ is the temperature (T) gradient in the direction (x) vertical to the heating/cooling surfaces. Δx is the thickness of the test sample, $\Delta T = T_{down} - T_{up}$ with T_{down} and T_{up} being respectively the temperature at the lower and upper surfaces of the sample. The upper and lower surface temperatures of CPCMs can be determined experimentally by taking the average of reading of three thermocouples as:

$$T_{down} = \frac{T_1 + T_2 + T_3}{3} \qquad \text{(Hot surface temperature)} \qquad\qquad (5.22)$$

$$T_{up} = \frac{T_4 + T_5 + T_6}{3} \qquad \text{(Cold surface temperature)} \qquad\qquad (5.23)$$

where, T_1-T_6 are the measured temperatures from different thermocouples as shown in Figure 5.4. From Equation (5.21), the thermal conductivity of the CPCM can be estimated as:

$$\lambda(T) = \frac{Q\Delta x}{A_c(T_{down} - T_{up})} \qquad\qquad (5.24)$$

where Q can be estimated from the input power of the electrical heating element; Δx and A_c can be obtained from the sample geometry.

Figure 5.5 shows the measured thermal conductivity of standard stainless steel using the method outlined above. For comparison, reference data [162] are also included. One can see good agreement has been achieved, illustrating the accuracy of the experimental data and reliability of the experimental setup.
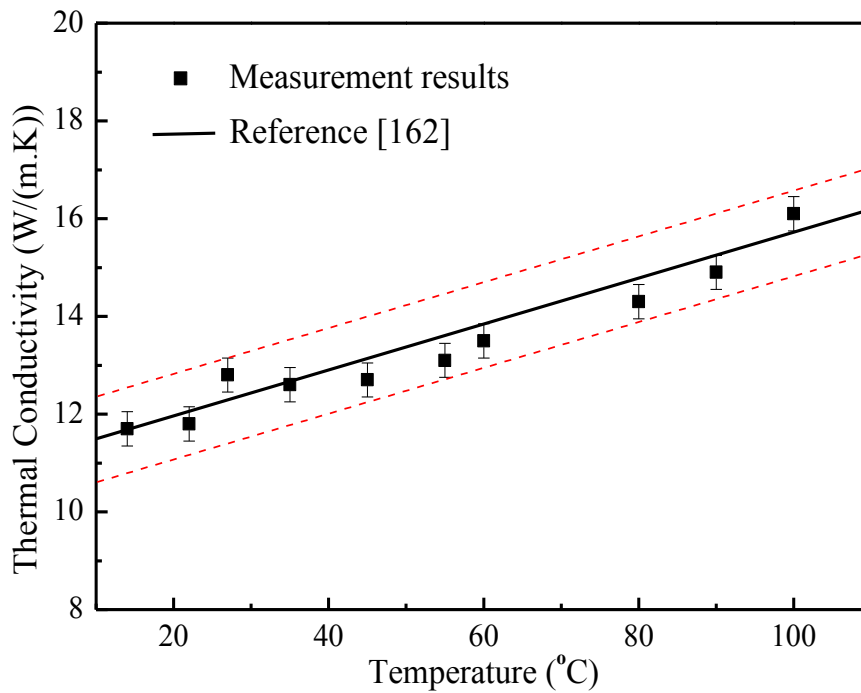
Figure 5.5 Comparison of the measured data with the reference data for stainless steel standard.

5.3 A theoretical model for thermal conductivity of CPCMs

In a CPCM, the CSM serves as the micro-porous supporting material, the PCM and TCEM are distributed in the interparticle voids. For the single carbonate salt based CPCMs, the CSM can sinter and form a rigid porous structure due to the high sintering temperature. Assume that the sintered CSM particles in the single carbonate salt based CPCM are in cubic arrangement, then these particles contact with each other in both vertical and horizontal directions, as shown in Figure 5.6. Consider further that heat is transferred only in one direction (horizontal or vertical).
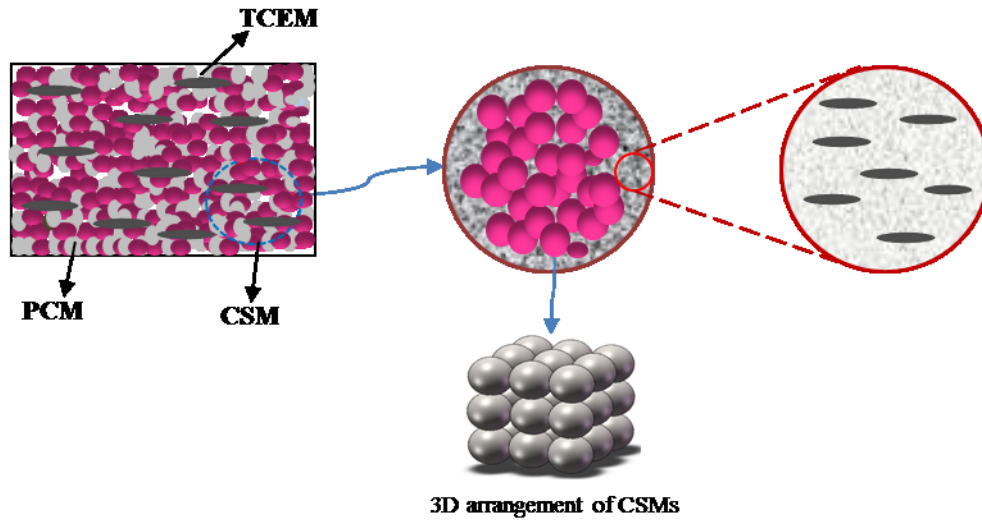
Figure 5.6 A schematic diagram of microstructure of the single salt based CPCM and CSM arrangement.

Under the above assumption, the arrangement of MgO particles can be simplified to a two-particle unit cell as shown in Figure 5.7. This unit consists of two MgO spheres with the same mean diameter, and the two spheres are connected by a sintered neck formed in the sintering process. The PCM and TCEM are treated as a single phase filled in the interparticle voids of the two spheres. As a consequence, the effective thermal conductivity of the single carbonate salt based CPCM can be estimated by using two models reported in the literature: the point contact model proposed by Zehner-Schunler [153, 154] and the neck growth model presented by Birnboim et al [161].
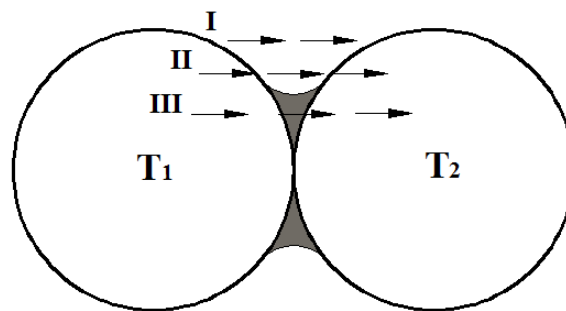
Figure 5.7 Schematic diagram of a two-particle unit cell.
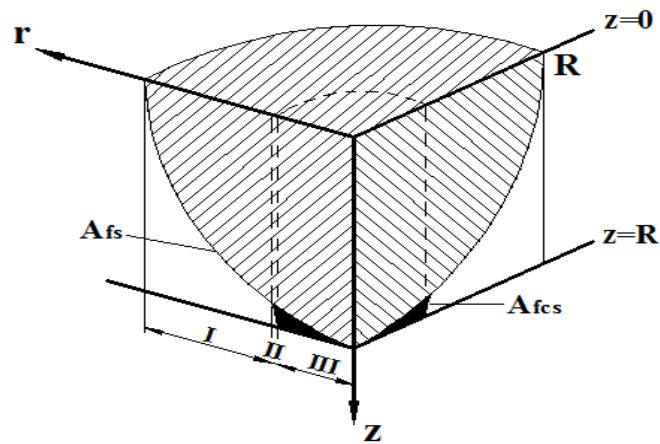
Figure 5.8 Three dimensional representation of a two-particle unit cell.
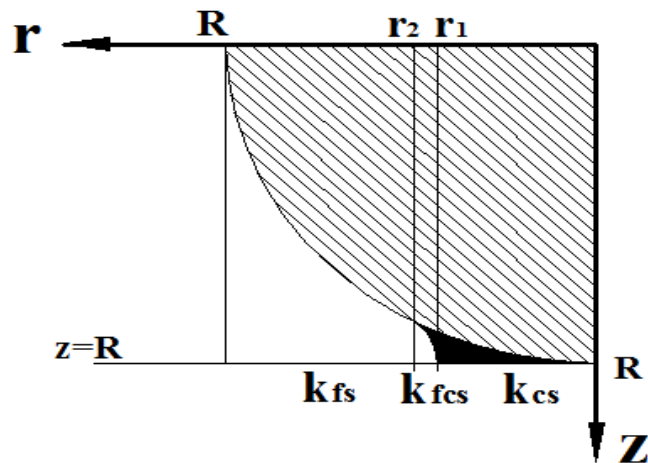
Figure 5.9 A Cross sectional view of the two-particle unit cell.

Figure 5.7-5.9 show schematically a modified two-particle unit cell based on the point contact model (described in Section 5.1.1). Three parallel thermal conduction paths in Regions I, II & III can be identified from these figures. Region I consists of PCM and TCEM mixture, and solid CSM; Region II contains PCM and TCEM mixture, sintered neck and solid CSM; and Region III is made of sintered neck and solid CSM. Accordingly, the effective thermal conductivity of the unit can be calculated from the following expression:

$$k_e = \frac{r_1^2}{R^2} k_{cs} + \frac{R^2 - r_2^2}{R^2} k_{fs} + \frac{r_2^2 - r_1^2}{R^2} k_{fcs} \tag{5.25}$$

where r_1, r_2 and R represent respectively radii at interfaces between Regions III&II, II&I and CSM particles; k_{fs}, k_{fcs} and k_{cs} are respectively equivalent thermal conductivities in Regions I, II and III. These thermal conductivities depend on the shape of the solid and salt interfaces A_{fs} and A_{fcs}. Using the point contact model [153, 154], one has A_{fs} in region I satisfying,

$$r^2 + \frac{z^2}{[(1+\alpha)B - (B-1)z]^2} = R^2 \tag{5.26}$$

where α is the deformed factor.

The equivalent thermal conductivity of k_{fs} can be calculated by the following:

$$\pi(R^2 - r_2^{\,2})k_{fs} = \int_{r_2}^{R} 2\pi r k^* dr \tag{5.27}$$

with k^* given by:

$$\frac{k^*}{k_f} = \frac{1}{1 + (\lambda - 1)z} \tag{5.28}$$

where k_f is the effective thermal conductivity of PCM and TCEM mixture. Equation (5.28) is obtained from the layer-in-series method [154], with an assumption that the thermal resistances of different paths in cylindrical region are in series with respect to the temperature gradient. $\lambda = k_f / k_s$. Combining Equation (5.26) and (5.27) gives:

$$r dr = -\frac{(1+\alpha)B z dz}{[(1+\alpha)B - (B-1)z]^3} \tag{5.29}$$

Integration of Equation (5.29) and application of Equation (5.28) gives:

$$\frac{k_{fs}}{k_f} = A\left\{\frac{1-\lambda}{C^3}\ln\left[\frac{B(1+\alpha)+z(1-B)}{z(1-\lambda)-1}\right] - \frac{1}{C^2\left[B(1+\alpha)+z(1-B)\right]} - \frac{B(1+\alpha)}{2C(B-1)\left[B(1+\alpha)+z(1-B)\right]^2}\right\}\Bigg|_0^{z_2}$$

(5.30)

where $A = \dfrac{2B(1+\alpha)}{(R^2 - r_2^2)}$; $C = 1 - \lambda B + (1-\lambda)\alpha B$; Z_2 is the z-coordinate at $r=r_2$ given by,

$$z_2 = \frac{(1+\alpha)B\sqrt{R^2 - r_2^2}}{1+(B-1)\sqrt{R^2 - r_2^2}}$$

(5.31)

The interface A_{fcs} in Region II is governed by:

$$\left[r - (r_1 + r_m)\right]^2 + \left[z - R\right]^2 = r_m^2$$

(5.32)

and the equivalent thermal conductivity of k_{fcs} is determined by:

$$\pi\left(r_2^{\,2} - r_1^{\,2}\right)k_{fcs} = \int_{r_1}^{r_2} 2\pi r k^{**} dr$$

(5.33)

with

$$\frac{k^{**}}{k_f} = \frac{1}{1+(\lambda-1)z^*}$$

(5.34)

By using Equations (5.32) and (5.33), Equation (5.34) can be integrated to yield:

$$\frac{k_{fcs}}{k_f} = D\left\{\frac{\left[1+(\lambda-1)z\right]}{(\lambda-1)^2} - \frac{1}{(\lambda-1)^2}\ln\left[1+(\lambda-1)z\right]\Bigg|_{Z_2}^{R} - \frac{R}{\lambda-1}\ln\left[1+(\lambda-1)z\right]\Bigg|_{z_2}^{R} + \frac{r_1+r_m}{1+(\lambda-1)z}\Bigg|_{r_1}^{r_2}\right\}$$

(5.35)

where

$$D = \frac{2}{(r_2^{\,2} - r_1^{\,2})} \tag{5.36}$$

Inserting Equations (5.30) and (5.35) into Equation (5.25), one has the model for effective thermal conductivity, k_e.

In order to calculate k_e, a few parameters need to be determined and they are summarised in the following. First, the effective thermal conductivity of PCM-TCEM mixture, this can be determined by Maxwell' model [146]:

$$\frac{k_f}{k_{pcm}} = \frac{k_T + 2k_{pcm} - 2\varepsilon(k_{pcm} - k_T)}{k_T + 2k_{pcm} + \varepsilon(k_{pcm} - k_T)} \tag{5.37}$$

where k_{pcm} is the thermal conductivity of the PCM, k_T is the thermal conductivity of TCEM, ε is the volume fraction of the TCEM in the PCM-TCME mixture.

Second, the sintering neck parameters, r_1, r_2 and r_m, (Figure 5.10) they can be calculated from the sintering curve theory proposed by Birnboim *et al.* [161].
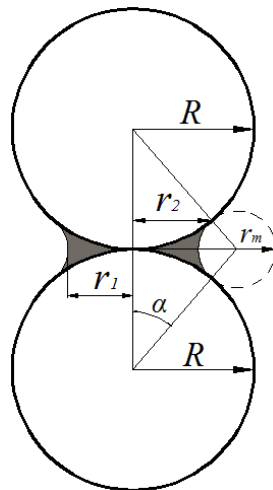
Figure 5.10 Two-particle sintered model [161].

As described in Section 5.1.2, the radius of curvature can be calculated by,

$$r_m = \frac{r_1^2}{2R} \qquad (5.38)$$

r_2 can be then obtained from a geometry analysis, as shown in Figure 5.10,

$$\frac{r_2}{r_1 + r_m} = \frac{R}{R + r_m} \qquad (5.39)$$

5.4 Results and discussion

5.4.1 Sintered neck parameters

In this work, MgO was used as the CSM. The physical properties of MgO are tabulated in Table 5.1 [163-168]. Insertion of these parameters into Equations 5.19 and 5.20, and Equations 5.38 and 5.39 gives the sintered neck parameters.

Table 5.1 Physical properties of MgO [163-168].

Property/parameter	Symbol	Value (units)
Atomic volume (m^3)	Ω	1.87×10^{-29}
Surface energy (J/m^2)	γ_s	0.5
Grain growth Activation Energy (kJ/mol)	Q	199
Mg grain boundary diffusion coefficient multiplied by the grain boundary width	$\delta_s D_s$	$3.4 \times 10^{-9} \exp(-402/RT)$
Boltzmann's constant (J/K)	K_B	1.38×10^{-23}
Melting Point (K)	T_m	3125
Effective superficial thickness (m)	δ_s	4×10^{-10}

Utilisation of those data, one can obtain the sintering neck radius as a function the average particle size of MgO. Figure 5.11 shows the results for a sintering temperature of 950 ℃ and sintering time of 400 mins (see the insert of Figure 5.11). One can observe that the sintering neck radius increases with an increase in MgO particle size and the increasing trend tends to level off for particles larger than ~ 1000 μm. The neck size is sensitive to the MgO particle size particularly when MgO particle is less than ~ 100 μm. This is partially because of higher surface energy of smaller par ticles, leading to easier contact formation and neck growth [165, 167]. Other reasons for the particles size effect are associated with heat and mass transfer during sintering-the larger the particle size, the lower the heat and mass transfer rates due to larger transport distance [165-168].
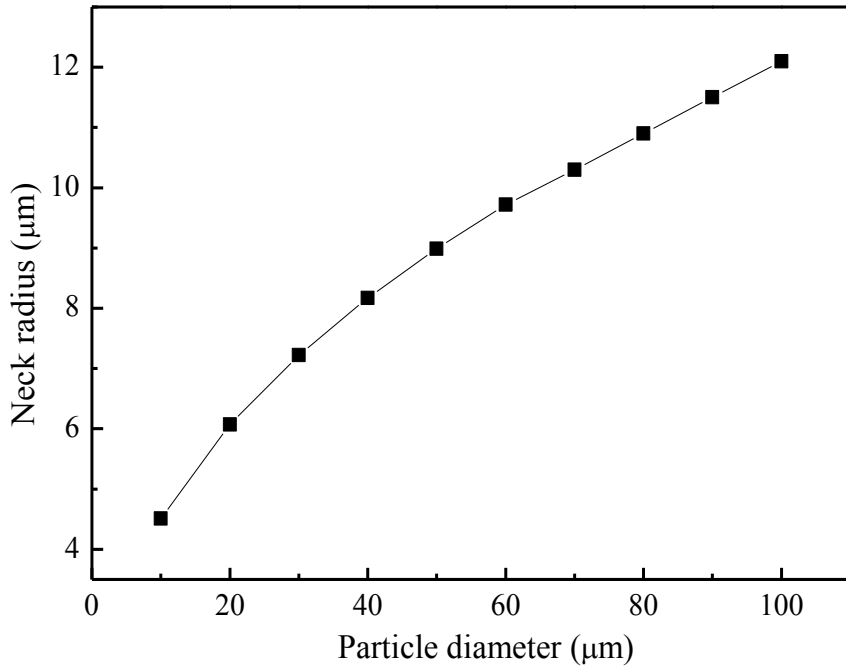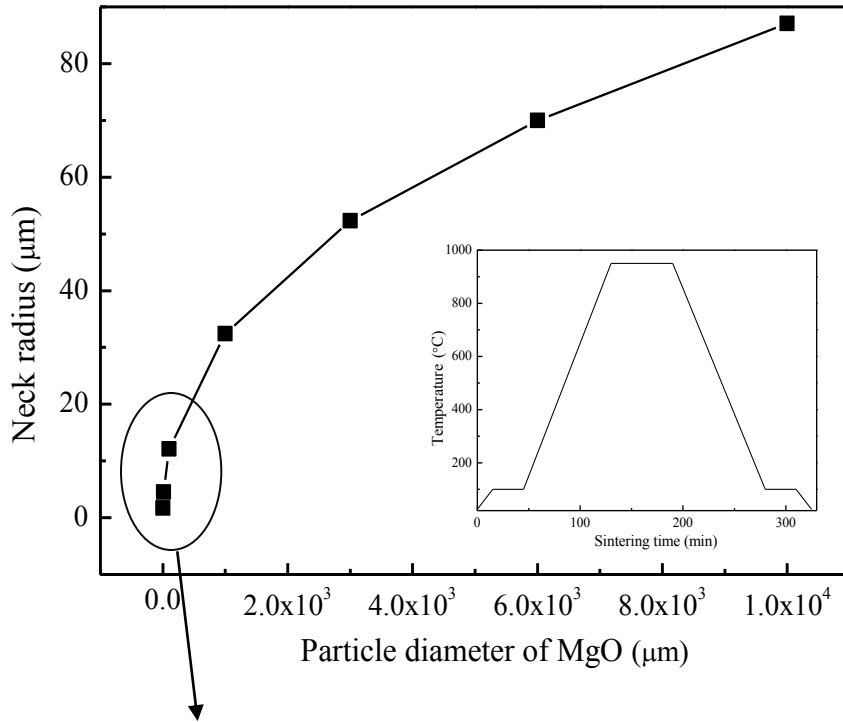
Figure 5.11 Radius of sintering neck as a function of particle diameter of MgO; insert is the sintering temperature program.

5.4.2 Comparison between effective thermal conductivity model and experimental data

Given α and B, Equation (5.25) can be solved for the effective thermal conductivities. Taking B as 1 for MgO particles (approximately spherical, as shown in Figure 5.3), the effective thermal conductivity as a function of particle size is shown in Figure 5.12 for different particle shape deformation factor α. In the figure, α=0 represents cases with no particle shape deformation, whereas α=1 denotes large particle shape deformation. One can see that the effective thermal conductivity decreases with increasing particle deformation factor for a given particle size, and the shape deformation factor impacts become significant with MgO particle size increased. The effect of particle size on the thermal conductivity is only significant for particles smaller than ~ 30 μm, beyond which the increasing trend levels off.
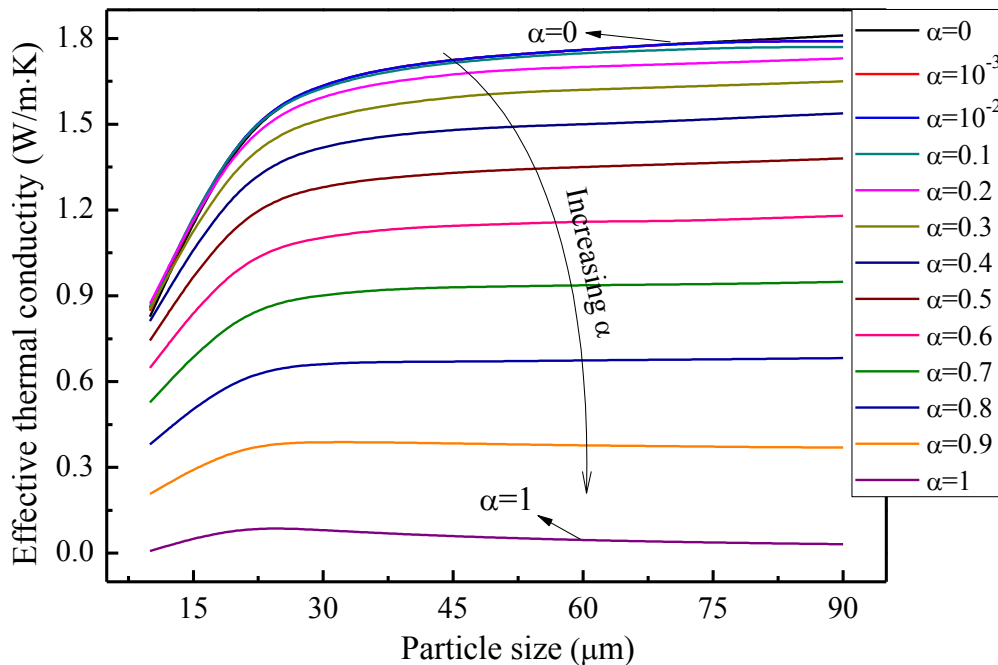
Figure 5.12 Variation of the effective thermal conductivity as a function of particle size and shape deformed factor.

Figure 5.13 compare the calculated effective thermal conductivity using the model and the experimental data as a function of MgO size for the single carbonate salt based CPCMs without the addition of graphite. It is seen that the theoretical results are in excellent agreement with the experimental data when the shape deformed factor is ~ 0.6, with the effective thermal conductivities increasing with increasing particle size. The deviations between calculated results and experimental data are 7.4% for case 1 (light MgO) and -9.8% for case 2 (heavy MgO). The error bars indicate the uncertainty measurement scope. For both cases, the deviations between the model results and experimental data are within the uncertainty range of measurements. Except for possible the measurement errors, the difference may be due to the assumption of the shape factor of B=1 and B can be slightly away from 1, particularly for heavy MgO as shown in Figure 5.3. Another possible reason is the existence of non-uniform particle size as also shown in Figure 5.3.
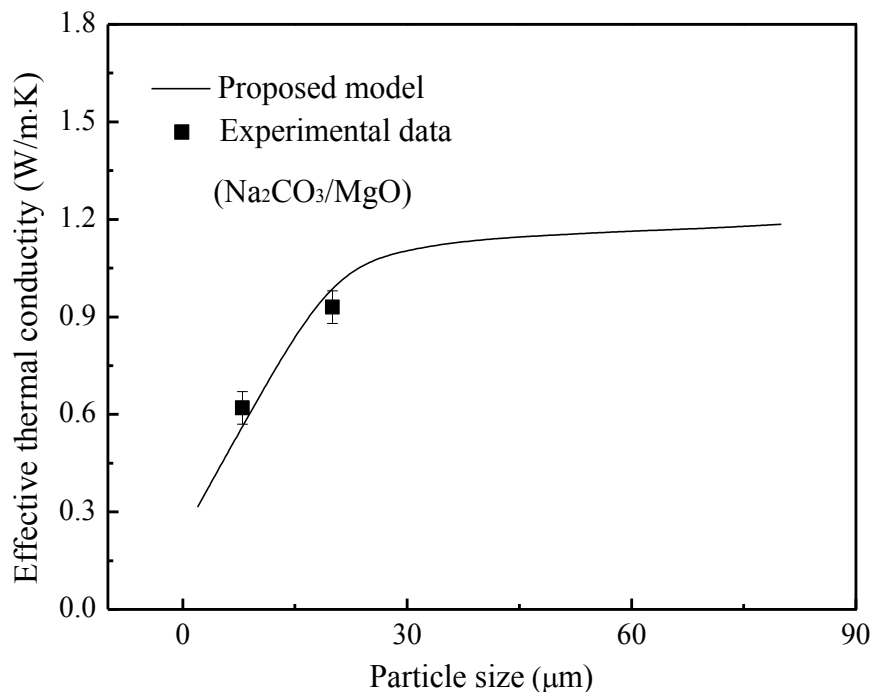
Figure 5.13 Comparison between calculated results and experimental data for CPCMs without graphite.

Figure 5.14 compares the calculated effective thermal conductivities and the experimental data for single carbonate salt based CPCMs with graphite. Good agreement has been obtained with deviations of -12.1% for case 1 (light MgO) and -15.2% for case 2 (heavy MgO), and the calculated results are within the experimental error bars for both the cases. A comparison between Figures 5.13 and 5.14 shows that the addition of graphite increases the thermal conductivity significantly. The addition of graphite also increases the deviation between experiments and calculations. This can be explained by the effective thermal conductivity calculation method for the PCM and TCEM mixture used. As mentioned earlier, the effective thermal conductivity of PCM and TCEM mixture is calculated by the Maxwell model. This model is for spherical non-interacting particles. Graphite particles are flake shaped, which should give, in theory, a lower effective thermal conductivity. Moreover, the anisotropy effect of graphite flake is not considered in the Maxwell model, which also could bring the deviation. This is indeed demonstrated in Figure 5.14 where negative deviations are obtained. The deviations could also be due to the MgO particle shape and non-uniform particle sizes as described above and shown in Figure 5.3. Another possible reason is that, the bigger the MgO particles, the more difficult the particles to be sintered [132, 133].
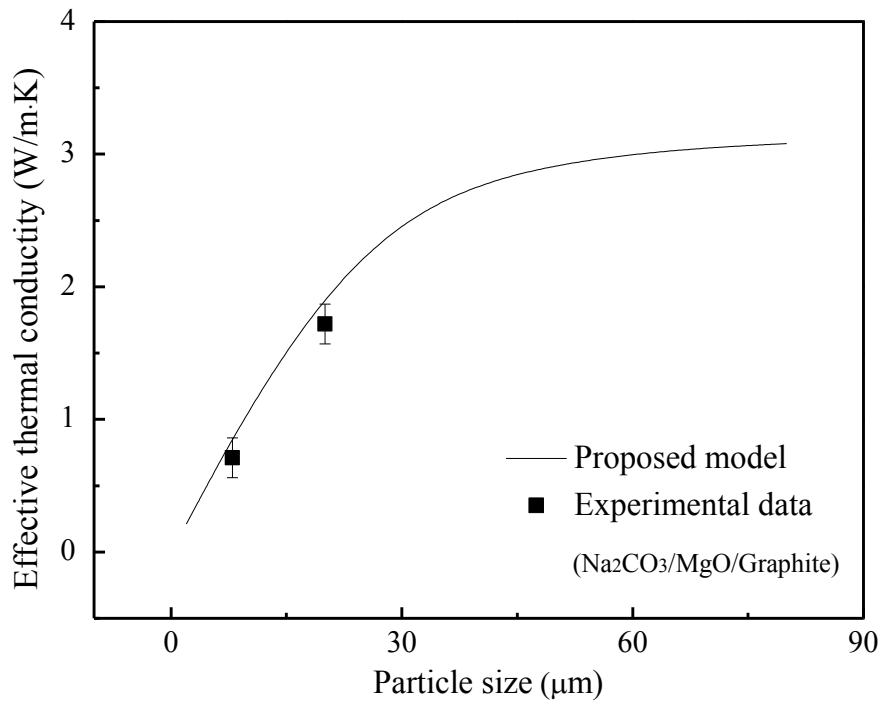
Figure 5.14 Comparison between calculated results and experimental data for CPCMs with graphite (5wt% graphite).

5.4.3 Comparison between the model proposed in this study and the literature models

Figures 5.15 and 5.16 show a comparison of the experimental results for the effective thermal conductivity of the eutectic carbonate salt based CPCMs with and without graphite, with those calculated results using the literature models. Note the porosity needed by the literature models has not been measured. The following equation is therefore employed to transfer the input parameter of porosity to the volume ratio of PCM or PCM-TCEM mixture that used in the experiments and the model proposed in this study:

$$\eta = \varphi_{PCM} = v_{PCM} / v_{composite} = \frac{m_{PCM} / \rho_{PCM}}{m_{PCM} / \rho_{PCM} + m_{CSM} / \rho_{CSM} + m_{TCEM} / \rho_{TCEM} + v_{air}} \quad \text{(without graphite)} \quad (5.40)$$

$$\eta = v_{PCM+TCEM} / v_{composite} = \frac{m_{PCM}/\rho_{PCM} + m_{TCEM}/\rho_{TCEM}}{m_{PCM}/\rho_{PCM} + m_{CSM}/\rho_{CSM} + m_{TCEM}/\rho_{TCEM} + v_{air}} \quad \text{(with graphite)} \qquad (5.41)$$

where v_{PCM}, $v_{composite}$ and v_{air} are the volume of PCM, composite and air, respectively; m_{PCM}, m_{CSM}, and m_{TCEM} denote respectively the mass of PCM, CSM and TCEM; ρ_{PCM}, ρ_{CSM}, and ρ_{TCEM} represent the density of PCM, CSM and TCEM, respectively.

The experimental data for eutectic carbonate salt based CPCMs without graphite seems to agree fairly well with the Ratciffr's and Maxwell's models, and the average deviation are -3.8% and 7.9% for both cases, respectively. The Zehner-Schlunder's model shows a fairly level of deviation from the experimental data particularly for the small MgO size case. In contrast, the Alexander's model takes into account the sintering behaviour of particles and does not show good comparison with the experimental data and other models. The rest models deviate significantly from experimental data particularly the parallel and series models which are too ideal to be applicable in these cases.
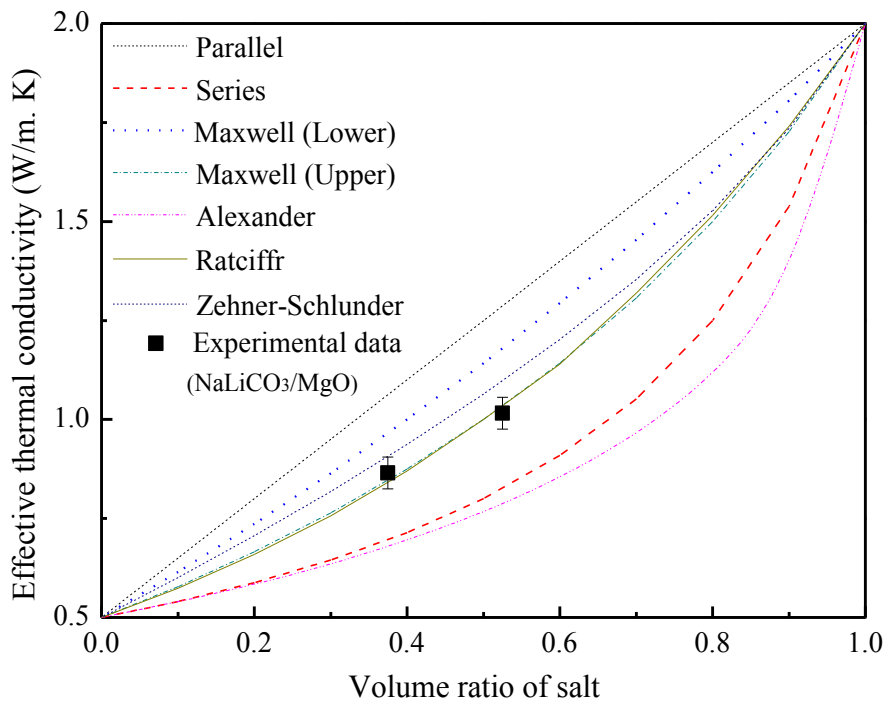
Figure 5.15 Comparison between experimental data and literature models for the eutectic carbonate salt based CPCMs without graphite.

The measured effective thermal conductivities for the eutectic carbonate salt based CPCMs with graphite are compared with the literature models in Figure 5.16. Zehner-Schlunder' and Ratciffr's models are seen to give a closer agreement than other models, and the average deviations are respectively 10.1% and 8.8% for both cases. The Maxwell' model, on the other hand, shows considerable deviations in this case, which is different from the case without graphite where the agreement is good. Such a difference is, as discussed above, likely to be associated with the shape of graphite flake which is not accounted by the Maxwell theory.
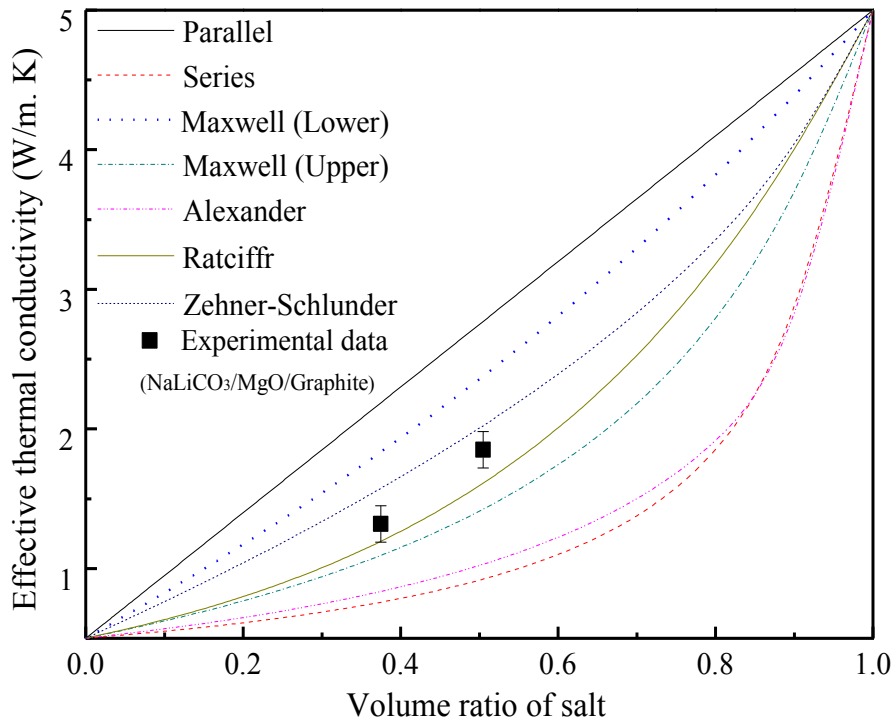
Figure 5.16 Comparison between experimental data and literature models for the eutectic carbonate salt based CPCMs with graphite (5wt% graphite).

Figures 5.17 and 5.18 compare the measured effective thermal conductivity of single carbonate salt based CPCMs with the model results. One can see that the effective thermal conductivity is very sensitive to the MgO size in both cases of CPCMs with and without graphite. The Alexander model seems to agree with the experimental data for the CPCMs

with small sized MgO. This model, however, differs significantly from the measured data of the CPCMs with the heavy (large sized) MgO, whereas the Ratciffr's model gives better agreement. Also shown in Figure 5.17 and 5.18 are the calculated results using the model development in this work. Very good agreement has been achieved for both cases.
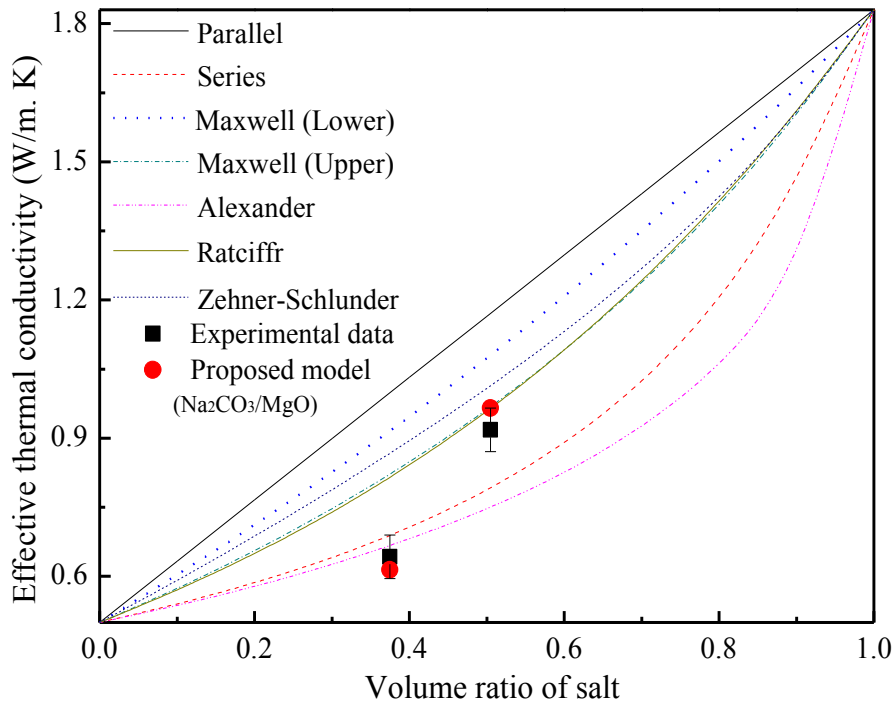
Figure 5.17 Comparison between experimental data and literature models for the single carbonate salt based composite without graphite.
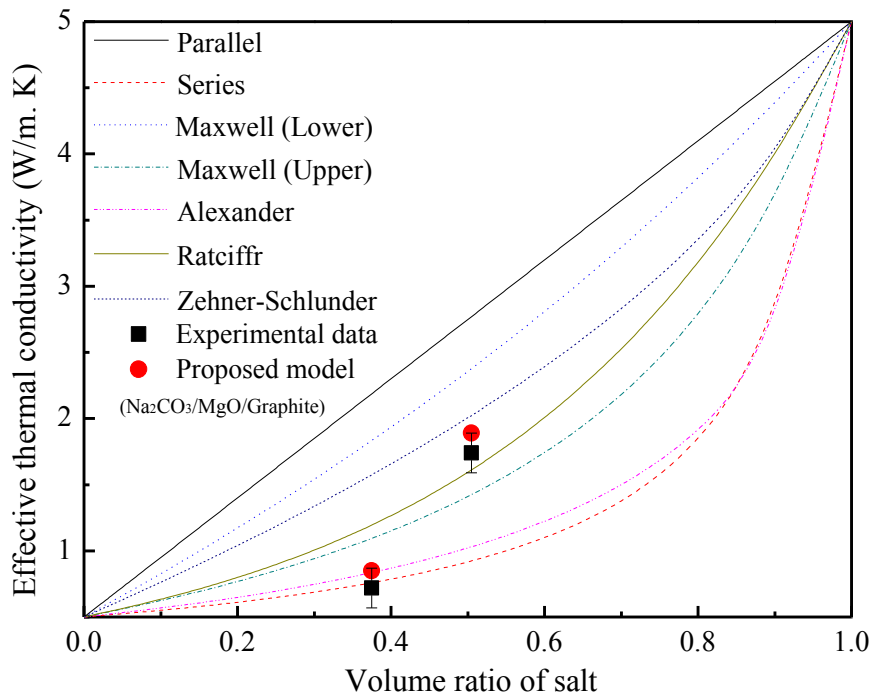
Figure 5.18 Comparison between experimental data and literature models for the single carbonate salt based composite with graphite (5wt% graphite)

Table 5.2 summarises the deviations between the experimental data and literature models. The results of the model of this work are also shown in the table (Last row). One can see overall the model derived in this study gives the best agreement with experiments.

Table 5.2 Differences between literature model results and experimental data.

Differences %	NaLiCO$_3$ /MgO		NaLiCO$_3$ /MgO/C		Na$_2$CO$_3$ /MgO		Na$_2$CO$_3$ /MgO/C	
	Case1	Case2	Case1	Case2	Case1	Case2	Case1	Case2
Parallel	-16	-15.6	-32.4	-22.5	-41.3	-23.8	-58.6	-19.3
Series	23.7	31.75	82.7	134.3	-14.1	27.1	-6.6	137.5
Maxwell (lower)	-7.6	-7.7	-18.7	-19.4	-36.1	-19.1	-50.8	-7.9
Maxwell (upper)	4.4	5.4	23.6	42.1	-28.5	-11.7	-16.8	49.3
Alexander	25.8	37.7	68.2	110.1	-5.1	28.2	-5.1	112.8
Ratciffr	5.4	5.4	10.3	24.7	-27.9	-12.1	-24.3	29.6
Zehner-Schlunder	-4.3	-6.6	-15.3	-9.5	-32.3	-13.9	-42.5	-8.2
Proposed model	25.4	29.2	21.1	31.2	7.4	-9.8	-12.1	-15.2

5.5 Conclusions of chapter 5

This chapter concerns the effective thermal conductivities of carbonate salt based CPCMs. A theoretical model is derived for calculating the effective thermal conductivity of the CPCMs. The model uses a unit cell modelled two MgO spheres in contact with a PCM/TCEM mixture filled in the interparticle voids. Two models reported in the literature are employed to determine the thermal resistance between spheres and to estimate the sintered neck parameters. A parallel-plate based experimental set up was designed and constructed to

measure the effective thermal conductivities of the composites and to verify the theoretical model. The following conclusions are obtained:

(1). The theoretical model agrees well with experimental data.

(2). The Zehner-Schlunder and Raticffr models appears to agree with experimental data of eutectic carbonate salt based CPCMs.

(3). The Alexander model seems to agree with experimental data for the single carbonate salt based CPCMs made with small sized light MgO, whereas the Ratciffr model shows a better agreement with the measurements for the CPCMs made from the larger sized heavy MgO particles.

(4). The deviations of the theoretical model from experiments are likely due to particle shape and non-uniform distribution of MgO particles.

Chapter 6 Linking material properties to device performance

This chapter reports the results of both experimental and numerical studies on the heat transfer behaviour of CPCMs based TES at component and device levels. The aim is to establish a relationship between the device level performance and materials properties for CPCM based TES. Two types of components, a single tube and a concentric tube component, were designed and investigated. A mathematical model was formulated for studing the transient heat transfer behaviour of CPCM modules and TES components. The modelling results were first compared with experiments to demonstrate suitability of the model. Extensive modelling studies were then carried out under different conditions. Various factors such as CPCM material's properties, CPCM module size, surface roughness of the module and flow conditions of charging and discharging processes were examined. CPCM TES devices using the CPCM components were then investigated with a specific focus on the effect of the component arrangements.

6.1 Numerical Modelling

6.1.1 Physical models

The aim of the work to be presented in this chapter is to establish a linkage between materials properties at material module level and device level performance. Figure 6.1 shows the physical configurations for the study, which is multiscale in nature. Two CPCM module configurations are designed and fabricated as shown in Figure 6.2. The eutectic carbonate salt (LiNaCO$_3$), MgO and graphite are used as PCM, CSM and TCEM, respectively. The eutectic carbonate salt is made of lithium carbonate (Li$_2$CO$_3$) and sodium carbonate (Na$_2$CO$_3$) with the mass ratio of 1:1. The thermophyscial properties of the matetials are measured by different methods including Dilatometer for density (DIL 806), Laser Flash Analysis for thermal conductivity (LFA 427), and differential scanning calorimetry for heat capacity, phase change temperature and enthalpy (DSC, QMS 403D). Table 6.1 show the results. Two CPCM based TES components are designed for the use of the material modules as illustrated in Figure 6.2. One of the components uses solid CPCM modules, and these modules are disc shaped, stacked in a cylindrical tube, as shown in Figure 6.2 (a). The tube has a length (L_s) of 500 mm, an outer diameter (D_s) of 58 mm and a wall thickness of 3 mm. The diameter and thickness of the solid CPCM modules, d_s and h_s are 50 mm and 10 mm, respectively. The other component uses concentric disc, which are stacked in a concentric tube as shown in Figure 6.2 (b). The concentric tube has the same length and wall thickness as that for the single tube based component. The outer and inner diameters of the concentric tube are 60 mm (D_e) and 12.2 mm (D_i), respectively. To make meaningful comparison between the two components, the CPCM modules are made to have inner and outer diameters of 14.2 mm and 52 mm, respectively. This gives the same CPCM mass as the solid CPCM modules. One notices that there are small gaps between the material modules and the tube walls. The gaps

are filled with graphite powers for two reasons. One is for lubrication during assembly, and the other is to allow for fabrication errors for both the tubes and material modules. The TES device is designed to have configuration as shown in Figure 6.1 (c), which has an outer shell containing an assembly of TES components. A HTF flows across the TES components (for the tubular TES components) or through the inner tube (for the concentric tubular components) to realise charge and discharge processes.
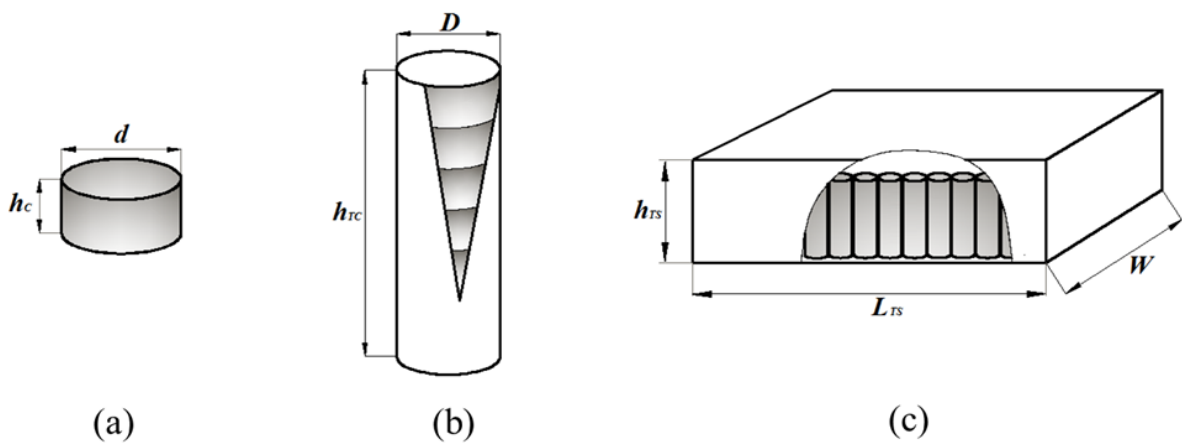
Figure 6.1 Schematic diagrams of a CPCM module (a), a TES component (b), and a TES device (c).
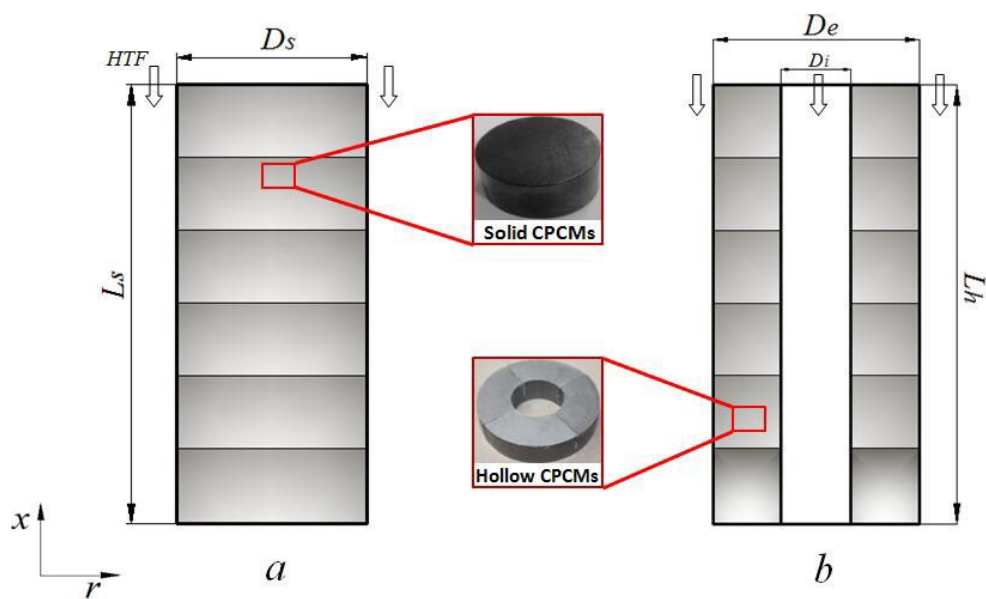
Figure 6.2 CPCM components: (a) tube based component and (b) concentric tube based component.

Table 6.1 Thermophysical properties of eutectic carbonate salt, MgO particles and graphite.

Materials	Density /Kg·m^{-3}	Thermal conductivity /W·m^{-1}K^{-1}	Heat capacity /J·g^{-1}K^{-1}	Melting point /K	Melting heat /J·g^{-1}
LiNaCO$_3$ (Li$_2$CO$_3$:Na$_2$CO$_3$=1:1)	2100	2.0	1.3	773.35	348.5
MgO	3580	0.5	1.0	3125	
Graphite	1900	129	0.66	3773	

6.1.2 Mathematical mode formulation

To establish a mathematical model for studying heat transfer behaviour of CPCM based TES component and device, the following assumptions are made:

(1). The CPCM modules are homogeneous and isotropic in terms of their thermophysical properties.

(2). The inlet velocity and initial temperature of the HTF are constant.

(3). The problem is considered as two-dimensional due to the symmetrical geometry.

Under the above assumptions, and consider the problem in cylindrical co-ordination, the model consisting of mass balance, momentum balance and energy balance equations can be written as follows:

First, governing equations for the HTF are given:

Continuity equation (mass balance)

$$\frac{1}{r}\frac{\partial}{\partial r}(rv)+\left(\frac{\partial u}{\partial x}\right)=0 \tag{6.1}$$

where u and v are HTF velocities in the x and r coordinates, respectively.

Momentum equations (Momentum balance)

x-direction

$$\frac{\partial u}{\partial t}+v\frac{\partial u}{\partial r}+u\frac{\partial u}{\partial x}=\mu_f\left[\frac{1}{r}\frac{\partial}{\partial r}\left(r\frac{\partial u}{\partial r}\right)+\frac{\partial^2 u}{\partial x^2}\right]-\frac{1}{\rho_f}\frac{\partial p}{\partial x} \tag{6.2}$$

r-direction

$$\frac{\partial v}{\partial t}+v\frac{\partial v}{\partial r}+u\frac{\partial v}{\partial x}=\mu_f\left[\frac{1}{r}\frac{\partial}{\partial r}\left(r\frac{\partial v}{\partial r}\right)-\frac{v}{r^2}+\frac{\partial^2 v}{\partial x^2}\right]-\frac{1}{\rho_f}\frac{\partial p}{\partial r} \tag{6.3}$$

where μ_f is the HTF viscosity, ρ_f is the HTF density, p is pressure and t is time.

Energy equation (Energy balance)

$$\rho_f c_f\left(\frac{\partial T_f}{\partial t}+v\frac{\partial T_f}{\partial r}+u\frac{\partial T_f}{\partial x}\right)=k_f\left[\frac{1}{r}\frac{\partial}{\partial r}\left(r\frac{\partial T_f}{\partial r}\right)+\frac{\partial^2 T_f}{\partial x^2}\right] \tag{6.4}$$

where c_f is the specific heat of the HTF, k_f is the thermal conductivity of the HTF, and T_f is the HTF temperature.

Second, the governing equations for the CPCM are discussed. Due to the involvement of PCM, the enthalpy-porosity theory [167-177] is used, and the energy equation can be written as [82]:

$$\rho_{eff}\frac{\partial H}{\partial t}=k_e\left[\frac{1}{r}\frac{\partial}{\partial r}\left(r\frac{\partial T_C}{\partial r}\right)+\frac{\partial^2 T_C}{\partial x^2}\right] \tag{6.5}$$

Equation (6.5) has an additional assumption that the natural convection and thermal radiation within the phase change region is negligible. This is justified by the fact that PCM is confined in the interparticle voids of CSM. In above equation, ρ_e and k_e are respectively the effective density and thermal conductivity of the CPCM, T_f is the CPCM modules temperature. H is the specific enthalpy defined as a sum of the sensible enthalpy (h) and latent enthalpy (ΔH):

$$H = h + \Delta H \tag{6.6}$$

with the sensible enthalpy given by:

$$h = h_{ref} + \int_{T_{ref}}^{T_C} c_{pcm} dT \tag{6.7}$$

where h_{ref}, T_{ref} and c_{pcm} are respectively the enthalpy at a reference temperature, the reference temperature and the specific heat of PCM at a constant pressure. The latent enthalpy in Equation (6.6) is related to the liquid phase fraction (β) during phase change and specific latent heat of the CPCM (L) as:

$$\Delta H = \beta L \tag{6.8}$$

with β expressed by the following equation:

$$\beta = \begin{cases} 0 & \text{if } T_C \leq T_s \\ \dfrac{T_C - T_s}{T_l - T_s} & \text{if } T_s \leq T_C \leq T_l \\ 1 & \text{if } T_C \geq T_l \end{cases} \tag{6.9}$$

The effective thermal conductivity of CPCM modules has been discussed in chapter 5, and can be determined by Zehner-Schlunder's model [151, 152]:

$$\frac{k_e}{k_f} = 1 - \sqrt{(1-\phi)} + \frac{2\sqrt{(1-\phi)}}{1-\lambda B}\left(\frac{(1-\lambda)B}{(1-\lambda B)^2} \ln\frac{1}{\lambda B} - \frac{B+1}{2} - \frac{B-1}{1-\lambda B} \right) \tag{6.10}$$

The effective density of CPCMs is calculated as:

$$\rho_e = (1-\xi)\rho_{csm} + \xi\rho_f \tag{6.11}$$

The effective heat capacity of CPCMs is given by:

$$\rho_e c_e = (1-\xi)\rho_{csm}c_{csm} + \xi\rho_f c_f \tag{6.12}$$

where ρ_f is the PCM-TCEM mixture density; c_{csm} and c_f are the specific heats of the CSM and the PCM-TCEM mixture, respectively; ξ is the volume ratio of the CSM in the CPCMs.

The effective density and specific heats of the PCM/TCEM mixture can be calculated as the volume average of the thermophysical properties of the PCM and TCEM [178, 179]. The effective thermal conductivity of the mixture is evaluated by Maxwell model, as described in Equation (5.17) of chapter 5.

Third, the governing equations for the CPCM based TES components are similar to that described above for the CPCM modules except for the thermal resistance between CPCM modules, which will be discussed in section 6.1.3. The governing equations for the CPCM based TES device consist of the equations for the HTF and TES components and are the same as described above.

6.1.3 Thermal contact resistance between CPCM modules
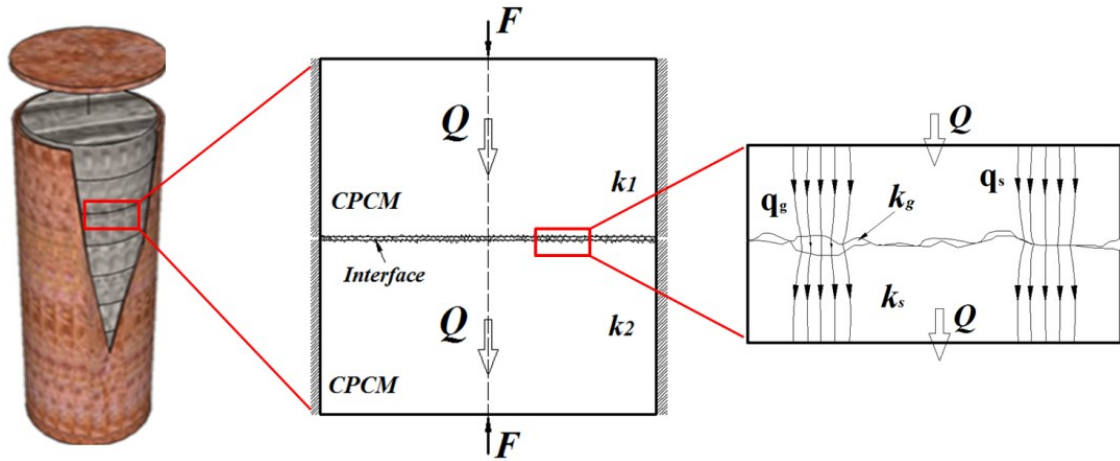
Figure 6.3 Contact of rough surfaces between CPCMs modules in a TES component.

As mentioned in the section 6.1.1, CPCMs based TES components are constructed by stacking CPCM modules, there is a gap between contacting surfaces filled with the interstitial stagnant gas unless the surface are perfectly smooth, which is unrealistic. The presence of the gaps between contacting surfaces leads thermal resistance. Heat transfer mechanisms in such a case are shown in Figure 6.3. Two paths can be identified from Figure 6.3 for heat transfer, one is through the contacting parts of the surfacing and the other is via a stagnant gas layer of the non-contacting parts. The low thermal conductivity of interstitial gas could cause a relatively high temperature drop between the two surfaces, which should be considered in studing the heat transfer behaviour of the CPCMs based TES component made by stacking the material modules. Thermal radiation and the natural convection across the contacting surfaces are not considered significant as the surface temperatures of CPCM modules are not very high and the fluid Grashof number is below 2500 (Natural convection is negligible at Grashof number below 2500) [180]. Consequently, heat transfer through the CPCM contacting surfaces is considered mainly via conduction, and the thermal contact resistance between two contacting surfaces consists of a microgap thermal resistance, $R_{g,}$ (gas path), and

thermal resistance of microcontacts, R_s, (solid path) [181-184]. The overall thermal contact resistance, R, can therefore be given by:

$$R = \left(\frac{1}{R_s} + \frac{1}{R_g} \right)^{-1} \tag{6.13}$$

Equation (6.13) assumes a one dimensional heat conduction problem with the two thermal resistances being in parallel.

The microcontact thermal resistance, R_s, can be estimated by the Bahrami's model [181],

$$R_s = \frac{0.565 H^* (\sigma / \delta)}{k_s F} \tag{6.14}$$

where $k_s = 2k_1 k_2 (k_1 + k_2)$ and $H^* = c_1 (\sigma^* / \delta)^{c_2}$, $\sigma^* = \sigma / \sigma_0$ and $\sigma_0 = 1 \mu m$. k_1 and k_2 are the thermal conductivities of the contacting surfaces, respectively; σ and δ are respectively the surface roughness and surface slope of the CPCMs, and c_1 and c_2 are correlation coefficients determined from the Vickers microhardness measurements [181].

The microgap thermal resistance, R_g, can be calculated by the Song's model [182]:

$$R_g = \frac{Y}{k_g A_g} \left[1 + \frac{M}{Y} + \frac{0.304 (\sigma / Y)}{(1 + M / Y)} - \frac{2.29 (\sigma / Y)^2}{(1 + M / Y)^2} \right] \tag{6.15}$$

where Y is the mean separation distance between the contacting surfaces, k_g is the gas thermal conductivity, A_g is the heat transfer area of the gas path, and M is a gas parameter defined as:

$$M = \left(\frac{2 - \alpha_{T1}}{\alpha_{T1}} + \frac{2 - \alpha_{T2}}{\alpha_{T2}} \right) \left(\frac{2\gamma}{1 + \gamma} \right) \frac{1}{Pr} \Lambda \tag{6.16}$$

where α_{T1} and α_{T2} are thermal accommodation coefficients corresponding to the two contact surfaces. Λ is the mean free path of the gas molecules at the prevailing pressure, P_g and temperatrure, T_g, and given by:

$$\Lambda = \frac{P_0}{P_g} \frac{T_g}{T_0} \Lambda_0 \tag{6.17}$$

6.1.4. Initial and boundary conditions for the model

The initial conditions are defined as follows:

t=0,　$T_{pcm}=T_0$　　　(charging process)　　　　　　　　　　　(6.18)

t=0,　$T_{pcm}=T_f$　　　(discharging process)　　　　　　　　　(6.19)

The boundary conditions are defined as follows:

(1). The HTF inlet is defined as velocity inlet where the inlet velocity and temperature are specified:

　　$u=u_{in}$ (constant or changed with time depending on the work condition)　　(6.20)

　　$T=T_{in,f}$ (constant or changed with time depending on the work condition)　　(6.21)

(2). The outlet is defined as outflow outlet.

(3). All the outside walls are set as adiabatic and no slip:

$$\left. \frac{\partial T}{\partial r} \right|_{r=r_0^+} = \left. \frac{\partial T}{\partial r} \right|_{r=r_0^-} = 0 \tag{6.22}$$

(4). The interfaces between the HTF and TES component as well as that between the CPCM modules are coupled-wall boundary condition for heat transfer:

$$k_w \frac{\partial T}{\partial r}\bigg|_{r=r_s} = k_f \frac{\partial T}{\partial r}\bigg|_{r=r_s} = 0 \quad \text{(HTF-TES component wall interface)} \qquad (6.23)$$

$$k_c \frac{\partial T}{\partial r}\bigg|_{r=r_w} = k_w \frac{\partial T}{\partial r}\bigg|_{r=r_w} = 0 \quad \text{(TES component wall interface-CPCM modules)} \qquad (6.24)$$

6.1.5 Numerical modelling

For all the cases reported in this work, calculation was performed by utilizing the commercial CFD software, Ansys Fluent, and the mesh of computational domain was built by using the software of Gambit. The User Define Function (UDF) program is used to account for the variable thermophysical coefficients of HTF and interpret the thermal contact resistance within the components. Governing equations were discredited by using the finite volume approach. The Second Order Upwind scheme was adopted for solving the momentum and energy equations while Pressure Staggering Option Scheme (PRESTO) scheme was used for the pressure correction equation. The coupling between pressure and velocity is conducted by the Semi-Implicit Pressure-Linked Equation (SIMPLE) algorithm. The under-relaxation factors for the velocity components, energy, pressure correction and liquid fraction were 0.5, 1, 0.3 and 0.9, respectively. The effects of time step and mesh size on the solution were carefully checked before the calculations. Convergence of numerical solution was examined at each time step, and the convergence criterion was set to 10^{-3} for the velocity and continuity equation and 10^{-6} for the energy equation.

6.2 Model verification

6.2.1 Experimental apparatus and procedure

The validity of the numerical model has been analysed by comparison between the numerical results and experimental data. Figure 6.4 (a) shows a schematic diagram of the experiment setup, which mainly consists of a cylindrical furnace, a single tube based component and a data collecting system. The cylindrical furnace was made of stainless steel, with inner diameter of 0.22 m and length of 1.4 m. In order to reduce the heat loss to the environment, the outer wall of the furnace was thermally well insulated. Three K-type thermocouples were used to measure temperatures at points as illustrated in Figure 6.4 (b). The thermocouples T1 and T2 were located in the middle part of the CPCM component, and 15 mm and 25 mm respectively into the component. The thermocouple T3 is placed at the exit of the TES component to monitor the end of charging and discharging processes. An additional thermocouple T4 was used to measure the inlet temperature of the HTF. All thermocouples were connected to a data logging unit interfaced to a computer. Heat supply to the experimental system was achieved by burning liquefied gas, and hence the HTF was exhaust gas from the combustion. The volumetric flowrate of the HTF was kept at 30.1 Nm^3/h for heat storage process and 28.5 Nm^3/h for heat release process. The experiments were repeated to ensure the repeatability of the results.

(a)

(b)
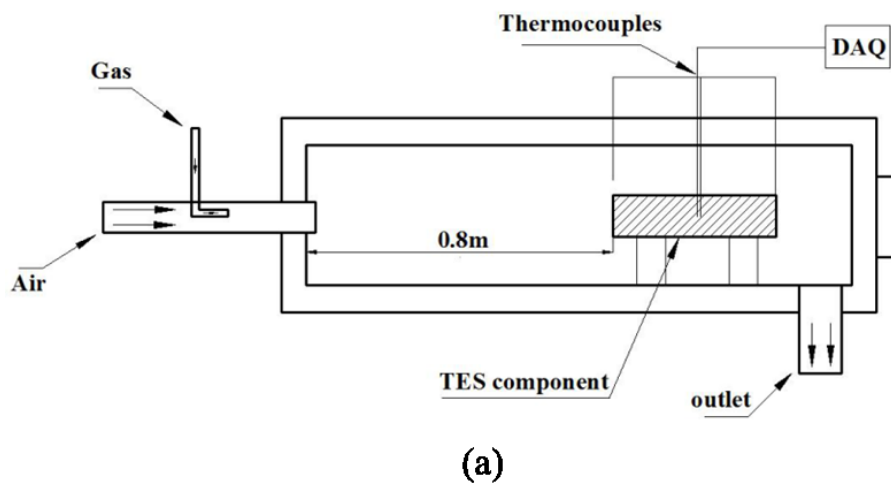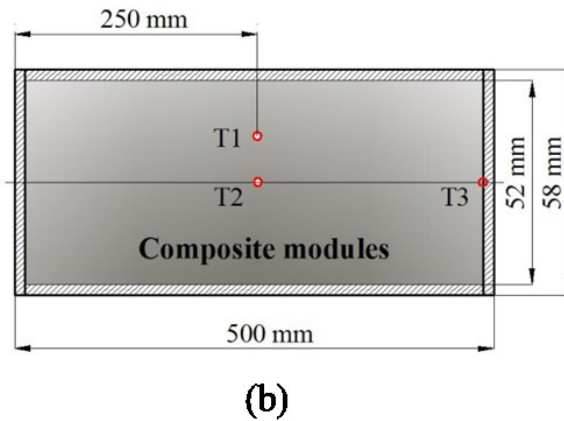
Figure 6.4 Diagrammatic sketches of the experimental apparatus: (a) experimental set up and (b) measurement points.

6.2.2 Comparison between experimental and numerical results

Figure 6.5 compares the measured and calculated temperature profiles at Location T_1 and T_2 for both charging and discharging processes. The surface roughness of CPCMs modules was measured by using the Atomic Force Microscope (AFM, NanoWizard III NanoScience), which gave an average value of 3 μm. Reasonably good agreement can be seen between modelling and experimental data. During charging process, three stages can be identified from Figure 6.5 (a). Stage 1 is the sensible heat storage during which the temperature increases rapidly with time; Stage 2 is the latent heat storage with phase change occurring and little changes in temperature; and Stage 3 is the sensible heat storage with the temperature increasing again with time until thermal equilibrium. The PCM is seen to start to melt at ~ 2700 s, and it takes about 2000 s to complete the phase change. The discharging process is expected to experience three stages as well. However, as shown in Figure 6.5 (b), only two stages are apparent, and the release of the sensible heat in Stage 1 should give a sharp decrease in temperature. This does not occur possibly due to the data logging process was not capture as shown clearly in Figure 6.5 (b), where the starting temperature is at the

phase change temperature. Stage 2 corresponding the period during which the changes in temperature are very small due to phase change. Stage 3 corresponds to the rapid drop in the temperature after phase change completes. The small changes in temperature during phase change are mainly due to the presence of the non-phase-change materials in the formulation. The relatively small difference in T_1 and T_2 suggests that the heat transfer process inside the CPCM modules is fairly quick and is dominated by heat conduction particularly in the charging process. As graphite powder was used to fill the gap between the CPCMs modules and the tube wall, the actual effective thermal conductivity is expected to be higher than the value used this study. This may be a reason for the small difference between experimental data and modelling results. The good agreement between experimental results and the modelling also indicates that the mathematical modelling could be used to give good prediction of the heat transfer behaviour at the component level.
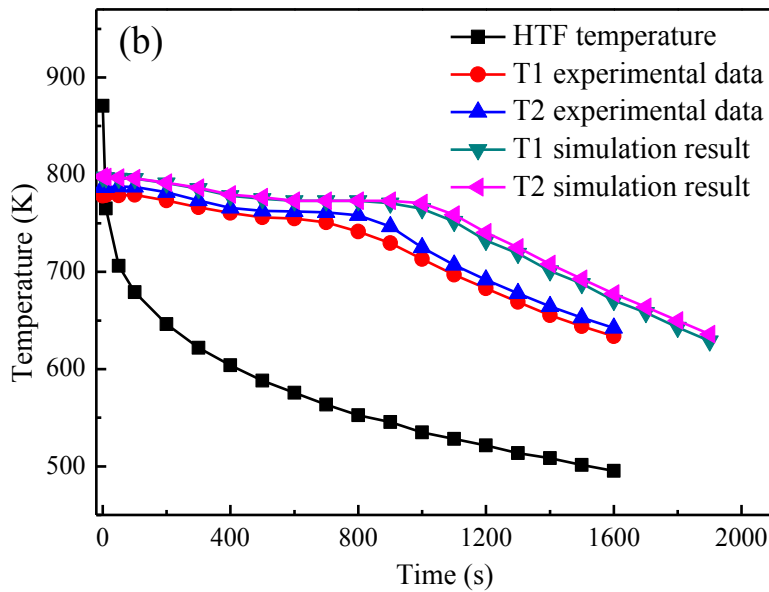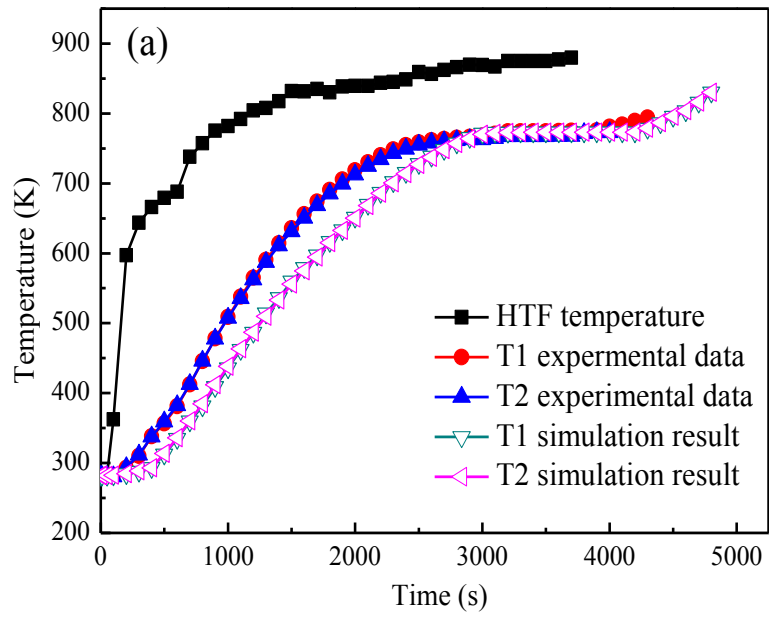
Figure 6.5 Comparison between experimental and numerical modelling: (a) charging process; (b) discharging process.

6.3 Numerical results and discussion

Having validated the modelling using the experimental data, a series of numerical analysis have been carried out to investigate the heat transfer behaviour of CPCMs based TES components and devices. All numerical models have performed similar to those used for the numerical model validation. The influences of properties, module size and surface roughness of CPCM modules as well as flow conditions of HTF are investigated.

6.3.1 Linking materials properties to TES component performance

6.3.1.1 Effect of CPCMs properties

CPCMs properties depend mainly on their formulation. Three cases are considered in this regard, as shown in Table 6.2. One can see that the mass fraction of the PCM is kept at 50% whereas the mass fraction of the CSM varies between 30% and 45%, and the corresponding mass fraction of the TCEM changes between 20% and 5% in Case 1. In Case 2, the mass ratio of PCM to CSM is kept at 1:1, while the mass fraction of TCEM changes between 5% and 20%. In Case 3, the mass fraction of CSMs is kept at 50%, while the mass fractions of the PCM and the TCEM are varied from 30% to 45% and 20% to 5%, respectively. In the analysis, the single tube based component was used. The dimensionless thickness of the CPCM modules, h_s/D_s was taken as 0.172, and the dimensionless diameter of the modules, d_s/D_s, was 0.862. The average surface roughness of CPCMs module was set as 3 μm. The total amount of CPCM modules inside the component was 50.

Table 6.2 Cases for studing the effect of CPCM*.

	Case 1	Case 2	Case 3
m_{PCMs}: m_{TCEMs}: m_{CSMs}	50:20:30	40:20:40	30:20:50
m_{PCMs}: m_{TCEMs}: m_{CSMs}	50:15:35	42.5:15:42.5	35:15:50
m_{PCMs}: m_{TCEMs}: m_{CSMs}	50:10:40	45:10:45	40:10:50
m_{PCMs}: m_{TCEMs}: m_{CSMs}	50:5:45	47.5:5:47.5	45:5:50

*(1) The CPCM properties depend on the formulation, so the above combination of CPCM gives different properties, e.g. density, thermal conductivity, etc. Such properties can be calculated by Equations (6.10-6.12) and the results are listed in following table 6.3. (2) All modules are assumed to have the same size and are made under the same fabrication conditions.

Table 6.3 CPCM properties of different formulation cases

Different formulation cases		Density /$Kg·m^{-3}$	Heat capacity /$J·g^{-1}K^{-1}$	Thermal conductivity /$W·m^{-1}K^{-1}$	Melting heat /$J·g^{-1}$
	50:20:30	2504	1.082	3.8481	174.25
Case 1	50:15:35	2588	1.099	3.1210	174.25
(m_{PCMs}: m_{TCEMs}: m_{CSMs})	50:10:40	2672	1.116	2.3595	174.25
	50:5:45	2756	1.133	1.8543	174.25
	40:20:40	2652	1.052	3.2953	139.4
Case 2	42.5:15:42.5	2699	1.0765	2.7369	148.11
(m_{PCMs}: m_{TCEMs}: m_{CSMs})	45:10:45	2746	1.101	2.4364	156.825
	47.5:5:47.5	2793	1.1255	1.8802	165.53
	30:20:50	2800	1.022	2.919	104.55
Case 3	35:15:50	2810	1.054	2.489	121.975
(m_{PCMs}: m_{TCEMs}: m_{CSMs})	40:10:50	2820	1.086	2.2708	139.4
	45:5:50	2830	1.118	1.6936	156.825

Figure 6.6 shows the total charging time of the single tube based component, together with the energy storage density of the CPCMs for the three cases, as a function of TCEM (graphite) loading. It can be seen that, for all the three cases, both the total charging time and the energy storage density decrease with increasing mass fraction of TCEM. When the TCEM mass fraction increases from 5% to 20%, the total charging time of the component decreases from 9800 s to 4600 s for Case 1, 9515 s to 4130 s for Case 2 and 9195 s to 3615 s for Case 3, respectively. This is because, for CPCM modules with a fixed mass fraction of PCM, the stored thermal energy is almost constant, and hence a higher mass fraction of TCEM gives a higher thermal conductivity. This implies a faster heat transfer rate and the shorter charging/discharging time. As discussed before, TCEMs such as graphite used in this work often give a poor wettability, leading to a loose structure and a low energy density. Optimisation of the formulation is therefore important.
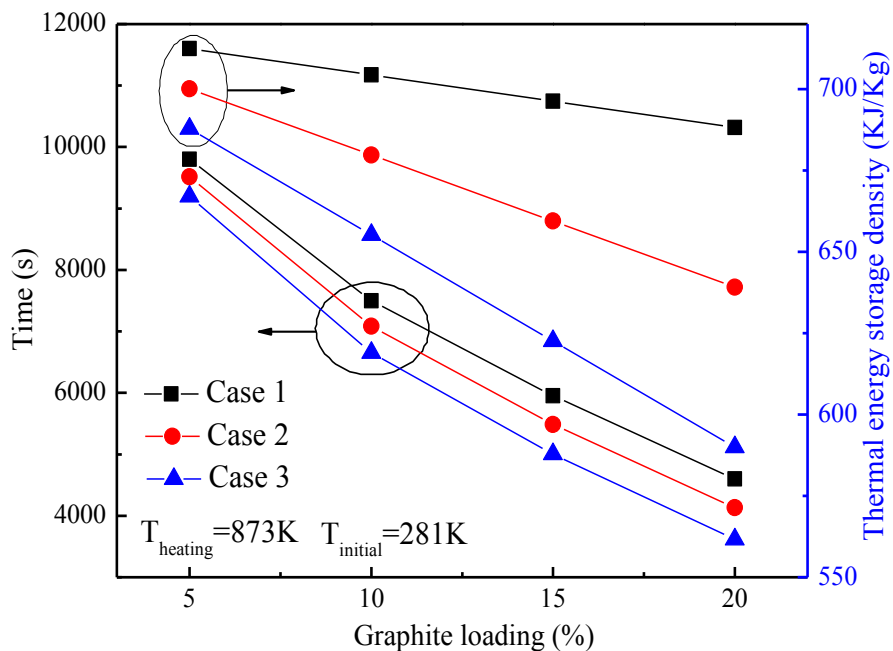
Figure 6.6 The total charging time of component and thermal energy storage density of CPCMs as a function of graphite loading.

6.3.1.2 Effect of surface roughness of CPCM modules

The influence of CPCM surface roughness was investigated on the charging and discharging processes. In the study, the dimensionless thickness of CPCM modules was fixed at 0.172, whereas the dimensionless diameter was 0.862. The number of CPCM modules within a single tube based TES component was 50. The mass ratio of PCM, CSM and TCEM was 50:40:10. The range of surface roughness examined was 0-20 μm. Figure 6.7 shows the results in the form of charging and discharging times as a function of surface roughness. It is seen that the total time for the TES component to complete the charging and discharging processes increases with increasing surface roughness. When the CPCM module surface roughness in increased from 0 μm to 20 μm, the total charging time is increased by ~ 10.1%, whereas the discharging time by ~ 12.2%. It is noticed that there is little effect when the surface roughness is below ~ 600 nm (see the enlargement in Figure 6.7). The surface roughness effect becomes more significant when its value is above ~ 800 nm. The above observations can be explained by the theory presented earlier in this thesis on the interfacial thermal resistance, which consists of two elements, solid path and gas path, and the larger the surface roughness, the larger the gap between the contacting surfaces and the larger the thermal resistances through both the paths.
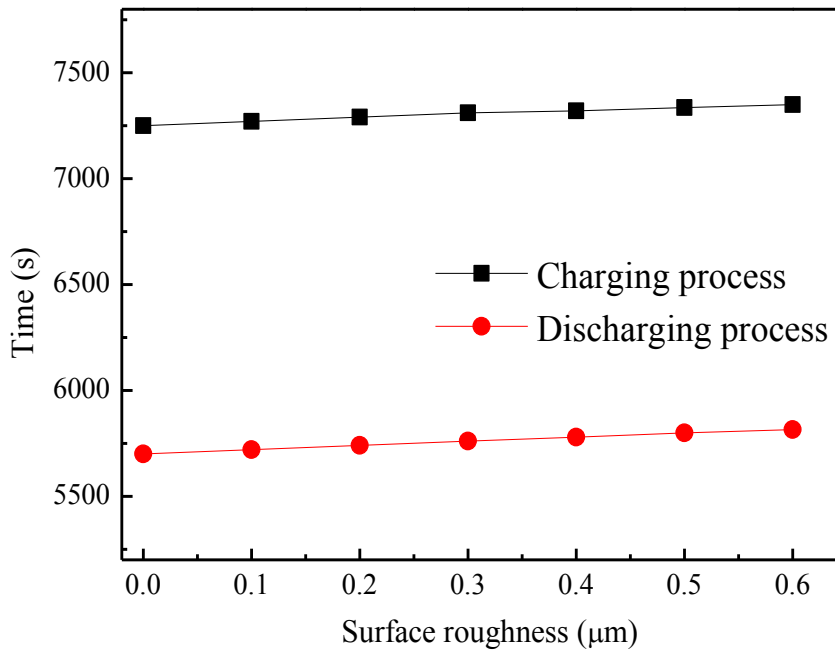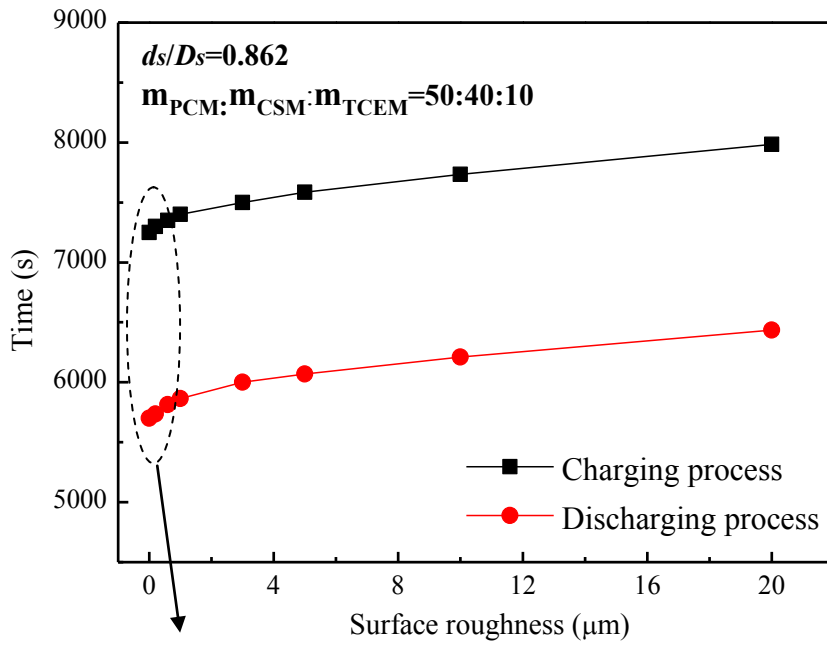
Figure 6.7 Effects of surface roughness of CPCM module on charging and discharging processes; charging: T_{HTF}=873 K, $T_{initial}$=281 K; discharging: T_{HTF}=473 K, $T_{initial}$=873 K.

6.3.1.3 Effects of CPCM module size and HTF velocity

In this set of analyses, the dimensionless thickness of the CPCM modules was considered to vary between 0.172 and 0.862. For the given length of TES component, the corresponding number of CPCM modules changed from 10 to 50. The dimensionless diameter of the CPCM modules was kept at 0.862, and the mass fraction of the PCM, CSM and TCEM was 50:40:10. The average surface roughness of CPCM modules was set as 3 μm. Figure 6.8 (a) shows the effect of CPCM module size on the charging and discharging times of the single tube based component. Both the charging and discharging times decrease with increasing thickness of the CPCM module. An increase in the module thickness from 10 mm to 50 mm, this corresponds to the decrease of the number of modules within the component from 50 to 10, leads to a reduction in the charging and discharging processes by 1.4 and 1.41 times, respectively. A thicker CPCM module means less contact resistance and hence a better heat transfer performance. The results suggest that thick CPCM modules be beneficial for the thermal performance of CPCMs based TES components. However, thick modules can present manufacture difficulties, particularly the uniformly in the microstructure of the material modules. As a result, optimisation is needed by taking into account of both thermal performance and fabrication process.
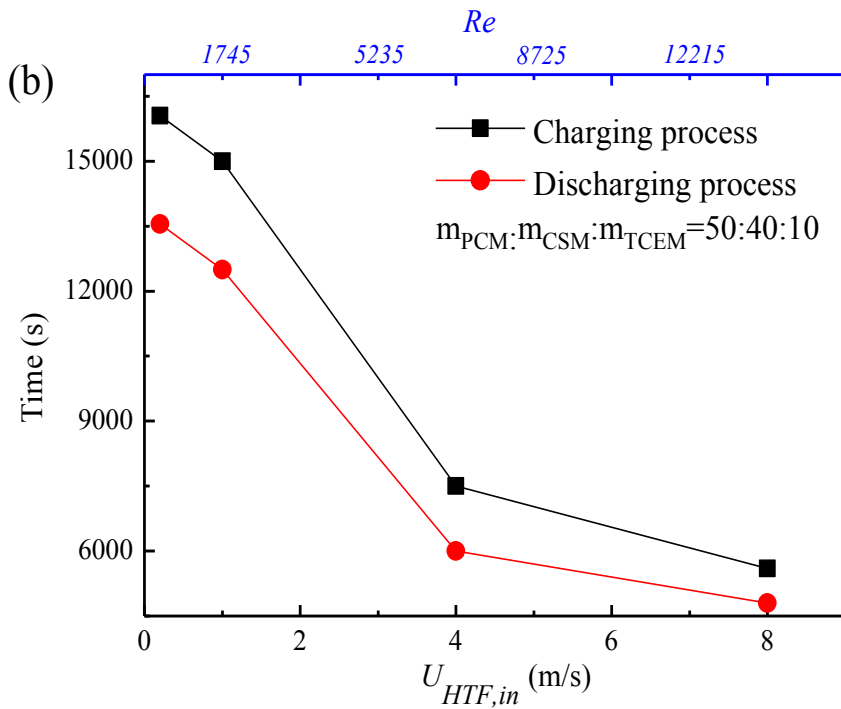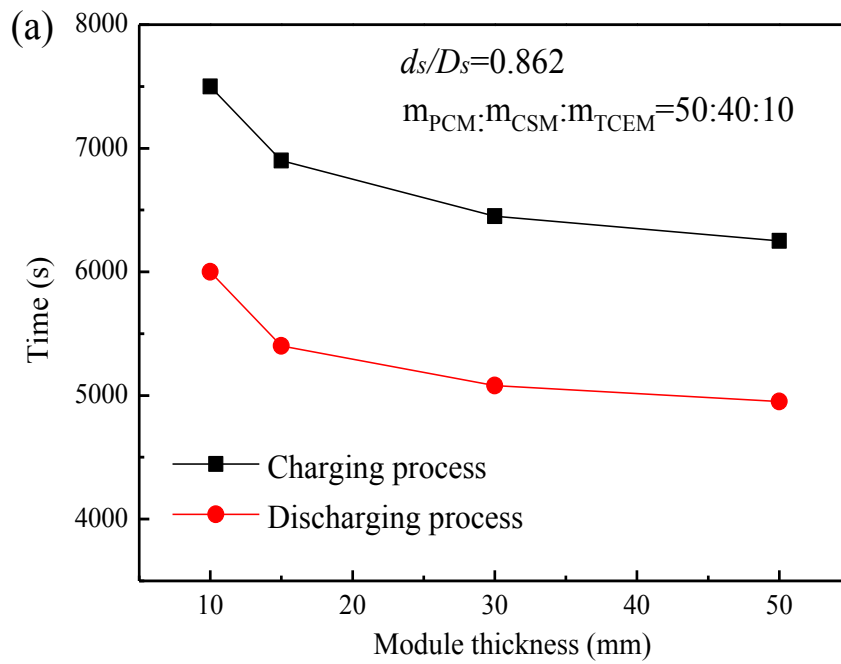
Figure 6.8 Effects of CPCM module size (a) and HTF velocity (b) on charging and discharging processes; charging: T_{HTF}=873 K, $T_{initial}$=281 K; discharging: T_{HTF}=473 K, $T_{initial}$=873 K.

The effect of HTF flow condition on the heat transfer performance of CPCM based TES components is of great interest in terms of design and optimisation of CPCM based TES components. This effect was examined with a focus on the HTF inlet velocity, which was studied over a range of 0.2 $m\ s^{-1}$ to 8 $m\ s^{-1}$ for both the charging and discharging processes, corresponding to the Reynolds number (defined as $Re = \rho_{HTF} U_{in} D / \mu$) between 349 and 13960. Here, ρ_{HTF} is the density of HTF, U_{in} is the HTF inlet velocity, D is the inner tube diameter of furnace. The CPCM module studied had a dimensionless thickness of 0.172, and dimensionless diameter of 0.862, corresponding to 50 CPCM modules within the component. The mass ratio of the PCM, CSM and TCEM was 50:40:10. An average roughness of 3 μm was set for the CPCM modules. Figure 6.8 (b) shows the results. An increase in the HTF velocity accelerates both charging and discharging processes and hence a decrease in the heat storage and releases times. A close inspection of the curves in Figure 6.8 (b) indicates that rate of decrease in the charge/discharge time is low at HTF velocity below ~ 1 m/s. The rate increases sharped at the HTF velocity above ~ 1 m/s until 4 m/s beyond which less significant changes to the rate is observed. The 1 m/s HTF is approximately at the laminar to turbulence transition, indicating external heat transfer to the TES component plays an important role in the overall thermal performance. At HTF velocity above 4 m/s, external heat transfer appears to be not a rate-limiting step and the overall thermal performance is controlled by the heat transfer within the TES component.

6.3.1.4 Comparison between two configurations of CPCM based TES components

Figure 6.9 compares the average temperature inside the CPCM based TES component in the charge (a) and discharge (b) processes. In this set of study, the dimensionless thickness of

solid and hollow CPCM modules was set to 0.172; the dimensionless outer and inner diameters of the concentric CPCM modules were respectively set as 0.866 and 0.236 in order to maintain the same mass of CPCM modules inside the two TES components; and the mass ratio of the PCM, CSM and TCEM was 50:40:10; an average surface roughness of the two types of CPCM modules was set as 3 μm. From Figure 6.9, one can see that the effect of HTF velocity agrees with that presented in section 6.3.1.3 for both types of TES components. For a given set of conditions, the concentric tube based component shows a better heat transfer performance than the single tube based component though the difference is not massive. This is because the concentric tube based component has a larger heat transfer area with the HTF. Quantitatively, the concentric tubular TES component gives respectively overall charge and discharge times 10% and 15% shorter than the single solid tubular TES component.

(a)
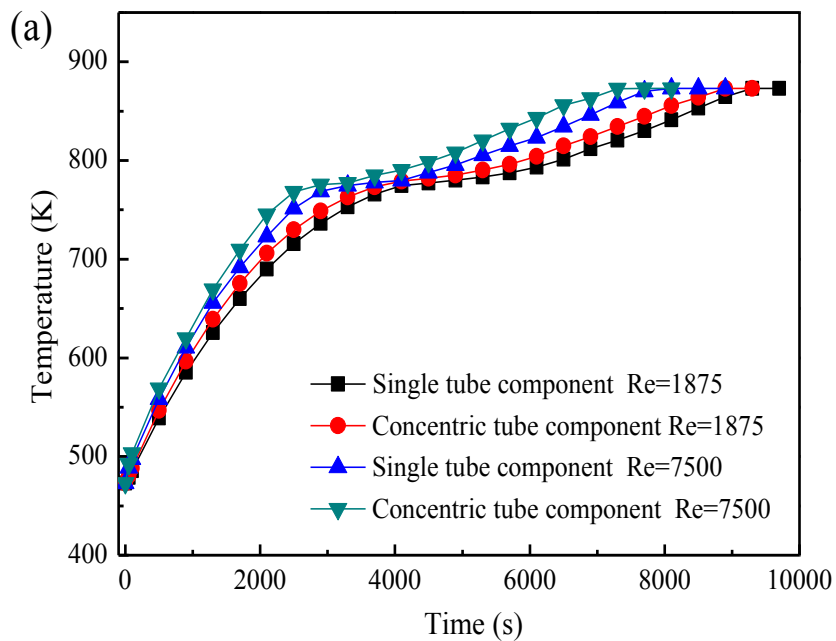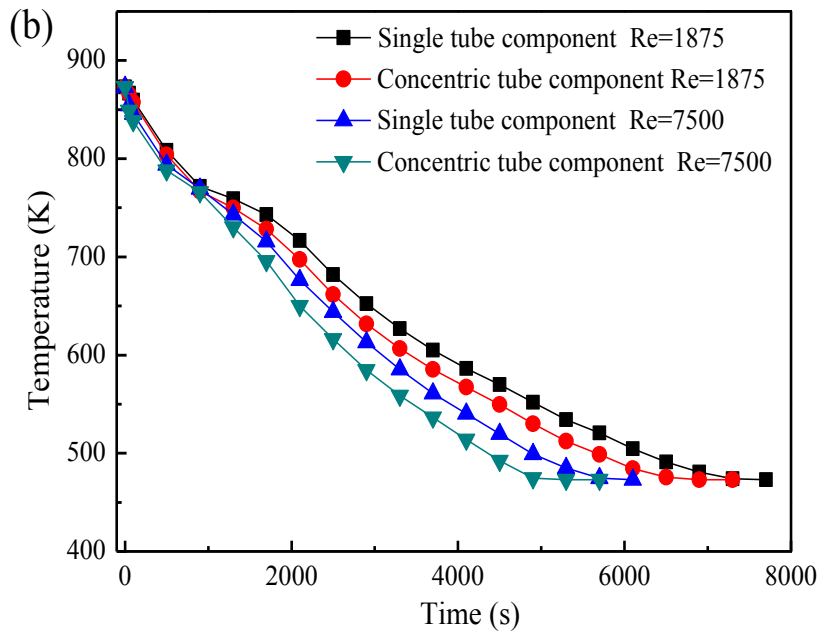
Figure 6.9 Comparison of two CPCMs based TES components: (a) charging process; (b) discharging process.

6.3.2 Linking TES component behaviour to TES device performance

This section presents the results of heat transfer behaviour of TES device made from the TES components. Three configurations of TES components were considered, parallel, interlaced and trapezoidal arrangements with the same number of the CPCM modules, and the same number of TES components of 45. Figure 6.10 illustrates schematically the three arrangements. In all cases, the length of the TES device is 640 mm. Configuration 1 is the parallel arrangement with 9 rows each containing 5 TES components (Figure 6.10 (a)). The width of the configuration 1 is 310 mm. Configuration 2 is the interlaced arrangement with 10 rows each containing either 4 or 5 TES components (Figure 6.10 (b)). The width of the configuration 2 is also 310 mm. Configuration 3 is the trapezoidal arrangement with 9 rows each containing 5 TES components. The widths of the top and bottom sides of the trapezoid

are respectively 280 mm and 340 mm. For comparison purpose, the total volume of the three

configurations is the same; so is the volume fraction of the TES component, which is 44.5%.

Air is used as the HTF and has a flow rate of 5.58 $m^3 \cdot h^{-1}$. The initial temperature of CPCM

modules and HTF temperature are set as 600 K and 873 K, respectively. The mass ratio of the

PCM, CSM and TCEM is taken as 50:40:10, and the dimensionless diameter and thickness of

the CPCM modules are set respectively as 0.862 and 0.172. The diameter of TES component

is set as 50 mm.
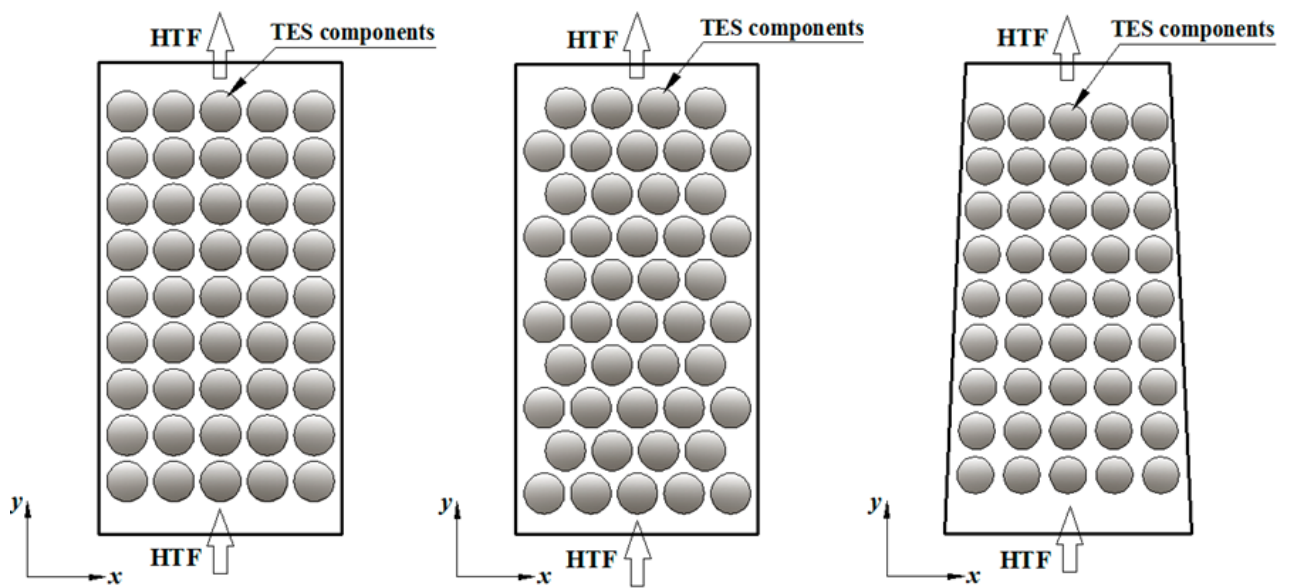
**Figure 6.10 Schematic arrangements of TES components for parallel configuration (a),
interlaced configuration (b), and trapezoidal configuration (c).**

Figure 6.11 shows the numerical results of the flow field for the three configurations.

Different flow parts are apparent in the three configurations. The parallel configuration shows

six main flow passages, as shown in Figure 6.11 (a), with the maximum HTF velocity of 0.08

$m \cdot s^{-1}$ occurring between neighbouring TES components. The interlaced arrangement of TES

components gives a more disturbed flow and the highest velocity is around 0.108 $m \cdot s^{-1}$

between the TES component and the wall (Figure 6.11 (b)). The trapezoidal configuration

shows six main flow passages with the maximum flow velocity of 0.133 $m \cdot s^{-1}$ occurring

between neighbouring TES components at the exit region of the device due to reduced cross-sectional area (Figure 6.11 (c)).
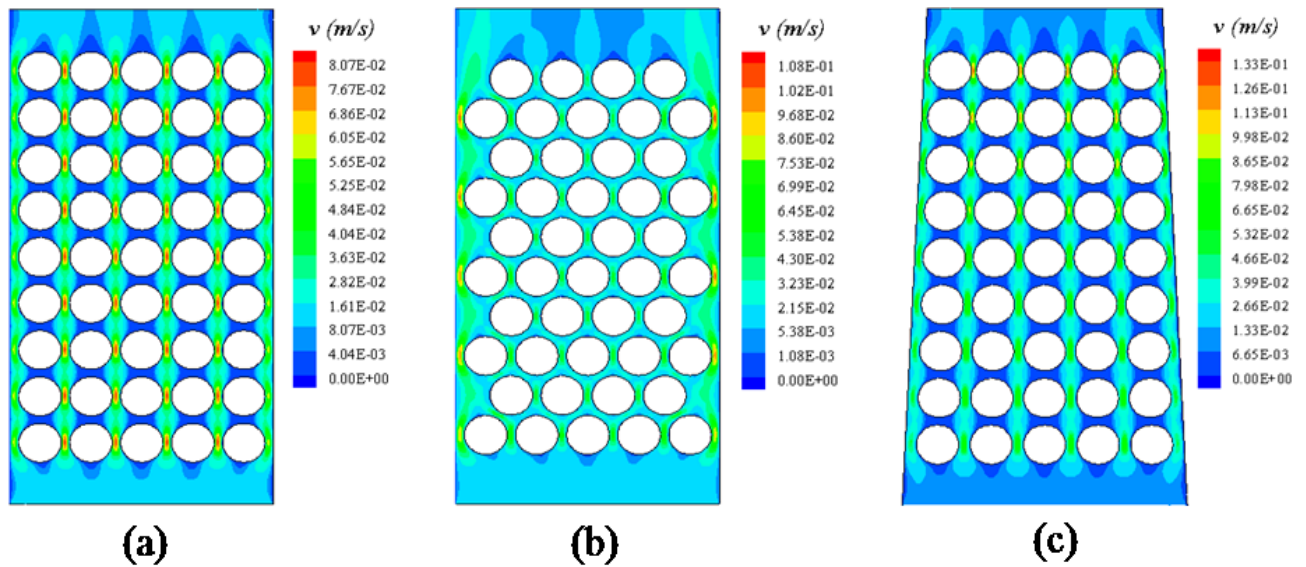
Figure 6.11 Flow fields of the Parallel configuration (a), the interlaced configuration (b), and (c) the trapezoidal configuration (c).

Figure 6.12 shows temperature distributions within the three configurations at the charging process of 8 hours. It can be seen that compared with the interlaced configuration, the temperature distributions along the X axis direction (at y=0.32m) within the trapezoidal and parallel configurations are more uniform due to the uniform flow passages, as shown in Figure 6.12 (a). In interlaced configuration, the disturbed flow paths lead to a non-uniform HTF flow condition and thus a non-uniform heat transfer rate. The TES components near the wall are heated intensely and the temperature increases more quickly than the centre of device as the flow rate near the wall is higher than that in the centre area (see Figure 6.11). This is the reason that a relatively inward bending curve of temperature distribution is obtained. It also can be seen that the temperature distribution inside the trapezoidal configuration is the highest than the other two configurations. This is because the reduced

sectional area arrangement not only offers a uniform flow passage, but also gives an enhancement on the HTF velocity.
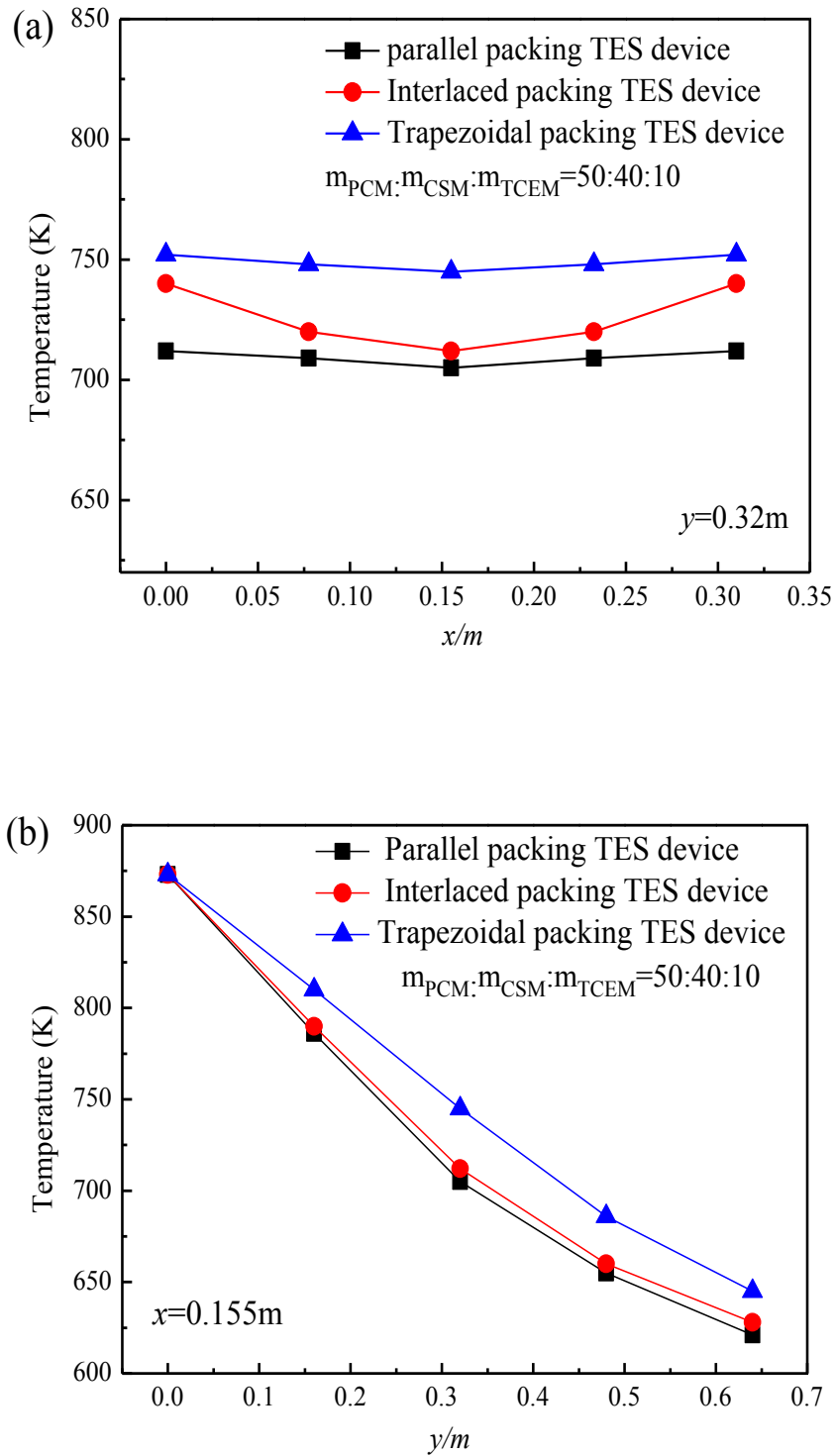
Figure 6.12 Temperature distributions within the three configurations during charging process (8 hours).

Figure 6.13 compares the HTF outlet temperatures of the three configurations, which agree with the above analyses that trapezoidal configuration has the best heat transfer performance and is superior to other two configurations. It can be seen that when the HTF inlet temperature and CPCM modules initial temperature are respectively set as 873 K and 600 K, the total charging time is 31.6 h for parallel configuration, 21.6 h for interlaced configuration, and 14.1 h for trapezoidal configuration. Compared with the parallel and interlace configurations, the fully charging process of trapezoidal configuration is shortened around 55.6% and 34.8%, respectively. It should be pointed that the pressure drop required for the trapezoidal configuration is also higher than that for other two configurations. However, it is very lower at the investigated work conditions and can be neglected compared with the practical industrial applications.
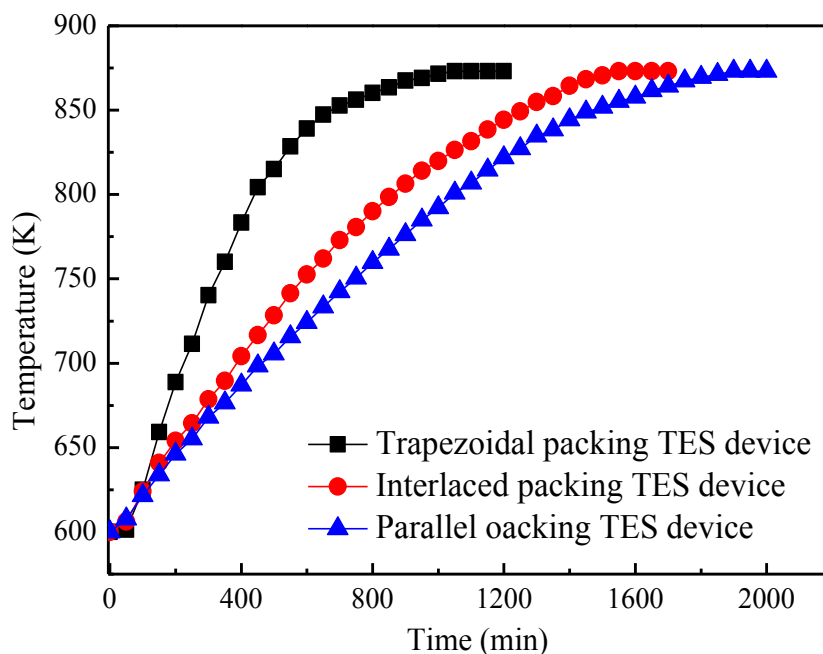
Figure 6.13 comparison of the HTF outlet temperature of the three configurations.

6.4 Conclusions of chapter 6

Heat transfer behaviour of CPCMs based TES at component and device levels have been investigated in this chapter. This includes the formulation of a numerical model for transient heat transfer in CPCM modules and TES components and validation of the model via experiments. The model considers the thermal contact resistance within the component, and the influences of materials properties, module size and surface roughness of CPCMs as well as flow conditions of HTF were investigated. The CPCMs consist of a carbonate salt based PCM, a TCEM and a CSM. The following conclusions were obtained under the conditions of this work:

(1). The modelling results agree reasonably well with the experimental data, indicating the validity of the numerical model. A constant mass ratio of PCM in CPCMs module gives the best combination of heat transfer rate and heat storage density. A higher mass ratio of TCEM in CPCM module gives a higher thermal conductivity at CPCMs level and hence a shorter charging/discharging process at component and device levels.

(2). The thermal contact resistance between the contacting rough CPCM modules should be considered and the influence is found to be significant when the surface roughness of CPCMs is larger than 800 nm.

(3). A larger CPCM module and a higher HTF inlet velocity give a more remarkable enhancement of the heat transfer behavior at the component level. For a given set of conditions, the concentric tube based component offers better heat transfer performance compared with the single tube based component, with a total heat storage time and release time approximately 10% and 15% shorter, respectively.

(4). Trapezoidal packing TES device offers the best heat transfer performance and is superior to parallel and interlaced packing devices. At the same set of other working conditions, the total heat storage time for a trapezoidal packing device is shorter than parallel and interlaced packing devices, respectively 55.6% and 34.8%.

Chapter 7 Conclusions and Future Work

This chapter summarizes the main conclusions from this thesis and gives recommendations for future work.

7.1 Summary of main conclusions

This thesis concerns TES materials and device challenges with an aim to establish a relationship between TES device level performance to materials properties. This is a multiscale problem. Carbonate salt based composite phase change materials (CPCMs) were used as example for the study, which consist of a carbonate based phase change material (PCM), a thermal conductivity enhancement material (TCEM) and a ceramic skeleton material (CSM). Both mathematical modelling and experiments were carried out to address the multiscale problem. The following are the main conclusions:

(1). The carbonate salt-MgO system presents an excellent wettability and the wettability is a fairly strong function of microstructure and hence surface energy of the MgO substrates fabricated at different sintering temperature. The non-sintered MgO substrate has a loose surface particle packing with large pores and crevices, leading to significant salt infiltration. The corresponding contact angle is measured to be 25 °. The contact angle of the salt on the sintered MgO increases with increasing sintering temperature of the MgO substrate fabrication and approaches ~40° for the single MgO crystal. The effect of the sintering temperature for making the MgO substrate could be linked to the surface energy due to the surface microstructures.

(2). Salt motion occurs within the composite structure during repeated heating and cooling cycles. Such motion is likely to be associated with volume change induced by phase change

and surface tension due to intermolecular forces. The motion could provide a force to drag the CSM (MgO) to move within interparticle void of the composit microstructure. The motion could form a shear force and break graphite flakes. The migration during the melting-solidification processes leads to a more homogenous distribution of both the salt and CSM/TCEM particles and an increase in the density of the microstructure.

(3). The CSM (MgO) particles in the single carbonate salt based composites would sinter and form a porous structure due to the use of a high sintering temperature. This reduces significantly the swelling effect due to the presence of low surface energy graphite and restricts particle motion during melting-solidification thermal cycles.

(4). The addition of graphite flakes in the formulation leads to reduced wettability of the carbonate salt on MgO substrates and limits particle migration within the composites. The extent of the reduction increases with increasing graphite flake loading.

(5). The proposed prediction model for effective thermal conductivity of single carbonate salt based CPCMs presents a good comparison with the experimental data. The Zehner-Schlunder's model and Raticffr's model can be used to predict the effective thermal conductivity of eutectic carbonate salt based CPCM with reasonable accuracy. The proposed model compares fairly well with the Alexander's sintering model for the single carbonate salt based CPCMs fabricated with small sized light MgO. For the CPCMs fabricated by large sized heavy MgO, the experimental data is better estimated by the model of Ratciffr.

(6). The modelling results for transient heat transfer in CPCM modules and TES components agree reasonably well with the experimental data, indicating the validity of the numerical model. A constant mass ratio of PCM in CPCMs module gives the best combination of heat transfer rate and heat storage density. A higher mass ratio of TCEM in CPCM module gives a

higher thermal conductivity at CPCMs level and hence a shorter charging/discharging process at component and device levels.

(7). The thermal contact resistance between contacting rough CPCM modules should be considered and the influence is found to be significant when the surface roughness of CPCMs is larger than 800 *nm*. A larger CPCM module and a higher HTF inlet velocity give a more remarkable enhancement of the heat transfer behavior at the component level.

(8). For a given set of conditions, the concentric tube based component offers a better heat transfer performance compared with the single solid tube component, with a total heat storage time and release time approximately 10% and 15% shorter, respectively.

(9). Trapezoidal packing TES device offers the best heat transfer performance and is superior to parallel and interlaced packing devices. At the same set of other working conditions, the total heat storage time for a trapezoidal packing device is shorter than parallel and interlaced packing devices, respectively 55.6% and 34.8%.

7.2 Recommendations for future work

Although some interesting and promising results have been obtained in this thesis, there are still a number of areas worth to be further investigated at TES materials and device levels. They are listed as following:

(1). To fabricate a novel MgO matrix based CPCMs: The CSM in the single carbonated salt based CPCMs could sinter and forms a porous structure at high sintering temperatures. However, the sintering temperature scope explored in this thesis (950 ~1000 ℃) is far lower than the CSM completely sintering temperature. The sintering neck in CPCMs should be just in the early sinter stage and the microstructure is not fully stable. Therefore, in order to obtain

a more rigid CPCM module, a possible approach is to introduce some other elements into the CPCMs, such as nano-scales Al and Cu, to reduce the completely sintering temperature of MgO particles.

(2). To investigate into the anisotropy effect of carbon materials on the thermal properties of CPCMs: The thermal conductivity anisotropy effect of graphite flake is not considered in this thesis. Actually, this is particularly important for the CPCMs materials properties prediction and optimization design of TES component and system and cannot be neglected. Therefore, a systematic study on the anisotropy effect of carbon material is needed and recommended.

(3). To explore the thermal stress within the CPCMs during melting-solidification thermal cycles: The salt motion and particles distribution/redistribution could be leading to a non-uniform thermal stress distribution within the CPCM, which is particularly significant for the CPCM mechanical strength and lifespan predictions and thus is recommended to investigated.

(4). To design and investigate other types of CPCM based TES components and devices: Fabrication CPCMs based components and devices that could be able to deliver the properties at the materials scale should be the ultimate objective for future research on TES component and device fields.

Appendix Publications and Presentations

JOURNAL PAPER:

1) ***Chuan Li***, Sun Ze, Yulong Ding. A numerical investigation into the charge behaviour of a spherical phase change material particle for high temperature thermal energy storage in packed beds. Energy Storage Science and Technology, 2013, 2(5), 480-485.

2) ***Chuan Li***, Zhiwei Ge, Yi Jin, Yongliang Li, Yulong Ding. Heat transfer performance of thermal energy storage component based on composite phase change materials. Energy Storage Science and Technology, 2013, 4(2), 1-8.

3) Bo Zhao, ***Chuan Li*[*]**, Yi Jin, Cenyu Yang, Guanghui Leng, Hui Cao, Yongliang Li, Yulong Ding. Heat transfer performance of thermal energy storage components using composite phase change materials. IET Renewable Power Generation, doi: 10.1049/iet-rpg.2016.0026.

4) ***Chuan Li***, Yongliang Li, Yulong Ding. Composite phase change materials for thermal energy storage: Microstructure development and characteristics. MRS Bulletin, under review.

5) ***Chuan Li***, Yongliang Li, Yulong Ding. Wettability of carbonate salt on magnesium oxide for composite phase change materials fabrication. Applied Energy, under review.

6) ***Chuan Li***, Yongliang Li, Yulong Ding. Effective thermal conductivity of carbonate-salt based composite phase change materials for thermal energy storage. International Journal of Heat and Mass Transfer, under review.

7) ***Chuan Li***, Yongliang Li, Yulong Ding. A review of heat transfer and performance enhancement for PCM-based shell and tube thermal energy storage device. Renewable and sustainable Energy Reviews, under review.

8) ***Chuan Li***, Yongliang Li, Yulong Ding. Carbonate-salt based composite phase change materials for thermal energy storage: Linking composite module performance to device performance. Applied Thermal Engineering, under review.

9) Peilun Wang, Xiang Wang, Yun Huang, ***Chuan Li***, Zhijian Peng, Yulong Ding. Thermal energy charging behavior of a heat exchange device with a zigzag plate configuration containing multi-phase-change-materials (m-PCMs). Applied Energy, 2015(142), 328-336.

10) Zhiwei Ge, Yongliang Li, Dacheng Li, Ze Sun, Yi Jin, Chuanping Liu*, **Chuan Li***, Guanghui Leng, Yulong Ding. Thermal energy storage: challenges and the role of particle technology. Particuology, 2014(15), 2-8.

11) Chuanping Liu, ***Chuan Li***, Yongliang Li, Yulong Ding, Li Wang. Review of heat transfer enhancement in gas-solid flow. Journal of Chemical Industry and Engineering (China), 2014, 7(65), 2485-2494.

PRESENTATIONS:

1) ***Chuan Li***, Yulong Ding. Numerical investigation of the charge behaviour of packed bed storage unit for high temperature energy storage applications. 20th Joint Annual Conference of CSCST-SCI, June 2013, London, UK.

2) ***Chuan Li***, Yulong Ding. Thermal charging behaviour of packed bed storage particle unit and system for high temperature energy storage applications. 4th UK-China Particle Technology Forum, September 2013, Shanghai, China.

3) ***Chuan Li***, Ze Sun, Yulong Ding. A numerical investigation into the charge behaviour of an encapsulated spherical phase change materials (PCM) particle for high temperature thermal energy storage applications. 7th World Congress on Particle Technology (WCPT7), July 2014, Beijing, China.

4) ***Chuan Li***, Yulong Ding. Heat transfer performance of thermal energy storage units based on the composite phase change materials. UK Energy Storage Conference, November 2014, Coventry, UK.

5) ***Chuan Li***, Yulong Ding. Thermal energy storage based on composite phase change materials: linking materials properties to system performance. 12th UK Particle Technology Forum, September 2014, Manchester, UK.

6) ***Chuan Li***, Yulong Ding. Thermal energy storage using composite phase change materials: linking materials properties to device performance. 2nd Training School-Numerical Modelling of Thermal Energy Storage System, June 2015, Lyon, France.

7) ***Chuan Li***, Yulong Ding. Heat transfer performance of thermal energy storage components for low and medium temperature applications. Offshore Energy & Storage Symposium, July 2015, Edinburgh, UK.

8) ***Chuan Li***, Yulong Ding. Heat transfer performance of thermal energy storage components based on the composite phase change materials. 14th UK Heat Transfer Conference, September 2015, Edinburgh, UK.

9) ***Chuan Li***, Yongliang Li, Yulong Ding. Effective thermal conductivity of carbonate salt based composite phase change materials for thermal energy storage. UK Energy Storage Conference, November 2015, Birmingham, UK.

10) ***Chuan Li***, Yongliang Li, Yulong Ding. Composite phase change materials for thermal energy storage: Microstructural characteristics and effective thermal conductivity predication. UK-China Thermal Energy Storage Workshop, December 2015, Beijing, China.

Bibliography

[1] Goran Strbac, Marko Aunedi, Danny Pudjianto, et al. Strategic assessment of the role and value of energy storage systems in the UK low carbon energy future. *Carbon Trust*, June 2012.

[2] UK DECC. Clean Coal: an industrial strategy for the development of catbon capture and storage across the UK. March 2010.

[3] CAS Sustainable Development Strategy Study Group. China sustainable development strategy report 2011. *Science Press*, March 2011.

[4] India energy outlook, World Energy Outlook Special Report, 2015

[5] Renewable Energy Prospects: United States of America, Remap 2030 analysis. January 2015.

[6] Zhiwei Ge, Yongliang Li, Dacheng Li, Ze Sun, Yi Jin, Chuanping Liu, Chuan Li, Guanghui Leng, Yulong Ding. Thermal energy storage: Challenges and the role of particle technology. *Particuology* **15** (2014) 2-8.

[7] Haisheng Chen, Thang Ngoc Cong, Wei Yang, Chunqing Tan, Yongliang Li, Yulong Ding. Progress in electrical energy storage system: A critical review. *Progress in Natural Science* **19** (2009) 291-312.

[8] Yongliang Li, Yi Jin, Yun Huang, Feng Ye, Xiang Wang, Yulong Ding. Principles and new development of thermal storage technology. *Energy Storage Science and Technology* **2** (2013) 69-72. (in chinese)

[9] Zhiwei Ge, Feng Ye, Hui Cao, Guanghui Leng, Yue Qin, Yulong Ding. Carbonate-salt-based composite materials for medium and high temperature thermal energy storage. *Particuology* **15** (2014) 77-81.

[10] Zhiwei Ge, Feng Ye, Yulong Ding. Composite materials for thermal energy storage: Enhancing performance through microstructures. *ChemSusChem* **7** (5) 2014 1318-1325.

[11] Antoni Gil, Marc Medrano, Ingrid Martorell, Ana Lazaro, Pablo Dolado, Belen Zalba, Lusia F. Cabeza. State of the art on high temperature thermal energy storage for power generation. Part 1—Concepts, materials and modellization. *Renewable and Sustainable Energy Reviews* **14** (2010) 31-55.

[12] Marc Medrano, Antoni Gil, Ingrid Martorell, Xavi Potau, Lusia F. Cabeza. State of the art on high-temperature thermal energy storage for power generation. Part 2—Case studies. *Renewable and Sustainable Energy Reviews* **14** (2010) 56-72.

[13] Mohammed M. Farid, Amar M. Khudhair, Siddique Ali K. Razack, Said Al-Hallaj. A review on phase change energy storage: materials and applications. *Energy Conversion and Management* **45** (2004) 1597-1615.

[14] Prashant Verma, Varun, S.K. Singal. Review of mathematical modeling on latent heat thermal energy storage systems using phase-change material. *Renewable and Sustainable Energy Reviews* **12** (2008) 999-1031.

[15] Annette Evans, Vladimir Strezov, Tim J. Evans. Assessment of utility energy storage options for increased renewable energy penetration. *Renewable and Sustainable Energy Reviews* **16** (2012) 4141-4147.

[16] Sarada Kuravi, Jamie Trahan, D. Yogi GOswami, Muhammed M. Rahman, Elia K. Stefanakos. Thermal energy storage technologies and systems for concentrating solar power plants. *Progress in Energy and Combustion Science* **39** (2013) 285-319.

[17] Belen Zalba, Jose M Marin, Luisa F Cabeza, Harald Mehling. Review on thermal energy storage with phase change: materials, heat transfer analysis and applications. *Applied Thermal Engineering* **23** (2003) 251-283.

[18] Atul Sharma, V.V. Tyagi, C.R. Chen, D. Buddhi. Review on thermal energy storage with phase change materials and applications. *Renewable and Sustainable Energy Reviews* **13** (2009) 318-345.

[19] Murat M Kenisarin. High-temperature phase change materials for thermal energy storage. *Renewable and Sustainable Energy Reviews* **14** (2010) 955-970.

[20] Yvan Dutil, Daniel R. Rousse, Nizar Ben Salah, Stephane Lassue, Laurent Zalewski. A review on phase-change materials: Mathematical modeling and simulations. *Renewable and Sustainable Energy Reviews* **15** (2011) 112-130.

[21] A. AFelix Regin, S.C. Solanki, J.S. Saini. Heat transfer characteristics of thermal energy storage system using PCM capsules: A review. *Renewable and Sustainable Energy Reviews* **12** (2008) 2438-2458.

[22] S. SJegadheeswaran, S.D. Pohekar, T. Kousksou. Exergy based performance evaluation of latent heat thermal storage system: A review. *Renewable and Sustainable Energy Reviews* **14** (2010) 2580-2596.

[23] R.J. Goldstein, W.E. Ibele, S.V. Patankar, T.W. Simon, T.H. Kuehn, P.J. Strykowski, K.K. Tamma, J.V.R. Heberlein, J.H. Davidson, J. Bischof, F.A. Kulacki, U. Kortshagen, S. Garrick, V. Srinivasan, K. Ghosh, R. Mittal. Heat transfer—A review of 2004 literature. *International Journal of Heat and Mass Transfer* **53** (2010) 4343-4396.

[24] D.Fernandes, F. Pitie, G. Caceres, J. Baeyens. Thermal energy storage: "How previous findings determine current research priorities". *Energy* **39** (2012) 246-257.

[25] Dan Nchelatebe Nkwetta, Fariborz Hagighat. Thermal energy storage with phase change material—A state-of-the art review. *Sustainable Cities and Society* **10** (2014) 87-100.

[26] Harmeet Singh, R.P. Saini, J.S. Saini. A review on packed bed solar energy storage systems. *Renewable and Sustainable Energy Reviews* **14** (2010) 1059-1069.

[27] Bruno Cardenas, Noel Leon. High temperature latent heat thermal energy storage: Phase change materials, design considerations and performance enhancement techniques. *Renewable and Sustainable Energy Reviews* **27** (2013) 724-737.

[28] J M Khodadadi, Liwu Fan, Hasan Babaei. Thermal conductivity enhancement of nanostructure-based colloidal suspensions utilized as phase change materials for thermal energy storage: A review. *Renewable and Sustainable Energy Reviews* **24** (2013) 418-444.

[29] Abduljalil A Al-abidi, Sohif Bin Mat, K Sopian, M Y Sulaiman, Abdulrahman Th Mohammed. CFD applications for latent heat thermal energy storage: a review. *Renewable and Sustainable Energy Reviews* **20** (2013) 353-363.

[30] Ye Hong, Ge Xin-Shi. Preparation of polyethylene-paraffin compound as a form-stable solid–liquid phase change material. *Solar Energy Materials and Solar Cells* **64** (2000) 37–44.

[31] Weilong Wang, Xiaoxi Yang, Yutang Fang, Jing Ding. Preparation and performance of form-stable polyethylene glycol/silicon dioxide composites as solid–liquid phase change materials. *Applied Energy* **86** (2009) 170-174.

[32] Bingtao Tang, Meige Qiu, Shufen Zhang. Thermal conductivity enhancement of PEG/SiO2 composite PCM by in situ Cu doping. *Solar Energy Materials & Solar Cells* **105** (2012) 242-248.

[33]Jingruo Li, Lihong He, Tangzhi Liu, Xuejuan Cao, Hongzhou Zhu. Preparation and characterization of PEG/SiO2 composites as shape-stabilized phase change materials for thermal energy storage. *Solar Energy Materials & Solar Cells* **118** (2013) 48-53.

[34]Weilong. Wang, X.iaoxi Yang, Yutang Fang, Jing Ding, Jinyue Yan. Enhanced thermal conductivity and thermal performance of form-stable composite phase change materials by using b-Aluminum nitride. *Applied Energy* **86** (7-8) (2009) 1196-1200.

[35] N Gokon, D Nakano, S Inuta, T Kadama. High temperature carbonate/MgO composite materials as thermal storage media for double-walled solar reformer tubes. *Solar Energy* **82** (2008) 1145-1153.

[36] Su Xu, Liming Zou, Xinlong Ling, Yizhe Wei, Shengkai Zhang. Preparation and thermal reliability of methyl palmitate/methylstearate mixture as a novel composite phase change material. *Energy and Buildings* **68** (2014) 372-375.

[37] W Notter, Th Lechner, U GroB and E Hahne. Thermophysical properties of the composite ceramic-salt system (SiO2 /Na$_2$SO$_4$). *Thermochimica Acta* **218** (1993) 455-463.

[38] Ahmet Sari, Ali Karaipekli. Thermal conductivity and latent heat thermal energy storage characteristics of paraffin/expanded graphite composite as phase change material. *Applied Thermal Engineer* **27** (2007) 1271–1277.

[39] Ali Karaipekil, Ahmet Sari, Capric-myristic acid/expanded perlite composite as form-stable phase change material for latent heat thermal energy storage. *Renewable Energy* **33** (2008) 2599-2605.

[40] Ali Karaipekil, Ahmet Sari, Capric–myristic acid/vermiculite composite as form-stable phase change material for thermal energy storage. *Solar Energy* **83** (2009) 323-332.

[41] Huazhe Yang, Lili Feng, Chongyun Wang, Wei Zhao, Xingguo Li. Confinement effect of SiO2 framework on phase change of PEG in shape-stabilized PEG/SiO2 composites. *European Polymer Journal* **48** (2012) 803–810.

[42] Qinglong Zhang, Jiachun Feng. Di. Functional olefin block copolymer/paraffin form-stable phase change materials with simultaneous shape memory property. *Solar Energy Materials & Solar Cells* **117** (2013) 259-266.

[43] Sedat Karaman, Ali Karaipekli, Ahmet Sari, Alper Bicer. Polyethylene glycol (PEG)/diatomite composite as a novel form-stable phase change material for thermal energy storage. *Solar Energy Materials & Solar Cells* **95** (7) (2011) 1647-1653.

[44] Feng Ye, Zhiwei Ge, Yulong Ding, Jun Yang. Multi-walled carbon nanotubes added to Na$_2$CO$_3$/MgO composites forthermal energy storage. *Particuology* **15** (2013) 56-60.

[45] Keping Chen, Xuejiang Yu, Chunrong Tian, Jianhua Wang. Preparation and characterization of form-stable paraffin/polyurethane composites as phase change materials for thermal energy storage. *Energy Conversion and Management* **77** (2014) 13-21.

[46] Mohammad Mehrali, Sara Tahan Latibari, Mehdi Mehrali, Teuku Meurah Indra Mahlia, Hendrik Simon Cornrils Metselaar. Preparation and characterization of palmitic acid/grapheme nanoplatelets composite with remarkable thermal conductivity as a novel shape-stabilized phase change material. *Applied Thermal Engineering* **61** (2013) 633-640.

[47] Lili Feng, Jie Zheng, Huazhe Yang, Yanli Guo, Wei Li, Xingguo Li. Preparation and characterization of polyethylene glycol/active carbon composites as shape-stabilized phase change materials. *Solar Energy Materials & Solar Cells* **95** (2011) 644-650.

[48] T Kodama, Y Isobe, Y Kondoh, S Yamaguchi, K I Shimizu. Ni/ceramic/molten-salt composite catalyst with high temperature thermal storage for use in solar reforming processes. *Energy* **29** (2004) 895-903.

[49]Yutang Fang, Huimin Yu, Weijun Wan, Xuenong Gao, Zhengguo Zhang. Preparation and thermal performance of polystyrene/n-tetradecane composite nanoencapsulated cold energy storage phase change materials. *Energy Conversion and Management* **76** (2013) 430-436.

[50] Fang Chen, Michael P Wolcott. Miscibility studies of paraffin/polyethylene blends as form-stable phase change materials. *European Polymer Journal* **52** (2014) 44-52.

[51] Shazim Ali Memon, Tommy Yiu Lo, Hongzhi Cui, Salim Barbhuiya. Preparation, characterization and thermal properties ofdodecanol/cement as novel form-stable composite phasechange material. *Energy and Buildings* **66** (2013) 697-705.

[52] Chongyun Wang, Lili Feng, Wei Li, Jie Zheng, Wenhuai, Tian, Xingguo Li. Shape-stabilized phase change materials based on polyethylene glycol/porous carbon composite: The influence of the pore structure of the carbon materials. *Solar Energy Materials & Solar Cells* **105** (2012) 21-26.

[53] Lingjian Zhang, Haifeng Shi, Weiwei Li, Xu Han, Xingxiang Zhang. Structure and thermal performance of poly(ethylene glycol) alkyl ether (Brij)/porous silica (MCM-41composites as shape-stabilized phase change materials. *Thermochimica Acta* **570** (2013) 1-7.

[54] Qinglong Zhang, Yiqing Zhao, Jiachun Feng. Systematic investigation on shape stability of high-efficiency SEBS/paraffin form-stable phase change materials. *Solar Energy Materials & Solar Cells* **118** (2013) 54-60.

[55] Dong Zhang, Jianming Zhou, Keru Wu, Zongjin Li. Granular phase changing composites for thermal energy storage. *Solar Energy* **78** (2005) 471-480.

[56] X Xiao, P Zhang. Morphologies and thermal characterization of paraffin/carbon foam composite phase change material. *Solar Energy Materials & Solar Cells* **117** (2013) 451-461.

[57] Guobing Zhou, Yongping Yang, Xin Wang, Shaoxiang Zhou. Numerical analysis of effect of shape-stabilized phase change material plates in a building combined with night ventilation. *Applied Energy* **86** (2009) 52-59.

[58] A.H Ahmadi Motlagh, S H Hashemabadi. 3D CFD simulation and experimental validation of particle-to-fluid heat transfer in a randomly packed bed of cylindrical particles. *International Communications in Heat and Mass Transfer* **25** (2008) 1183-1189.

[59] Harmeet Singh, R P Saini, J S Saini. Performance of a packed bed solar energy storage system having large sized elements with low void fraction. *Solar Energy* **87** (2013) 22-34.

[60] S. SKarthikeyan, R. Velraj, Numerical investigation of packed bed storage unit filled with PCM encapsulated spherical containers-A comparison between various mathematical models. *International Journal of Thermal Sciences* **60** (2012) 153-160.

[61] Eduard Oro, Justin Chiu, Viktoria Martin, Luisa F. Cabeza, Comparative study of different numerical models of packed bed thermal energy storage systems. *Applied Thermal Engineering* **50** (2013) 384-392.

[62] Mohamed Rady. Thermal performance of packed bed thermal energy storage units using multiple granular phase change composites. *Applied Energy* **86** (2009) 2704-2720.

[63]L. Xia, P. Zhang, R.Z. Wang, Numerical heat transfer analysis of the packed bed latent heat storage system based on an effective packed bed model. *Energy* **35** (2010) 2022-2032.

[64] Aytunc Erek, Ibrahim Dincer. Numerical heat transfer analysis of encapsulated ice thermal energy storage system with variable heat transfer coefficient in downstream. *International Journal of Heat and Mass Transfer* **52** (2009) 851-859.

[65] C Arkar, S Medved. Influence of accuracy of thermal property data of a phase change material on the result of a numerical model o f a packed bed latent heat storage with spheres. *Thermochimica Acta* **438** (2005) 192-201.

[66] A Benmansour, MA Hamdan, A Bengeuddach. Experimental and numerical investigation of solid particles thermal energy storage unit. *Applied Thermal Engineering* **26** (2006) 513-518.

[67] Tao Hu, Abdel Hakim Hassabou, Markus Spinnler, Wolfgang Polifke, Performance analysis and optimization of direct contact condensation in a PCM fixed bed regenerator. *Desalination* **280** (2011) 232-243.

[68] K.A.R. Ismail, J.R. Henríquez, Numerical and experimental study of spherical capsules packed bed latent heat storage system. *Applied Thermal Engineering* **22** (2002) 1705-1716.

[69] A.F. Regin, S.C. Solanki, J.S. Saini, An analysis of a packed bed latent heat thermal energy storage system using PCM capsules: numerical investigation. *Renewable Energy* **34** (2009) 1765-1773.

[70] M. Rady, Granular phase change materials for thermal energy storage: experiments and numerical simulations. *Applied Thermal Engineering* **29** (2009) 3149-3159.

[71] D. MacPhee, I. Dincer, Thermal modeling of a packed bed thermal energy storage system during charging. *Applied Thermal Engineering* **29** (2009) 695-705.

[72] Shuangmao Wu, Guiyin Fang, Xu Liu, Thermal performance simulations of a packed bed cool thermal energy storage system using n-tetradecane as phase change material. *International Journal of Thermal Sciences* **49** (2010) 1752-1762.

[73] Hitesh Bindra, Pablo Bueno, Jeffrey F. Morris, Reuel Shinnar, Thermal analysis and exergy evaluation of packed bed thermal storage systems. *Applied Thermal Engineering* **52** (2013) 255-263.

[74] X. Xiao, P. Zhang. Numerical and experimental study of heat transfer characteristics of a shell-tube latent heat storage system: Part I-Charging process. *Energy* **79** (2015) 337-350.

[75] X. Xiao, P. Zhang. Numerical and experimental study of heat transfer characteristics of a shell-tube latent heat storage system: Part II-Discharging process. *Energy* **80** (2015) 177-189.

[76] Anica Trp. An experimental and numerical investigation of heat transfer during technical grade paraffin melting and solidification in a shell-and-tube latent thermal energy storage unit. *Solar Energy* **79** (2005) 648-660.

[77] Xu Liu, Guiyin Fang, Zhi Chen. Dynamic charging characteristics modeling of heat storage device with heat pipe. *Applied Thermal Engineering* **31** (2011) 2902-2908.

[78] V. Pandiyarajan, M. Chinna Pandian, E. Malan, R. Velraj, R.V. Seeniraj. Experiemntal investigation on heat recovery from diesel engine exhaust using finned shell and tube heat exchanger and thermal storage system. *Applied Energy* **88** (2011) 77-87.

[79] Mete Avci, M. Yusuf Yazici. Experimental study of thermal energy storage characteristics of a paraffin in a horizontal tube-in-shell storage unit. *Energy Conversion and Management* **73** (2013) 271-277.

[80] Mithat Akgun, Orhan Aydin, Kamil Kaygusuz. Experimental study on melting/solidification characteristics of a paraffin as PCM. *Energy Conversion and Management* **48** (2007) 669-678.

[81] Francis Agyenim, Philip Eames, Mervyn Smyth. Heat transfer enhancement in medium temperature thermal energy storage system using a multitube heat transfer array. *Renewable Energy* **35** (2010) 198-207.

[82] Wei-Wei Wang, Kun Zhang, Liang-Bi Wang, Ya-Ling He. Numerical study of the heat charging and discharging characteristics of a shell-and-tube phase change heat storage unit. *Applied Thermal Engineering* **58** (2013) 542-553.

[83] Y.B. Tao, Y.L. He, F.Q. Cui, C.H. Lin. Numerical study on coupling phase change heat transfer performance of solar dish collector. *Solar Energy* **90** (2013) 84-93.

[84] Kamal A.R. Ismail, Mabruk M. Abugderah. Performance of a thermal storage system of the vertical tube type. *Energy Conversion and Management* **41** (2000) 1165-1190.

[85] Yu Wang, Ya-Ling He, Yong-Gang Lei, Jie Zhang. Heat transfer and hydrodynamics analysis of a novel dimpled tube. *Experimental Thermal and Fluid Science* **34** (2010) 1273-1281.

[86] Francis Agyenim, Philip Eames, Mervyn Smyth. A comparison of heat transfer enhancement in a medium temperature thermal energy storage heat exchanger using fins. *Solar Energy* **83** (2009) 1509-1520.

[87] A.H. Mosaffa, F. Talati, H. Basirat Tabrizi, M.A. Rosen. Analytical modeling of PCM solidification in a shell and tube finned thermal storage for air conditioning systems. *Energy and Buildings* **49** (2012) 356-361.

[88] Evan Fleming, Shaoyi Wen, Li Shi, Alexandre K. da Silva. Experimental and theoretical analysis of an aluminum foam enhanced phase change thermal storage unit. *International Journal of Heat and Mass Transfer* **82** (2015) 273-281.

[89] Kemal Ermis, Aytunc Erek, Ibrahim Dincer. Heat transfer analysis of phase change process in a finned-tube thermal energy storage system using artificial neural network. *International Journal of Heat and Mass Transfer* **50** (2007) 3163-3175.

[90] Hamid Ait Adine, Hamid EI Qarnia. Numerical analysis of the thermal behaviour of a shell-and-tube heat storage unit using phase change materials. *Applied Mathematical Modelling* **33** (2009) 2132-2144.

[91] K.A.R.Ismail, C.L.F. Alves, M.S.Modesto. Numerical and experimental study on the solidification of PCM around a vertical axially finned isothermal cylinder. *Appied Thermal Engineering* **21** (2001) 53-77.

[92] Zhenyu Liu, Yuanpeng Yao, Huiying Wu. Numerical modeling for solid–liquid phase change phenomena in porous media: Shell-and-tube type latent heat thermal energy storage. *Applied Energy* **112** (2013) 1222-1232.

[93] Manish K. Rathod, Jyotirmay Banerjee. Thermal performance enhancement of shell and tube Latent Heat Storage Unit using longitudinal fins. *Applied Thermal Engineering* **75** (2015) 1084-1092.

[94] A.H. Mosaffa, L. Garousi Farshi, C.A. Infante Ferreira, M.A. Rosen. Energy and exergy evaluation of a multiple-PCM thermal storage unit for free cooling applications. *Renewable Energy* **68** (2014) 452-458.

[95] Osama Mesalhy, Khalid Lafdi, Ahmed EIgafy, Keith Bowman. Numerical study for enhancing the thermal conductivity of phase change material (PCM) storage using high thermal conductivity porous matrix. *Energy Conversion and Management* **46** (2005) 847-867.

[96] Chaxiu Guo, Wujun Zhang. Numerical simulation and parametric study on new type of high temperature latent heat thermal energy storage system. *Energy Conversion and Management* **49** (2008) 919-927.

[97] Y.Q. Li, Y.L. He, H.J. Song, C.Xu, W.W. Wang. Numerical analysis and parameters optimization of shell-and-tube heat storage unit using three phase change materials. *Renewable Energy* **59** (2013) 92-99.

[98] Ehsan Mohseni Languri, Clifford O.Aigbotsua, Jorge L.Alvarado. Latent thermal energy storage system using phase change material in corrugated enclosures. *Applied Thermal Engineering* **50** (2013) 1008-1014.

[99] Yuwen Zhang, A. Faghri. Heat transfer enhancement in latent heat thermal energy storage system by using the internally finned tube. *International Journal of Heat and Mass Transfer* **39** (1995) 3165-3173.

[100] Ming Liu, Martin Belusko, N.H. Steven Tay, Frank Bruno. Impact of the heat transfer fluid in a flat plate phase change thermal storage unit for concentrated solar tower plants. *Solar Energy* **101** (2014) 220-231.

[101] Alvaro Campos-Celador, Gonzalo Diarce, Jon TeresZubiaga, Tatyana V. Bandos, Ane M. Garcia-Romero, L.M. Lopez, Jose M. Sala. Design of a finned plate latent heat thermal energy storage systemfor domestic applications. *Energy Procedia* **48** (2014) 300-308.

[102] A. Campos-Celador, G. Diarce, I. Gonzalez-Pino, J.M. Sala. Development and comparative analysis of the modeling of an innovative finned-plate latent heat thermal energy storage system. *Energy* **58** (2013) 438-447.

[103] M. Johnson, M. Fiss, T. Klemm, M. Eck. Test and analysis of a flat plate latent heat storage design. *Energy Procedia* **57** (2014) 662-671.

[104] Mohammed Bechiri, Kacem Mansouri. Exact solution of thermal energy storage system using PCM flat slabs configuration. *Energy Conversion and Management* **76** (2013) 588-598.

[105] Y. Tian, C.Y. Zhao. A numerical investigation of heat transfer in phase change materials (PCMs) embedded in porous metals. *Energy* **36** (2011) 5539-5546.

[106] Pavel Charvat, LubomirKlimes, Milan Ostry. Numerical and experimental investigation of a PCM-based thermalstorage unit for solar air systems. *Energy and Buildings* **68** (2014) 488-497.

[107] E. Halawa, W. Saman. Thermal performance analysis of a phase change thermal storage unit for space heating. *Renewable Energy* **36** (2011) 259-264.

[108] Wei-Biao Ye, Dong- Sheng Zhu, Nan Wang. Numeical simulation on phase-change thermal storage/release in a plate-fin unit. *Applied Thermal Engineering* **31** (2011) 3871-3884.

[109] A.A. Rabienataj Darzi, S.M. Moosania, F.L. Tan, M. Farhadi. Numerical investigation of free-cooling system using plate type PCM storage. *International Communications in Heat and Mass Transfer* **48** (2013) 155-163.

[110] Olga P. Arsenyeva, Barry Crittenden, Mangyan Yang, Petro O. Kapustenko. Accounting for the thermal resistance of cooling water fouling in plate heat exchangers. *Applied Thermal Engineering* **61** (2013) 53-59.

[111] Pourya Forooghi, Kamel Hooman. Experimental analysis of heat transfer of supercritical fluids in plate heat exchangers. *International Journal of Heat and Mass Transfer* **74** (2014) 448-459.

[112] Cagin Gulenoglu, Fatih Akturk, Selin Aradag, Nilay Sezer Uzol, Sadik Kakac. Experimental comparison of performances of three different plates for gasketed plate heat exchangers. *International Journal of Thermal Science* **75** (2014) 249-256.

[113] Zhe Wang, Yanzhong Li, Min Zhao. Experimental investigation on the thermal performance of multi-stream plate-fin heat exchanger based on genetic algorithm layer pattern design. *International Journal of Heat and Mass Transfer* **82** (2015) 510-520.

[114] Hoseong Lee, Song Li, Yunho Hwang, Reinhard Radermacher, Ho-Hwan Chun. Experimental investigations on flow boiling heat transfer in plate heat exchanger at low mass flux condition. *Applied Thermal Engineering* **61** (2013) 408-415.

[115] Artur J. Jaworski, Antonio Piccolo. Heat transfer processes in parallel-plate heat exchangers of thermoacousticdevices -numerical and experimentalapproaches. *Applied Thermal Engineering* **42** (2012) 145-153.

[116] M.A. Arie, A.H. Shooshtari, S.V. Dessiatoun, E. Al-Hajri, M.M. Ohadi. Numerical modeling and thermal optimization of a single-phase flowmanifold-microchannel plate heat exchanger. *International Journal of Heat and Mass Transfer* **81** (2015) 478-489.

[117] Fabio A.S. Mota, Mauro A.S.S. Ravagnani, E.P.Carvalho. Optimal design of plate heat exchangers. *Applied Thermal Engineering* **63** (2014) 33-39.

[118] S. Ghosh, I. Ghosh, D.K. Pratihar, B. Maiti, P.K. Das. Optimum stacking pattern for multi-stream plate-fin heat exchanger through a genetic algorithm. *International Journal of Thermal Sciences* **50** (2011) 214-224.

[119] N.H.S. Tay, F. Bruno, M. Belusko. Comparison of pinned and finned tubes in a phase change thermal energy storage system using CFD. *Applied Energy* **104** (2013) 79-86.

[120] N.H.S. Tay, M. Belusko, F. Bruno. Experimental investigation of tubes in a phase change thermal energy storage system. *Applied Energy* **90** (2012) 288-297.

[121] N.H.S. Tay, F. Bruno, M. Belusko. Experimental validation of a CFD and an e-NTU model for a large tube-in-tank PCM system. *International Journal of Heat and Mass Transfer* **55** (2012) 5931-5940.

[122] N.H.S. Tay, F. Bruno, M. Belusko. Experimental validation of a CFD model for tubes in a phase change thermal energy storage system. *International Journal of Heat and Mass Transfer* **55** (2012) 574-585.

[123] Gulsah Cakmak. Experimental investigation of thermal storage in U-tube heat exchanger. *International Communications in Heat and Mass Transfer* **44** (2013) 83-86.

[124] Jundika C. Kurnia, Agus P. Sasmito, Sachin V. Jangam, Arun S. Mujumdar. Improved design for heat transfer performance of a novel phase change material (PCM) thermal energy storage (TES). *Applied Thermal Engineering* **50** (2013) 896-907.

[125] Marwaan AL-Khaffajy, Ruth Mossad. Optimization of the heat exchanger in a flat plate indirect heating integrated collector storage solar water heating system. *Renewable Energy* **57** (2013) 413-421.

[126] Miroslaw Zukowski. Experimental study of short term thermal energy storage unit based on enclosed phase change material in polyethylene film bag. *Energy Conversion and Management* **48** (2007) 166-173.

[127] Jungwook Shon, Hyungik Kim, Kihyung Lee. Improved heat storage rate for an automobile coolant waste heat recovery system using phase-change material in fin-tube heat exchanger. *Applied Energy* **113** (2104) 680-689.

[128] Antoni Gil, Eduard Oro, Albert Castell, Luisa F. Cabeza. Experimental analysis of the effectiveness of a high temperature thermal storage tank for solar cooling applications. *Applied Thermal Engineering* **54** (2013) 521-527.

[129] Fabien Rouault, Denis Bruneau, Patrick Sebastian, Jerome Lopez. Experimental investigation and modelling of a low temperature PCM thermal energy exchange and storage system. *Energy and Buildings* **83** (2014) 96-107.

[130] Moran Wang, Ning Pan. Predictions of effective physical properties of complex multiphase materials. *Materials Science and Engineering R* **63** (2008) 1-30.

[131] Longlong Yang, Ping Shen, Qiaoli Lin, Feng Qiu, Qichuan Jiang. Wetting of porous graphite by Cu-Ti alloys at 1373 K. *Materials Chemistry and Physics* **124** (2010) 499-503.

[132] F.B. Swinkel, M.F. Ashby. A second report on sintering diagrams. *Acta Metallurgica* **29** (1981) 259-281.

[133] M.F. Ashby, A first report on sintering diagrams. *Acta Metallurgica* **22** (1974) 275-289.

[134] Katsuyoshi Kondoh, Masashi Kawakami, Hisashi Imai, Junko Umeda, Hidetoshi Fujii. Wettability of pure Ti by molten pure Mg droplets. *Acta Materialia* **58** (2010) 606-614.

[135] Likun Zang, Zhangfu Yuan, Hongxin Zhao, Xiaorui Zhang.Wettability of molten Sn-Bi-Cu solder on Cu substrate. *Materials Letters* **63** (2009) 2067-2069.

[136] Carmen Chiappori, Saverio Russo, Antonio Turturro. Wettability of glass substrates by molten nylon-6. *Polymer* **22** (1981) 534-538.

[137] B.S Tanem, O. Lunder, A. Borg, J. Mardalen. AFM adhesion force measurements on conversion-coated EN AW-6082-T6 aluminium. *International Journal of Adhesion & Adhesives* **29** (2009) 471-477.

[138] Stephan Frybort, Michael Obersriebnig, Ulrich Muller, Wolfgang Gindl-Altmutter, Johannes Konnerth. Variability in surface polarity of wood by means of AFM adhesionforce mapping, Colloids and Surfaces A: *Physicochemical and Engineering Aspects* **457** (2014) 82-87.

[139] M Meincken, T.A Berhane, P.E Mallon. Tracking the hydrophobicity recovery of PDMS compounds using the adhesive force determined by AFM force distance measurements. *Polymer* **46** (2005) 203-208.

[140] Pelin. I.M, Piednoir. A, Machon. D, Farge. P, Pirat. C, Ramos. S.M.M, Adhesion forces between AFM tips and superficial dentin surfaces. *Journal of Colloid and Interface Science* **376** (2012) 262-268.

[141] Jianfeng Wang, James K. Carson, Mike F. North, Donald J. Cleland. A new approach to modelling the effective thermal conductivity of heterogeneous materials. *International Journal of Heat and Mass Transfer* **49** (2006) 3075-3083.

[142] R.C.Progelhof, J.L.Throne, R.R.Ruetsch. Methods for predicting the thermal conductivity of composite systems: *A review. Polymer Engineering and Science* **16** (1976) 615-625.

[143] Ramvir Singh, H.S. Kasana. Computational aspects of effective thermal conductivity of highly porous metal foams. *Applied Thermal Engineering* **24** (2004) 1841-1849.

[144] Juan Shi, Zhenqian Chen, Shuai Shao, Jiayi Zheng. Experimental and Numerical study on effective thermal conductivity of novel form-stable basalt fiber composite concrete with PCMs for thermal storage. *Applied Thermal Engineering* **66** (2014) 156-161.

[145] W. van Antwerpen, C.G du Toit, P.G. Rousseau. A review of correlations to model the packing structure and effective thermal conductivity in packed beds of mono-sized spherical particles. *Nuclear Engineering and Design* **240** (2010) 1803-1818.

[146] E. Tsotsas, H. Martin. Thermal conductivity of packed beds: A review. *Chemical Engineering and Processing* **22** (1987) 19-37.

[147] Jame K. Carson, Simon J. Lovatt, David J. Tanner, Andrew C. Cleland. Thermal conductivity bounds for isotropic, porous materials. *International Journal of Heat and Mass Transfer* **48** (2005) 2150-2158.

[148] K.C. Leong, H.Y. Li. Theoretical study of the effective thermal conductivity of graphite foam based on a unit cell model. *International Journal of Heat and Mass Transfer* **54** (2011) 5491-5496.

[149] T.H. Bauer. A general analytical approach toward the thermal conductivity of porous media. *International Journal of Heat and Mass Transfer* **36** (17) (1993) 4181-4191.

[150] F. Gori, S. Corasaniti. Effective thermal conductivity of composites. *International Journal of Heat and Mass Transfer* **77** (2014) 653-661.

[151] Amir Akbari, Mohsen, Reghan J. Hill. Effective thermal conductivity of two-dimensional anisotropic two-phase media. *International Journal of Heat and Mass Transfer* **63** (2013) 41-50.

[152] Daizo Kunii and J.M. Smith. Heat transfer characteristics of porous rocks. *A.I.Ch.E. Journal* **6** (1) (1960) 71-78.

[153] C.T. Hsu, P.Cheng, K.W. Wong. Modified Zehner-Schlunder models for stagnant thermal conductivity of porous media. *International Journal of Heat and Mass Transfer* **37** (1994) 2751-2759.

[154] K.C. Chan, Christopher Y.H. Chao. A theoretical model on the effective stagnant thermal conductivity of an adsorbent embedded with a highly thermal conductive material. *International Journal of Heat and Mass Transfer* **65** (2013) 863-872.

[155] J. Bourret, N. Tessier-Doyen, B. Nait-Ali, F. Pennec, A. Alzina, C.S. Peyratout, D.S.Simth. Effect of the pore volume fraction on the thermal conductivity and mechanical properties of kaolin-based foam. *Journal of the European Ceramic Society* **33** (2013) 1487-1495.

[156] Juan Pablo M. Florez, Marcia B.H. Manteli, Gustavo G.V. Nuernberg. Effective thermal conductivity of sintered porous media: Model and experimental validation. *International Journal of Heat and Mass Transfer* **66** (2013) 868-878.

[157] N. Atabaki, B.R. Baliga. Effective thermal conductivity of water-saturated sintered powder-metal plates. *Heat Mass Transfer* **44** (2007) 85-99.

[158] Alexander EJ Jr. Structure–property relationships in heat pipe wicking materials. Ph.D. Thesis, North Carolina State University, Dept. of Chemical Engineering, North Carolina, (1972).

[159] Min Sheng, Donald. R. Cahela, Hongyun Yang, Carols F. Gonzalez, William R. Yantz Jr., Daniel K. Harris, Bruce J.Tatarchuk. Effective thermal conductivity and junction factor for sintered microfibrous materials. *International Journal of Heat and Mass Transfer* **56** (2013) 10-19.

[160] G.R. Handley, Thermal conductivity of packed metal powders. *International Journal of Heat and Mass Transfer* **29** (1986) 909–920.

[161] Amikam Birnboim, Tayo Olorunyolemi, Yuval Carmel. Calculation the thermal conductivity of heated powder compacts. *Journal of American Ceramic Society* **84** (6) (2001) 1315-1320.

[162] X. Xiao, P. Zhang, M. Li. Effective thermal conductivity of open-cell metal foams impregnated with pure paraffin for latent heat storage. *International Journal of Thermal Sciences* **81** (2014) 94-105.

[163] R.L. Coble, Sintering crystalline solid I. Intermediate and final state diffusion models. *Journal of Applied Physical* **32** (1961) 787-793.

[164] F. Thummler, R. Oberacker. An Introduction to powder Metallurgy, The institut of Materials, London, Unite Kingdom, 1993.

[165] R. Chaim, M. Margulis. Densification maps for spark plasma sintering of nanocrystalline MgO ceramics. *Materials Science and Engineering A* **407** (2005) 180-187.

[166] J. Reis, R. Chaim. Densification maps for spark plasma sintering of nanocrystalline MgO ceramics: Particle coarsening and grain growth effects. *Materials Science and Engineering A* **491** (2008) 356-363.

[167] Yongfen Zhang, Aijun Song, Deqiang Ma, Xinyu Zhang, Mingzhen Ma, Riping Liu. Sintering characteristics and grain growth behaviour of MgO nanopowders by spark plasma sintering. *Journal of Allys and Compounds* **608** (2014) 304-310.

[168] Sagiv Kleiman, Rachman Chaim. Thermal stability of MgO nanoparticles. *Materials Letters* **61** (2007) 4489-4491.

[169] Antonio Ramos Archibold, Muhammad M. Rahman, D. Yogi Goswami, Elias K. Stefanakos. Analysis of heat transfer and fluid flow during melting inside a spherical container for thermal energy storage. *Applied Thermal Engineering* **64** (2014) 396-407.

[170] K. Nithyanandam, R. Pitchumani. Design of a latent thermal energy storage system with embedded heat pipes. *Applied Energy* **126** (2014) 266-280.

[171] Y. B. Tao, M.J. Li, Y.L. He, W.Q. Tao. Effects of parameters on performance of high temperature molten salt latent heat storage unit. *Applied Thermal Engineering* **72** (1)2014 48-55.

[172] Peilun Wang, Hua Yao, Zhipeng Lan, Zhijian Peng, Yun Huang, Yulong Ding. Numerical investigation of PCM melting process in sleeve tube with internal fins. *Energy Conversion and Management* **110** (2016) 428-435.

[173] Abduljalil A. Al-Abidi, Sohif Mat, K. Sopian, M.Y. Sulaiman, Abdulrahman Th. Mohammad. Internal and external fin heat transfer enhancement technique for latent heat thermal energy storage in triplex tube heat exchangers. *Applied Thermal Engineering* **53** (2013) 147-156.

[174] Jialin Yang, Xiaoze Du, Lijun Yang, Yongping Yang. Numerical analysis on the thermal behaviour of high temperature latent heat thermal energy storage system. *Solar Energy* **98** (2013) 543-552.

[175] S. Lorente, A. Bejan, J.L. Niu. Phase change heat storage in an enclosure with vertical pipe in the centre. *International Journal of Heat and Mass Transfer* **72** (2014) 329-335.

[176] Weihuan Zhao, David M. France, Wenhua Yu, Taeil Kim, Dileep Singh. Phase change material with graphite foam for applications in high-temperature latent heat storage systems of concentrated solar power plants. *Renewable Energy* **69** (2014) 134-146.

[177] Zhongyang Luo, Cheng Wang, Gang Xiao, Mingjiang Ni, Kefa Cen. Simulation and experimental study on honeycomb-ceramic thermal energy storage for solar thermal systems. *Applied Thermal Engineering* **73** (2014) 622-628.

[178] C.J Ho, Chun-Ruei Siao, Wei-Mon Yan. Thermal energy storage characteristics in an enclosure packed with MEPCM particles: An experimental and numerical study. *International Journal of Heat and Mass Transfer* **73** (2014) 88-96.

[179] Sarada Kuravi, Jamie Tranhan, D. Yogi Goswami, Muhammad M. Rahman, Elias K. Stefanakos. Thermal energy storage technologies and systems for concentrating solar power plants. *Progress in Energy and Combustion Science* **39** (2013) 285-319.

[180] Nabeel S Dhaidan, J.M Khodadadi, Tahseen A Al-Hattab, Saad M Al-Mashat. Experimental and numerical investigation of melting of phase change material/nanoparticle suspensions in a square container subjected to a constant heat flux. *International Journal of Heat and Mass Transfer* **66** (2013) 672-683.

[181] Andrey M Abyzov, Andrey V Goryunov, Fedor M Shakhov. Effective thermal conductivity of disperse materials. I. Compliance of common models with experimental data. *International Journal of Heat and Mass Transfer* **67** (2013) 752-767.

[182] Majid Bahrami, M Michael Yovanovich, J Richard Culham. Effective thermal conductivity of rough spherical packed beds. *International Journal of Heat and Mass Transfer* **49** (2006) 3691-3701.

[183] Majid Bahrami, M Michael Yovanovich, J Richard Culham. Thermal joint resistances of nonconforming rough surfaces with gas-filled gaps. *Journal of Thermophysics and Heat Transfer* **18** (2004) 326-332.

[184] Majid Bahrami, M Michael Yovanovich, J Richard Culham. Thermal joint resistances of conforming rough surfaces with gas-filled gaps. *Journal of Thermophysics and Heat Transfer* **18** (2004) 318-325.